# Rift and salt-related multi-phase dolomitization: example from the northwestern Pyrenees

Geoffrey Motte, Guilhem Hoareau, Jean-Paul Callot, Sidonie Révillon, Francesca Piccoli, Sylvain Calassou, Eric C Gaucher

Marine and Petroleum Geology 126 (2021) 104932

Contents lists available at ScienceDirect

Marine and Petroleum Geology

journal homepage: www.elsevier.com/locate/marpetgeo

# Rift and salt-related multi-phase dolomitization: example from the northwestern Pyrenees

Geoffrey Motte [a,b,*], Guilhem Hoareau [a], Jean-Paul Callot [a], Sidonie Révillon [c], Francesca Piccoli [d], Sylvain Calassou [b], Eric C. Gaucher [b]

[a] Université de Pau et des Pays de l'Adour, E2S UPPA, CNRS, TOTAL, LFCR, UMR5150, 64000, Pau, France
[b] TOTAL, CSTJF, 64018, Pau Cedex, France
[c] SEDISOR, Institut Universitaire Européen de la Mer, 29280, Plouzane, France
[d] Institute of Geological Sciences, University of Bern, 3012, Bern, Switzerland

ARTICLE INFO

*Keywords:*
Carbonate diagenesis
Dolomite
Breccias
Hydrothermalism
U–Pb dating
Hyperextension
Salt tectonics
Jurassic

ABSTRACT

The Meillon (Callovo-Oxfordian) and Mano (Tithonian) Formations are dolomitized carbonate reservoirs that actively produce oil and gas (Aquitaine Basin, France). In this study, the dolomitization conditions of their counterparts exhumed in the northwestern Pyrenees are detailed using a combination of field observations, petrography, fluid inclusion microthermometry, elemental and isotopic geochemistry, and carbonate U–Pb geochronology. Dolomitization occurred in several stages spanning from the Neocomian (pre-rift) to the Albian (syn-rift, associated with mantle exhumation and active salt tectonics). Both formations were first massively dolomitized in near-surface to shallow burial conditions during the Berriasian-Valanginian, likely triggered by the influx of marine-derived waters. Between the Barremian and the Albian, the Early Cretaceous rifting caused the upward influx of hot fluids associated with the partial to complete recrystallization of the initial dolomites. During the Albian, subsequent dolomites precipitated in both formations as high-temperature ($T > 160$ °C) vein- and pore-filling cement. Distinct fluid inclusion chlorinities and rare earth element patterns between the Meillon and Mano Formations point to fluid compartmentalization during this stage. Whereas dolomite cements indicate the involvement of evaporite-derived brines in the Meillon Formation, precipitation was likely related to clay-derived water in the Mano Formation. Lastly, a final episode of dolomite cementation occurred only in the vicinity of faults and volcanic intrusions during the Albian when the highest temperatures were recorded in both formations ($T > 250$ °C). These saddle dolomites precipitated from hydrothermal water with a mixture of mantle-, crustal-, and evaporite-derived waters channeled by faults and active diapirs. Subsequent quartz and calcite cement precipitation reveals a temperature decrease in a post-rift to inversion setting (post-Cenomanian) and indicates fluid compartmentalization between both formations. This study highlights the major control exerted by rifting, combined with the presence of diapiric salt, on dolomitization, making carbonate platforms of modern salt-rich passive margins potential targets for exploration.

## 1. Introduction

Dolomitization processes have been the subject of numerous studies in the last few decades, driven by the large number of hydrocarbon reservoirs made of dolomitized carbonate platforms (Braithwaite et al., 2004; Duggan et al., 2001; Nader and Swennen, 2004; Warren, 2000; White and Al-Aasm, 1997; Wierzbicki et al., 2006; Zenger and Dunham, 1980). Most investigations into the mechanisms responsible for dolomite precipitation, either as a cement or as a calcite replacement, are based on the study of ancient examples with a predominance of carbonate platforms (Barale et al., 2016; Barbier et al., 2015; Carmichael et al., 2008; Martín-Martín et al., 2015; Sharp et al., 2010). This is due to the absence of modern analogues of platforms impacted by massive dolomitization as well as the difficulty of precipitating dolomite at low temperatures in the laboratory within a reasonable timescale (Land, 1980, 1998). Despite the variety of genetic interpretations, these diagenetic studies generally agree that the main parameters required for dolomitization are (1) good rock permeability that allows (2) a high

* Corresponding author. Université de Pau et des Pays de l'Adour, E2S UPPA, CNRS, TOTAL, LFCR, UMR5150, 64000, Pau, France.
*E-mail address:* geoffreymotte@gmail.com (G. Motte).

https://doi.org/10.1016/j.marpetgeo.2021.104932
Received 14 September 2020; Received in revised form 15 January 2021; Accepted 17 January 2021
Available online 21 January 2021

water-rock ratio and (3) the input of Mg into the system (Hardie, 1987; Jonas et al., 2015; Kaczmarek and Sibley, 2011; Land, 1985; Lovering, 1969; Machel and Mountjoy, 1986; Sibley et al., 1994). The combination of these factors results in a variety of dolomitization models (see Machel, 2004; Warren, 2000). Examples of dolomitization are restricted to a single event either in an ancient carbonate platform with a well-known geodynamic evolution or in a modern carbonate platform, which provides the opportunity to identify the key control factors responsible for this diagenetic transformation and thus predict the distribution of dolomite in the carbonate platform (Adam and Rhodes, 1960; Barbier et al, 2011, 2012, 2015; Butler et al., 1982; Choquette and Hiatt, 2008; Deffeyes et al., 1965; Illing, 1959, 1964; Land, 1973; Sharp et al., 2010; Spencer-Cervato and Mullis, 1992; Stoakes, 1987; Wendte et al., 1998). In recent decades, many authors have described cases of pervasive dolomitization, which tends to be multi-phased, first relating to seawater in a near-surface to shallow burial environment and then caused by hydrothermal fluids channeled by structural pathways (Beckert et al., 2015; Biehl et al., 2016; Breesch et al., 2010; Cantrell et al., 2004; Di Cuia et al., 2011; Garaguly et al., 2018; Guo et al., 2016; Haeri-Ardakani et al., 2013a; Lukoczki et al., 2018; Nader et al., 2004; Tortola et al., 2020; Ye et al., 2019). In these numerous studies, temperature is one of the most critical parameters in the dolomitization reaction.

The foothills of the northwestern Pyrenees (southern Aquitaine basin) provide good examples of dolomitized carbonate platforms, which were used in the exploration of major oil and gas prospects in the 1950s, including the world-renowned Lacq gas field (Biteau et al., 2006). The platform contains two dolomite reservoirs deposited from the Bathonian to the Oxfordian (Meillon Formation) and during the Tithonian (Mano Formation). Their conditions of dolomitization, which were poorly characterized (Biteau et al., 2006; Grimaldi, 1988; Péré, 1987), have been recently revisited by Elias Bahnan (2019), Renard et al. (2018), and Salardon et al. (2017). These studies were accompanied by a complete reevaluation of the geodynamic evolution of the Pyrenees, highlighting the importance of Cretaceous rifting (Jammes et al., 2010a, 2009; Lagabrielle and Bodinier, 2008; Masini et al., 2014; Tugend et al., 2015 and many other studies) as the source of anomalous thermal regimes (Clerc et al., 2015; Hart et al., 2017; Incerpi et al., 2020; Jourdon et al., 2020; Lagabrielle et al., 2016; Lescoutre et al., 2019; Saspiturry, 2019; Vacherat et al., 2014). The inheritance of salt tectonic structures and the role played by salt at various scales were also emphasized in recent studies (Izquierdo-Llavall et al., 2020; Jourdon et al., 2020; Labaume and Teixell, 2020).

This Jurassic carbonate platform crops out in the *Chaînons Béarnais*, which constitute a succession of E-W-oriented salt-cored anticlines with several salt diapirs and ridges (Izquierdo-Llavall et al., 2020; Labaume and Teixell, 2020). In the *Chaînons Béarnais*, the dolomitization of the peritidal deposits that make up the Mano Formation is interpreted as occurring in several stages, beginning with an early limestone replacement followed by a dolomite cementation associated with tectonic fracturing and meteoric water circulation (Biteau et al., 2006; Elias Bahnan, 2019; Grimaldi, 1988). The Meillon Formation was also affected by multi-phase dolomitization with a complete replacement of the barrier-facies limestones followed by cementation associated with brecciation and fracturing at high temperatures (Péré, 1987). Very recently, Salardon et al. (2017), Incerpi et al. (2020), and Corre et al. (2018) demonstrated the role played by extensive hot fluid circulation during the Cretaceous rifting phase. As a result of these events, the two reservoirs present a fairly similar diagenetic evolution despite their distinct sedimentological facies (Grimaldi, 1988; Péré, 1987; Salardon et al., 2017). Nonetheless, the mechanism and origin of each dolomite event have yet to be studied in detail.

Using detailed mapping and petrography as well as conventional and more sophisticated analytical techniques such as carbonate U–Pb dating and secondary ion mass spectrometry (SIMS), this paper updates the diagenetic evolution of the northwestern Pyrenean Jurassic carbonate platform based on the study of the northernmost and most prominent ridge of the *Chaînons Béarnais*: the Mail Arrouy. The aims of this study are as follows: (1) to detail the diagenetic evolution of this carbonate platform, especially at the reservoir scale; (2) to unravel the mechanisms and fluids responsible for each dolomitization event; and (3) to assess the sedimentological and structural controls affecting the precipitation of dolomite.

## 2. Geological setting and stratigraphic framework

The Pyrenean orogen is an 450 km long E-W trending belt resulting from the N–S convergence of the European and Iberian Plates from the Late Santonian to the Miocene (Choukroune, 1992; Gong et al., 2008; Mouthereau et al., 2014; Puigdefàbregas and Souquet, 1986; Rosenbaum et al., 2002; Sibuet et al., 2004; Tugend et al., 2014). Separating the two foreland basins (Aquitanian and Ebro Basins), this ridge is subdivided into three structural domains: the North Pyrenean Zone comprised of pre-orogenic Paleozoic and Mesozoic deposits; the Axial Zone represented by Paleozoic rocks; and the South Pyrenean Zone formed by pre-rift to syn-orogenic Mesozoic and Cenozoic deposits (Fig. 1A; Choukroune, 1976). The Pyrenees exhibit a shortening gradient decreasing from E to W, which preserves the pre-orogenic structure of the western part (Masini et al., 2014; Mouthereau et al., 2014; Muñoz, 1992; Vergés et al., 1995). The Jurassic dolomite Meillon and Mano reservoir units crop out in the *Chaînons Béarnais,* located in the western North Pyrenean Zone (Fig. 1A).

The *Chaînons Béarnais* are the first landforms of the northwestern Pyrenees, located about 30 km from the Lacq gas field. These ridges include three salt-cored anticlines with an E-W trend. These structures that affect the Mesozoic deposits are interpreted as being partly inherited from pre-to syn-rift salt tectonics (Canérot et al., 2005; Izquierdo-Llavall et al., 2020; Labaume and Teixell, 2020; Lenoble and Canérot, 1992). The majority of the structural geometry of the most spectacular folds occurred in response to downbuilding in the salt and gravitational gliding of the cover along the margin slope prior to the shortening phase (Izquierdo-Llavall et al., 2020; Labaume and Teixell, 2020). This study focuses on the northernmost ridge, the Mail Arrouy Ridge, which was most affected by this shortening during the Eocene (Fig. 1B). This north-dipping monoclinal structure extends over 15 km between the Ossau and Aspe Valleys. It presents deposits spanning from the Triassic (ante-rift) to the Cenomanian (post-rift). Above the Upper Triassic deposits composed of evaporites, clays, and ophites, more than 1000 m of carbonates were deposited in a relatively stable tectonic context (James, 1998; Lenoble, 1992; Puigdefàbregas and Souquet, 1986). During the Lias, the depositional environment evolved from continental to open marine, with deposits passing from breccias during the Hettangian to belemnite marls and limestones during the Toarcian–Aalenian (Aussurucq Limestones; Canérot et al., 1990; Fauré, 2002; James, 1998; Lenoble, 1992, Fig. 1C). From the Bajocian to the early Bathonian, the morphology of the carbonate platform gradually shifted from a ramp to a rimmed shelf at the base of the dolomite Meillon Formation. The recurrence of a ramp morphology took place during the deposition of the end of the Meillon Formation and the Kimmeridgian Lons limestone Formation (James, 1998; Lenoble, 1992; Péré, 1989). During the Tithonian, the development of the dolomite Mano Formation, characterized by peritidal to supratidal environment deposits, was related to a widespread regression. The formation emerged in the late Tithonian to the Neocomian (Grimaldi, 1988), as evidenced by the presence of bauxites (Canérot et al., 1999; Combes et al., 1998; Grimaldi, 1988). The exposure was generalized in the *Chaînons Béarnais*, and increased southwestward, as evidenced by incision variations in the Upper Jurassic deposits (Fig. 1B; Castéras, 1970). Emersion probably resulted from both the relative sea-level fall and the regional uplift due to asthenospheric upwelling (Cox, 1989; Hallam, 2001; Haq et al., 1987; Ziegler and Cloetingh, 2004). In addition, salt tectonics, initiated at the beginning of the extension, resulted in the reactive salt diapir and ridge

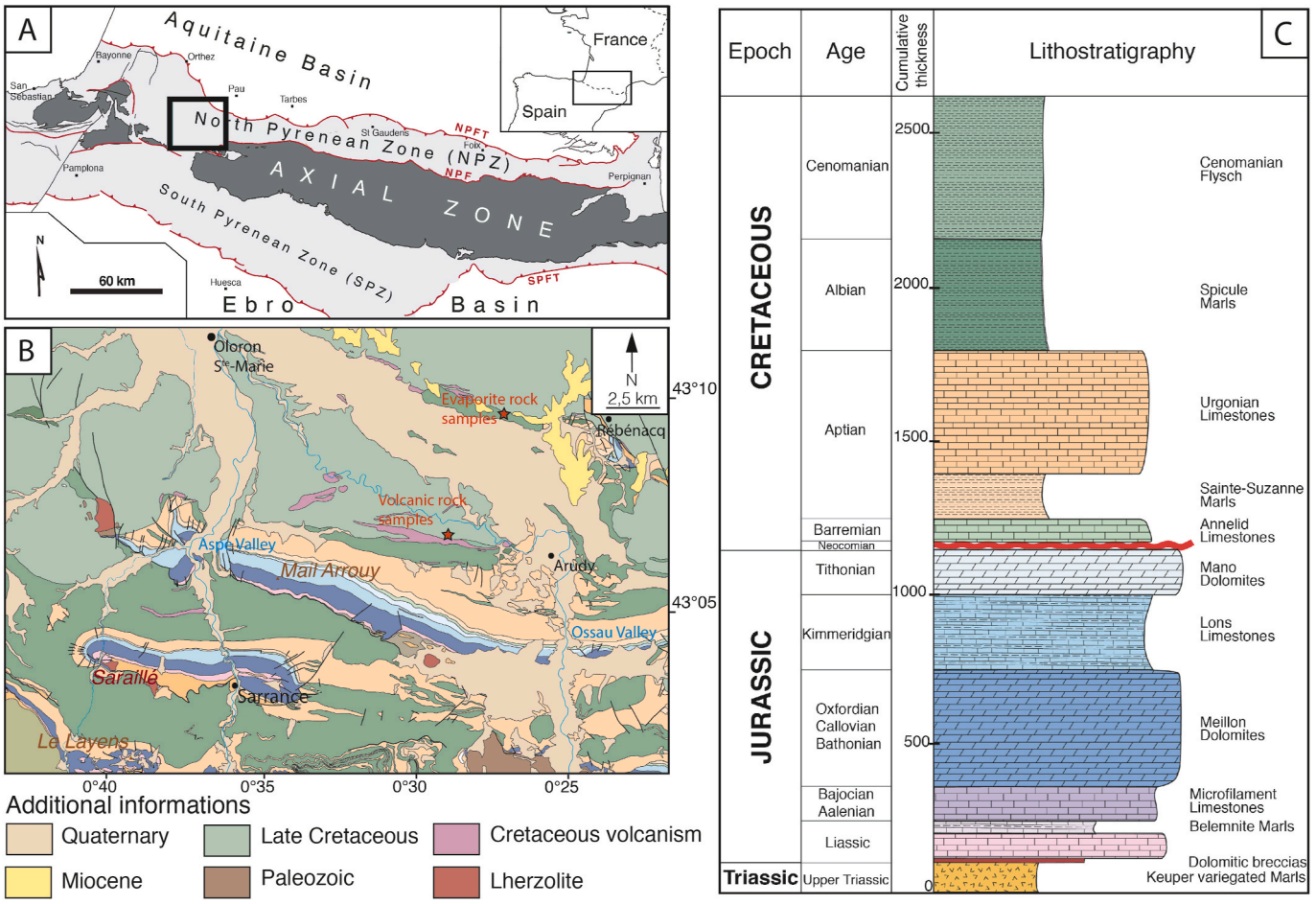


**Fig. 1.** A) Main structural domains of the Pyrenees with the location of the Chaînons Béarnais (after Clerc et al., 2016b); B) Geological map of the Chaînons Béarnais (modified after Castéras, 1970); the colors correspond to the lithostratigraphic log; C) Simplified lithostratigraphic log showing the different stratigraphic formations present in the Mail Arrouy. (For interpretation of the references to color in this figure legend, the reader is referred to the Web version of this article.)

development, associated with the strong folding of the pre-rift deposits and favoring local emersion (Canérot et al., 2005; Canérot and Lenoble, 1993; Izquierdo-Llavall et al., 2020; James and Canérot, 1999). From the Barremian to the Aptian, transgression took place from N to S, progressively flooding the emerged deposits. In the Mail Arrouy, it was first associated with the development of Annelid Limestones above the Jurassic deposits (Grimaldi, 1988; Lenoble, 1992), followed by the deposition of the Sainte-Suzanne Marls (Early Aptian), the ultimate seal of the Mano Formation (Biteau et al., 2006). All the Cretaceous deposits were controlled by a major rifting episode resulting from the rotation of the Iberian plate (Choukroune et al., 1973; Gong et al., 2008; Rosenbaum et al., 2002; Sibuet et al., 2004). The crust was first stretched and thinned by the ductile deformation of the lower crust, thus creating sedimentary space for the Aptian carbonates (Clerc et al., 2016; Clerc and Lagabrielle, 2014; Jammes et al, 2009, 2010b; Masini et al., 2014; Saspiturry et al., 2019). In the *Chaînons Béarnais*, the Early Aptian Sainte-Suzanne Marls are overlaid by a Late Aptian shallow carbonate platform mainly consisting of rudist build-ups (so-called Urgonian Limestones). These massive carbonates pass laterally to the Aptian Black Marls. From the Albian to the Cenomanian, the rifting led to the extreme thinning of the crust associated with mantle exhumation (Clerc and Lagabrielle, 2014; Corre et al., 2016; Jammes et al, 2009, 2010b; Lagabrielle et al., 2010; Lagabrielle and Bodinier, 2008; Masini et al., 2014; Tugend et al., 2014). The basin subsided heavily, with the widespread deepening of the depositional environments passing from reef to deep basinal deposits. From the Albian to the Maastrichtian, about 4000 m of turbidite deposits accumulated (Castéras et al., 1970). The thinning of the crust was associated with high geothermal gradients, causing high temperatures, low pressure metamorphism, and alkaline volcanism (Albarède and Michard-Vitrac, 1978; Azambre et al., 1992; Azambre and Rossy, 1976; Clerc et al., 2015; Ducoux et al., 2019; Golberg and Leyreloup, 1990; Hart et al., 2017; Izquierdo-Llavall et al., 2020; Lagabrielle et al., 2016; Lescoutre et al., 2019; Vacherat et al, 2014, 2016). From the early rifting at 125 Ma to the mantle exhumation, the thermal gradients increased by up to 80–100 °C/km in the central part of the basin (Hart et al., 2017). Starting during the Campanian, the convergence of the European and Iberian Plates resulted in a collision that reached a paroxysm during the Eocene (Choukroune, 1992; Choukroune et al., 1990; Mouthereau et al., 2014; Puigdefàbregas and Souquet, 1986; Teixell et al, 2016, 2018). The thermal gradients remained high during the post-rift and convergence stages. The thermal relaxation only occurred during the collision (50 Ma; Vacherat et al., 2014). During the contraction phase, tectonic lenses composed of crustal and mantle materials were incorporated into the Pyrenean orogenic wedge, leading to the exhumation of mantle bodies as in Urdach, *Turon de la Técouère*, and Lherz (Lagabrielle et al., 2010).

## 3. Methods

### 3.1. Field observations and sampling

Based on previous research (Castéras et al., 1970; Grimaldi, 1988; James, 1998; Lenoble, 1992) and our own observations, a 10 km$^2$ mapping of the study area was carried out in the Mail Arrouy, including

the boundaries of sedimentary formations, faults, magmatic dykes and sills, and breccia bodies (Fig. 2). The breccia description was based on Morrow (1982). Four stratigraphic sections were logged to constrain the lithologies of each formation. The sampling (n = 242) focused on the entire Mano and Meillon Formations outcropping in the Mail Arrouy, including the various brecciated bodies in the vicinity of faults. To obtain reference geochemical values, samples of volcanic rocks and evaporites were also collected (n = 8). A basaltic sill intercalated in the Cretaceous mapped near the Mail Arrouy Ridge was also sampled (Fig. 1B). Due to the lack of outcropping evaporites, we obtained samples directly from cores provided by Total SA, extracted from the Belair 1 well located 10 km north of the study area (Fig. 1B).

### 3.2. Analytical techniques

In total, 80 samples were selected for polished thin section preparation. Thin sections were partly stained with alizarin Red S solution to distinguish dolomite from calcite. The petrographic studies were performed using a Nikon Eclipse LV100ND optical microscope at the Laboratoire des Fluides Complexes et leurs Réservoirs (LFCR) (Pau, France). Overall, 50 thin sections were observed under cathodoluminescence (CL) using a Cathodyne system (OPEA) with an operating condition of 15 kV–18 kV and a gun current of 300–350 mA under a 60 mTorr vacuum at the LFCR. The limestone description was based on the Dunham (1962) classification, updated by Embry and Klovan (1971) and Wright (1992). The dolomite textures were described according to Gregg and Sibley (1987).

Fluid inclusion (FI) petrography was performed on 40 doubly-polished thick sections to identify FI assemblages according to Goldstein and Reynolds (1994) for each dolomite and calcite cement. The microthermometric measurement of dolomites only allowed homogenization temperatures to be determined due to the small size of the inclusions (<5–10 μm). Measurements were performed on a Linkam THMSG600 heating-cooling stage connected to a Nikon Eclipse LV100ND microscope at the LFCR. The equipment was calibrated using the following: (1) synthetic $H_2O$ pure fluid inclusion standard (ice melting ($T_{m\ ice}$) at 0.0 °C, homogenization temperature ($T_h$) at 374.1 °C); (2) synthetic $H_2O$–$CO_2$ inclusions ($CO_2$ melting at −56.6 °C, hydrate melting at +9.9 °C); and (3) synthetic $H_2O$–NaCl inclusions (eutectic temperature at −21.2 °C). The phase transition temperature had an uncertainty of around ±1–2 °C because of the small size of the inclusions.

Due to the lack of $T_{m\ ice}$ measurements, Raman spectroscopy was performed to determine the chlorinity of the fluid inclusions (Burke, 2001; Dubessy et al., 2002; Frezzotti et al., 2012). Analyses were performed in the Georessources laboratory (Nancy, France) with a LabRAM HR spectrometer (Horiba Jobin Yvon) equipped with a 600 g $mm^{-1}$ grating and an edge filter, as well as an excitation light provided by an $Ar^+$ laser at 457 nm at a power of 200 mW. Chlorinity was determined using the calibration of Caumon et al. (2013) following the procedure outlined in Caumon et al. (2015) to avoid the effect of mineral birefringence.

Major element compositions were measured in dolomite and calcite with an electron probe microanalyzer using a CAMECA SX100 from the PLateforme Aquitaine de CAractérisation des MATériaux (Pessac, France). The standard microprobe conditions were 40 nA and 20 kV using natural (andradite and celsian) and synthetic in-house standards.

Rare earth elements (REE) were measured on three thin sections by LA-ICP-MS with a Resonetics Resolution-SE 193 nm excimer laser system equipped with a S-155 large volume constant geometry chamber (Laurin Technic, Australia) at the Institute of Geological Sciences, University of Bern, Switzerland. Four transects were made across the dolomites, covering a total of 26 points in distinctive cement/matrix phases. The laser system was coupled to an Agilent 7900 quadrupole ICP-MS instrument. Samples were ablated in a He atmosphere and the aerosol mixed with Ar carrier gas before being transported to the ICP-

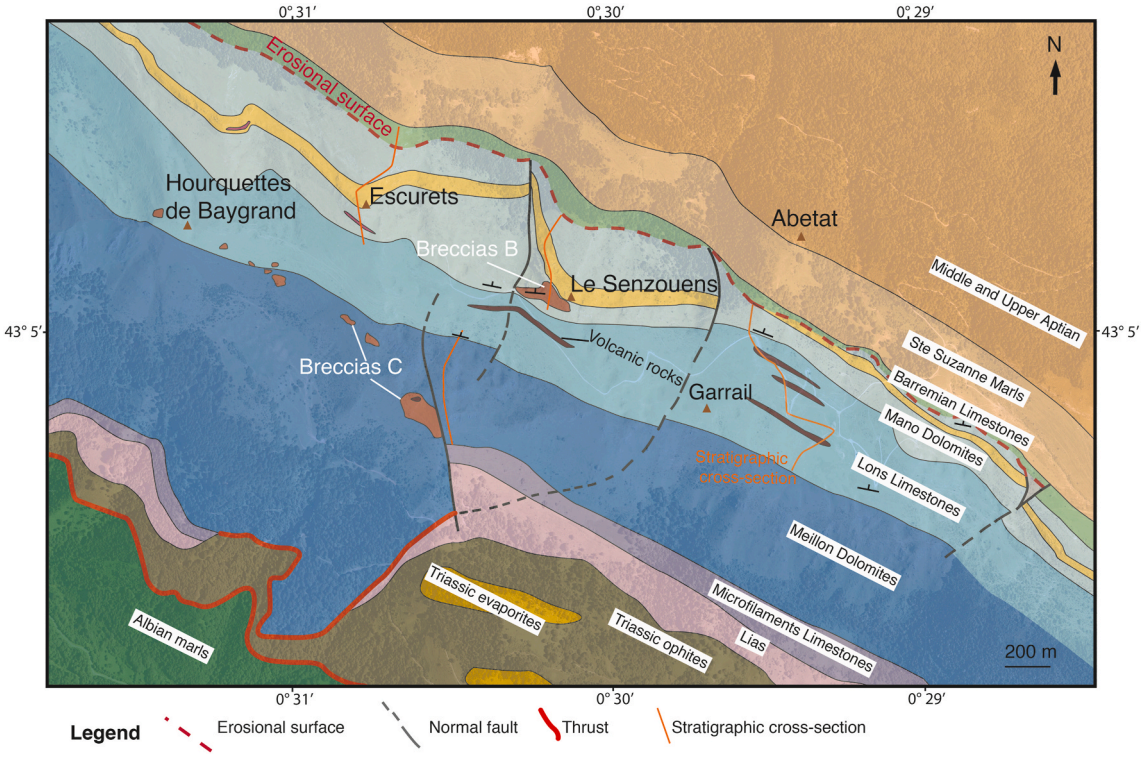


**Fig. 2.** Geological map of the studied area modified after Castéras (1970) and Grimaldi (1988). Note the differential erosion at the top of the Mano Formation due to the development of normal faults after deposition. Brecciated bodies (B and C) are present in the vicinity of faults and near the upper boundary of the Meillon Formation (see the text for details). Sedimentary breccias (A) are located near the base of the Mano Formation but are not visible at this scale. The color scale is the same as in Fig. 1. (For interpretation of the references to color in this figure legend, the reader is referred to the Web version of this article.)

MS. Measurement beam size was set at 80 μm, and the surface area of each measurement spot was cleaned with a pre-ablation of four pulses with a larger spot size. Total acquisition time for each analysis was 65 s (s), consisting of 30 s of gas background acquired with the laser switched off, 10 s of washout after pre-ablation cleaning, and 25 s of ablation signal. External calibration was performed using trace element-doped basaltic glasses GSD-1g (Jochum et al., 2010) and NIST 612 (Jochum et al., 2011), while Mg concentration, preliminarily determined by the electron probe microanalyzer, was used as the internal standard recovery. Standard controls were made every 10 measurements. Data were reduced by employing Iolite Igor Pro (version 7.08). The REE concentrations were normalized to the World Shale Average (WSA) as calculated by Piper (1974).

Bulk stable oxygen and carbon isotopes were analyzed on 13 powdered carbonate samples at the Institut des Sciences de la Terre de Paris (Paris, France). Due to the size of the microdrill bit (800 μm minimum), only four samples corresponded to a single phase of dolomite, with the others being a mixture of cement and dolomite matrix material. The dolomite samples were reacted under vacuum with 100% phosphoric acid at 70 °C for 10 min. $CO_2$ was purified in an automatic cryogenic trapping system and analyzed on the Kiel IV device coupled to a Delta V Advantage Thermo-Scientific. The measurements were reported as per mil (‰) deviation relative to the Vienna Pee Dee Belemnite (VPDB) standard and normalized to the NBS19 and NBS18. The acid fractionation of Rosenbaum and Sheppard (1986) was applied to the dolomite and Kim et al. (2007) to the calcite.

*In situ* oxygen and carbon isotope measurements were also performed on six polished and gold-coated thin sections with a SIMS Cameca IMS 1270 located at the Center de Recherche Pétrographique et Géochimique (Nancy, France). Eight transects were made across calcite and dolomite cements, covering a total of 189 points. To do so, two parallel transects (one for each isotope) were measured for each region of interest. Samples were sputtered with the 10 kV $Cs^+$ primary beam of 3 (for oxygen) and 2.7 (for carbon) nA intensity focused on 20 μm spots. Secondary negative ions of C and O were accelerated at 10 kV and analyzed at a mass resolution of about 5000 using the circular focusing mode of the IMS 1270 and a transfer optic of 150 μm (Rollion-Bard et al., 2003). The instrumental mass fractionation was determined using two standards analyzed conventionally for O and C isotopes: an ankerite standard (G119) for the dolomite ($\delta^{18}O_{SMOW} = +23.83 \pm 0.28$‰; $\delta^{13}C_{VPDB} = -0.38 \pm 0.17$‰) and a calcite standard (CC CigA) for the calcite ($\delta^{18}O_{SMOW} = +18.94 \pm 0.14$‰; $\delta^{13}C_{VPDB} = +1.04 \pm 0.10$‰) according to Rollion-Bard et al. (2003). The instrumental stability was verified regularly during each session. In the event of instrumental drift, a linear correction constrained by the difference in the standard value was applied to the measurements. The internal precision for a single measurement was ±0.1–0.2‰$_{(VPDB)}$ for $^{13}C/^{12}C$ and $^{18}O/^{16}O$ ratios. Rollion-Bard et al. (2003) experimented the reproducibility based on the repeated standard measurements and obtained ± 0.4‰$_{(VPDB)}$ for oxygen and ±0.65‰$_{(VPDB)}$ for carbon. The bulk values of large areas of cement were used to correct the $\delta^{18}O$ values obtained by the SIMS of the matrix effects (Rollion-Bard and Marin-Carbonne, 2011). Regarding the oxygen isotope values obtained by bulk analysis, the SIMS values are outlined in permil deviation from the VPDB standard (‰$_{VPDB}$).

The $^{87}Sr/^{86}Sr$ ratio was performed on 25 microdrilled samples: 18 were from dolomites and calcites in the Mano and Meillon Formations and 7 from volcanic rocks and evaporites. The Sr isotope analyses were performed at the Pole de Spectrométrie Ocean/Institut Universitaire Européen de la Mer (Plouzané, France). The Sr fractions were chemically separated following standard column chemistry procedures (Révillon et al., 2011). The Sr isotope compositions were measured in static mode on a Thermo TRITON and normalized to natural $^{86}Sr/^{88}Sr = 0.1194$ and to the standard solution NBS987 (recommended value of 0.710250). The standard deviation for laboratory standards within the samples was less than ±0.000005 (2σ).

Calcite U–Pb geochronology was conducted via a LA-ICPMS isotope mapping approach at the Institut des Sciences Analytiques et de Physico-Chimie pour l'Environnement et les Matériaux (Pau, France). All the samples were analyzed with a femtosecond laser ablation system (Lambda3, Nexeya, Bordeaux, France) coupled to an ICPMS Element XR (ThermoFisher Scientific, Bremen, Germany) fitted with the jet interface. This method is based on the construction of isotopic maps of the elements of interest for dating (U, Pb, Th) from ablation along lines, with ages calculated from the pixel values (Drost et al., 2018; Hoareau et al., in press). The laser and ICPMS parameters used for U–Pb dating are detailed in the Supplementary Material. Isotope maps were built from linear scans of 1.1 mm length at a repetition rate of 500 Hz. These lines of 25 μm height, separated by a distance of 25 μm, were obtained with a stage movement rate of 25 μm $s^{-1}$, corresponding to 44 s of analysis per line, followed by 15 s of break. There were 27–28 lines, resulting in a total analysis time ranging from 26.5 to 27.5 min for a surface of 0.74–0.77 $mm^2$. Prior to analysis, the samples were pre-cleaned with the laser using a stage movement rate of 200 μm $s^{-1}$. Only $^{238}U$, $^{232}Th$, $^{208}Pb$, $^{207}Pb$, and $^{206}Pb$ were selected, reaching a total mass sweep time of about ~60 ms. The selected unknowns were bracketed with the glass SRM NIST612 to normalize the lead ratios and drift correction of U/Pb ratios, followed by the WC1 calcite standard (Age 254.4 ± 6.4 Ma) for the final correction of the U/Pb ratio based on Roberts et al. (2017). The standards were analyzed in conditions similar to the unknowns, except that the isotopic maps were of smaller surface (~0.2 $mm^2$), corresponding to an analysis time of ~5 min. The Duff Brown Tank limestone (age 64.04 ± 0.67; Hill et al., 2016) was used as a secondary standard. To calculate the age, two approaches were followed. The first approach, less precise, consists of dividing the map into squares with a dimension of 5 × 6 pixels, equivalent to 125 μm × 150 μm and 15 s of analysis, and then calculating the mean and its uncertainty for each square. The second approach, similar to that of Drost et al. (2018), involves sorting the pixel ratio values using the $^{207}Pb/^{235}U$ ratio, clustering the data into discrete steps with a given number of pixels (here 30 pixels corresponding to 15 s of signal), and then calculating the mean and its uncertainty for each cluster. For both approaches, the age was obtained through a regression across the corresponding ellipses in the newly defined total−Pb/U–Th plot of Vermeesch (2020) using IsoplotR (Vermeesch, 2018). The goodness-of-fit to the data was assessed by calculating the mean squared weighted deviation (MSWD) on the discretized data. Ages are considered valid when statistical parameters are satisfying, and when similar ages (within uncertainty) are obtained for the two approaches. The calculated ages have uncertainties quoted as age ± x/y, where x corresponds to the confidence interval of the regression and y is with (1) additional analytical uncertainties (on $^{238}U/^{206}Pb$ of glass SRM NIST612) and (2) systematic uncertainties (on decay constant of $^{238}U$ (0.05%, 1s) on the $^{238}U/^{206}Pb$ ratio of WC1 as estimated by Roberts et al. (2017) (1.35%, 1s) and long-term excess uncertainty (1%, 1s)).

## 4. Results

### 4.1. Field observations

#### 4.1.1. Sedimentology

On its crest, the Mail Arrouy Ridge includes the Meillon and Mano dolostones as well as the Lons and Annelid Limestones. Over the 15 km length of the Mail Arrouy, dolomitization affects the entire volume of the Meillon and Mano Formations.

The Meillon Formation is characterized by around 350 m of high-energy environment deposits (Fig. 3A). In the lower and upper parts of the formation, the deposits range from wackestone (WST) to packstone (PST) with peloidal and oolitic content. In the middle part of the formation, they mainly consist of oolitic grainstone (GST; Fig. 3B). The entire Meillon Formation is affected by a fabric-destructive dolomitization. Distinguishing the initial texture is difficult in the presence of this pervasive pluri-micrometric sucrosic dolomite (Fig. 3C). Veins filled with white dolomite cement are present throughout the formation.

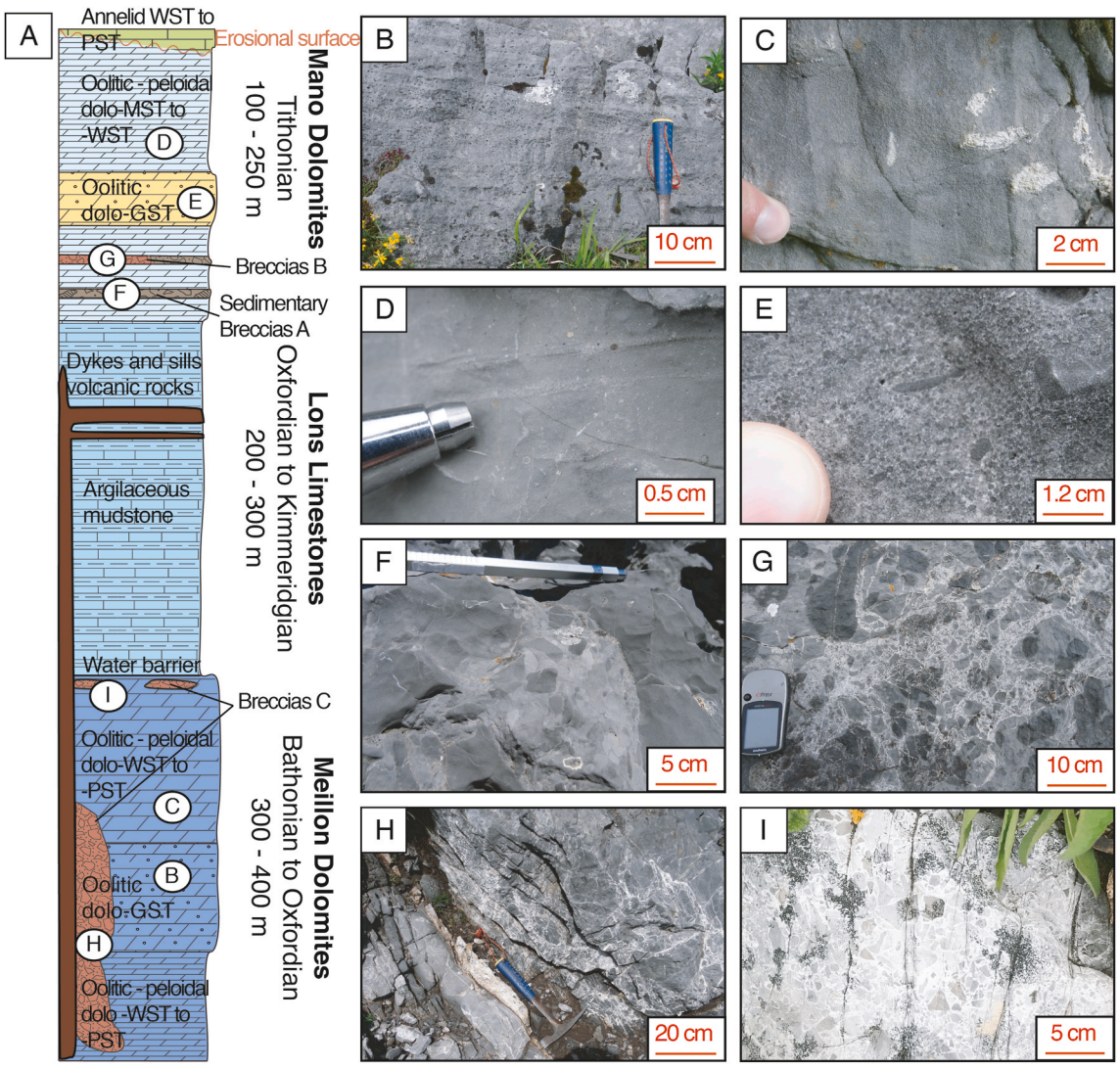


**Fig. 3.** A) Simplified sedimentological log of the Meillon, Lons, and Mano Formations with the location of the photographs; B to I) Field photographs of sedimentological facies and breccias of the Mail Arrouy. B) Oolitic doloGST with moldic porosity (Meillon Formation); C) Massive doloGST (Meillon Formation); D) DoloMST to doloWST with lenticular bedding (Mano Formation); E) Massive oolitic doloGST (Mano Formation). The dolomite oolite grains are dark, whereas white dolomite cemented the primary porosity; F) Polygenic breccia with sub-rounded clasts supported by a dolomite carbonate mud (Mano Formation); G) Breccias with monogenic unsorted dolomite clasts supported by a white dolomite cement (Mano Formation). This breccia (Breccia B) is located in the vicinity of the fault and passes laterally to the sedimentary breccia (Breccia A); H) Breccia C observed in the vicinity of a N–S fault (Meillon Formation); I) Angular dolomite clasts supported by white dolomite cement near the upper boundary of the Meillon Formation (Breccia C).

The Lons Formation consists of 250 m of barely changing argillaceous mudstone deposits (Fig. 3A). The formation boundaries with the Meillon and Mano Formations are evident, with a clear transition from limestone to dolostone without evidence of geometrical unconformity. No evidence of dolomite was observed.

Most deposits in the Mano Formation consist of dolomudstone (doloMST) or dolowackestone (doloWST) with pellets and oolites (Fig. 3D). Along the entire ridge, variations in thickness (from 250 to 30 m) are controlled by differential erosion during the Neocomian emersion. Dolograinstone (doloGST) with oolites represents the highest energy deposits (Fig. 3E). Interbedded monogenic or rarely polygenic sedimentary breccias (Breccia A) are present at the base of the Mano Formation (Fig. 3F). Breccia A exhibits a particulate rubble packbreccia morphology *sensu* Morrow (1982) (Fig. 4A-B). These carbonate mud-filled breccias have been interpreted as the result of emersion and an arid climate, which induced brecciation caused by karstification or even *Wadi* flows with a very low transport rate (Grimaldi, 1988). The morphology of the dolomite crystals replacing the carbonate matrix depends on the initial facies. In doloMST- or doloWST-type deposits, dolomites are micrometric in size and light-colored (Fig. 3D). As the energy of deposition increases, the size of the dolomites increases from several tens of micrometers to several hundreds of micrometers, becoming increasingly dark. In addition, veins cemented by pluri-micrometric white dolomites are present throughout the formation. Whereas veins have a width of several centimeters, the size of the dolomite cement crystals increases toward the center of the veins, ranging from micrometric to millimetric or centimetric in size.

Above the erosional truncation, the Annelid Formation was deposited in a shallow depositional environment during the flooding of the emerged platform. These 25 m thick limestone deposits range from WST to PST with annelid contents (Fig. 3A). No trace of dolomite was observed in these carbonates.

#### 4.1.2. *Structural observations*

The Mail Arrouy Ridge presents numerous N–S trending normal faults, which affect the entire Jurassic strata (Fig. 2) and are sealed by

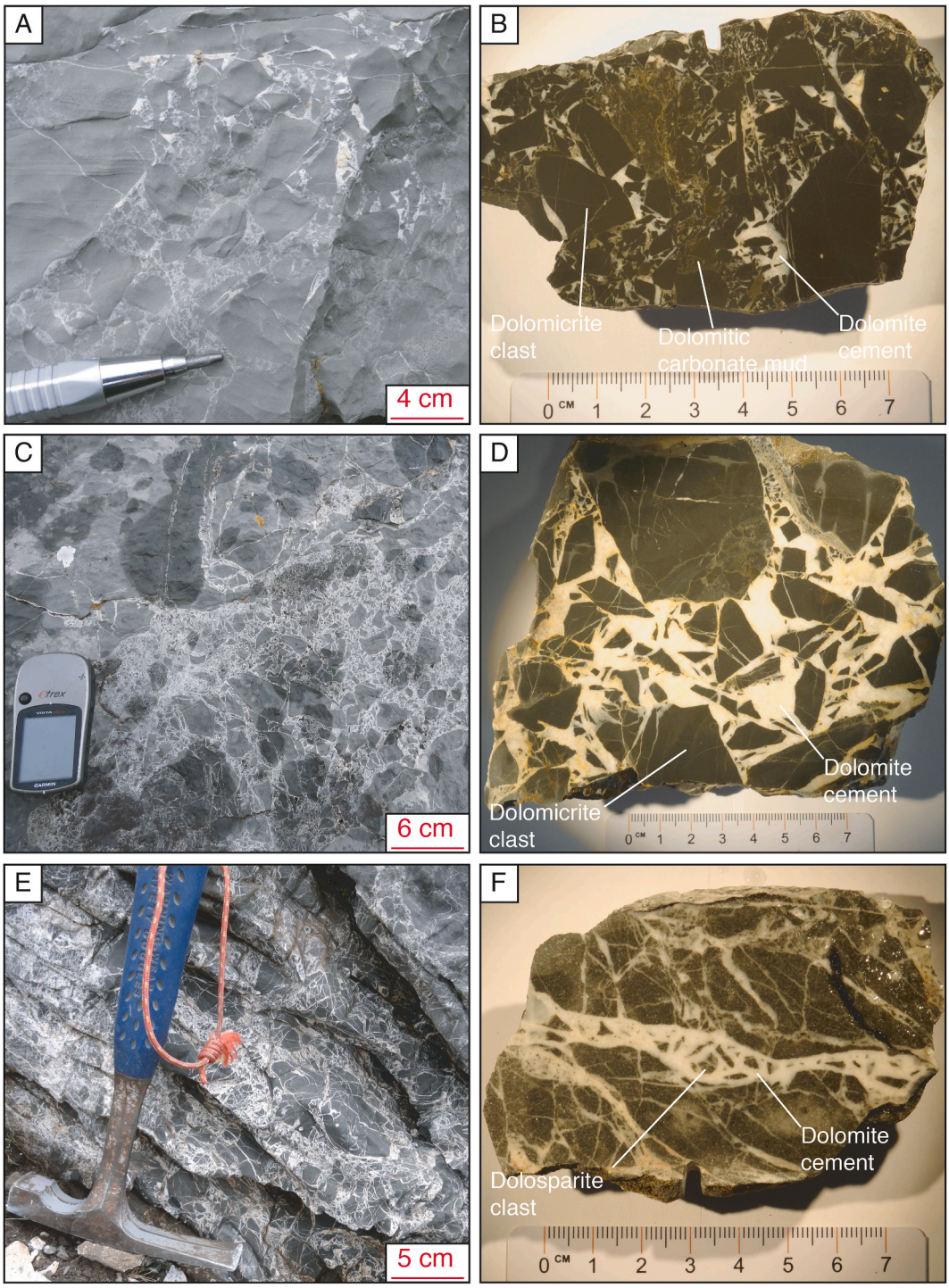


**Fig. 4.** Field photographs and corresponding polished samples illustrating the progressive transition from sedimentary Breccia A to dolomite Breccia B (A to D) as well as the texture of Breccia C (E, F). A and B) Sedimentary Breccia A with carbonate mud and tiny clasts partly replaced by white dolomite cement; C and D) Example of an almost complete replacement of the initial carbonate mud by white dolomite cement, located closer to a fault, forming a mosaic breccia texture (Breccia B); E and F) Breccia C with angular clasts supported by a white dolomite cement. Breccia C differs from B by the abundance of diffuse fracturing.

the Barremian Annelid Limestones (Grimaldi, 1988). The absence of any sedimentary wedge in the Mano Formation implies that fault activity occurred after the Jurassic carbonate deposition. Fault activity led to the differential erosion of the Mano Formation during the general uplift and exposure after the Tithonian. In the vicinity of the faults, morphologically distinct breccias are present in dyke-like geometries in both the Meillon and Mano Formations (Figs. 2 and 3A).

In the Mano Formation, these breccias (Breccia B) have monogenic angular clasts that rework the surrounding host rock (Fig. 4C-D), supported by a white dolomite cement (Fig. 3G). These breccias pass laterally to the aforementioned sedimentary breccias (Breccia A). As the distance from the fault zone increases, white dolomite cements become increasingly rare, leaving the initial organization of sedimentary Breccia A with monogenic clasts supported by carbonate mud (Fig. 4A-B). Breccia B presents a cemented rubble floatbreccia morphology. The partial to complete replacement of the initial millimetric elements and

the dolomite carbonate mud supported by the white dolomite cement occurs over a distance of 200–300 m from the faults (Figs. 2 and 3A). Due to this intense dolomitization, the initial sedimentary facies of the breccias is not easily identifiable. In some cases, the white dolomite cement is followed by quartz cementation.

In the Meillon Formation, the breccias (Breccia C) have monogenic, unsorted, and angular to sub-angular clasts supported by a white dolomite cement (Figs. 3H and Fig. 4E-F). The network of cemented veins is closely spaced to Breccia B of the Mano Formation, resulting in a cemented mosaic floatbreccia morphology. In some cases, quartz was also precipitated after the dolomite. Locally, these dolomite breccias are affected by a second brecciation event associated with calcite cementation. Breccia C is also observed near the upper boundary of the Meillon Formation in contact with the Lons Formation (Figs. 2 and Fig. 3A-I). Outside this domain and the faulted areas, breccia bodies are very limited in volume, and white dolomite cements are rarely observed except in tiny veins.

Finally, volcanic rocks are present as sills and dykes in the vicinity of the faults. They are injected into the fault zones in the Meillon, Lons, and Mano Formations (Figs. 2 and 3A).

In this study, the host rock and three distinct breccia types are used to characterize the diagenetic evolution of the entire Mano and Meillon Formations as well as that specific to the fault zones.

### 4.2. Petrographical observations

#### 4.2.1. Mano Formation

*4.2.1.1. Early diagenetic features.* In the grainstone facies, oolitic and peloidal grains have been partially dissolved, creating secondary porosity (Fig. 5A). The undissolved parts were also micritized before being dolomitized.

*4.2.1.2. Replacive dolomite.* The Mano Formation is affected by widespread dolomitization. In the mudstone and wackestone facies, the replacive dolomite crystals ($RD1_{Mano}$) are planar-S and range from 10 to 50 μm in size. They are gray to dark gray in color, turbid, and inclusion-rich. Under CL, the $RD1_{Mano}$ has a dull to dark-red luminescence.

$RD1_{Mano}$ completely overprints and thus postdates the sedimentary breccia (Fig. 5B). In the grainstone facies, the oolites and peloids are dolomitized by $RD1_{Mano}$, leaving the original fabric preserved (Fig. 5A).

*4.2.1.3. Dolomite cements.* Three dolomite cements can be distinguished on the basis of their crystal morphologies, size ranges, and CL luminescence. They occur as porosity-filling phases in grainstone facies (Fig. 5A), vein filling (Fig. 5C), and clast-supported cements in the diagenetic Breccia B (Fig. 5D). All cements are light gray to white in plane polarized light (PPL) and variably limpid. The grains do not exhibit compaction patterns (Fig. 5B), suggesting that the dolomite cementation affected the Mano Formation in a shallow burial context.

The first dolomite cement to precipitate ($DC2_{Mano}$) consists of planar-S crystals between 50 and 150 μm in size (Fig. 6A). It forms a thin rim located at the edge of the clasts or the host rock, with a light gray color. Locally in the breccias, $DC2_{Mano}$ replaces the host rock (Fig. 6B). Under CL, $DC2_{Mano}$ displays a dark red luminescence. Very small (≤5 μm) aqueous and solid inclusions are present in large quantities. $DC2_{Mano}$ was impacted by subsequent brecciation (Fig. 6C).

The second dolomite cement ($DC3_{Mano}$) precipitated after $DC2_{Mano}$, as shown by its common presence as $DC2_{Mano}$ crystal overgrowth (Fig. 6C). $DC3_{Mano}$ crystals are light gray, have a planar-E texture, and range from 300 to 1000 μm in size (Fig. 6A, B, D, and Fig. 5D). Locally, $DC3_{Mano}$ has a saddle texture due to its curved faces (Fig. 6D). CL observations highlight three successive growth zones characterized by distinct luminescence: DC3a in dark red, DC3b in red, and DC3c in alternating bright orange to red bands (Fig. 6A, B, D). The DC3b growth

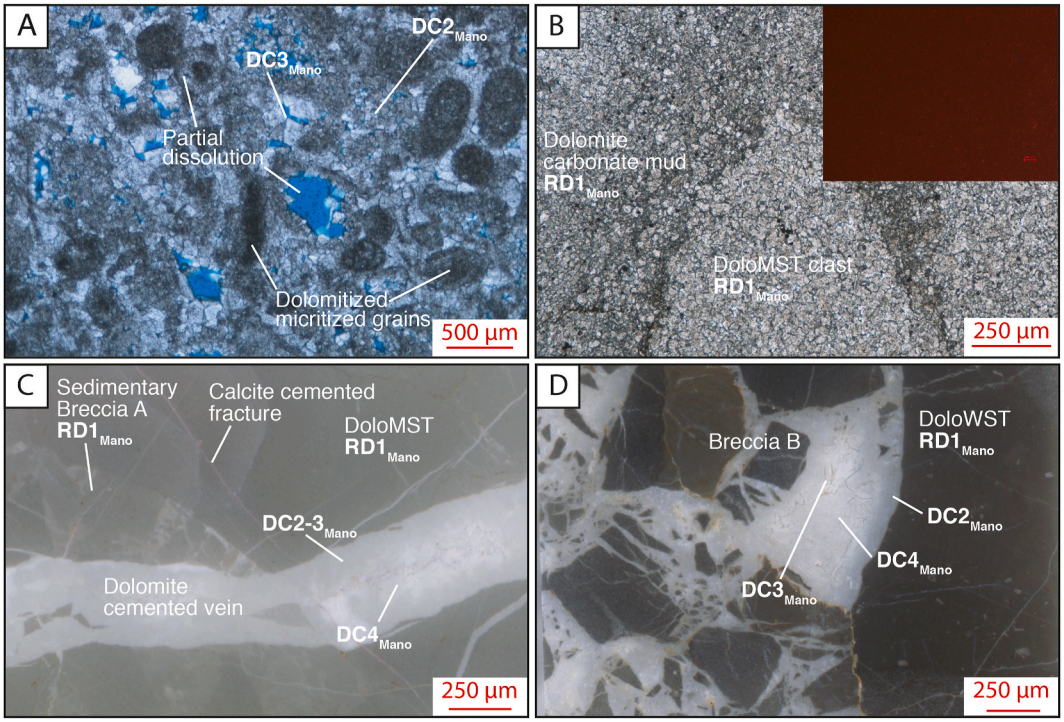


**Fig. 5.** Overview of the facies and breccias present in the Mano Formation in PPL with a scan of thin sections. A) DoloGST with fully micritized and partially dissolved dolomitized grains. The primary porosity is cemented by a white dolomite cement in planar-S to planar-E texture ($DC2_{Mano}$). Some planar-E dolomite crystals ($DC3_{Mano}$) precipitated in residual porosity; B) DoloMST in sedimentary Breccia A dolomitized by fine non-planar dolomite ($RD1_{Mano}$). Under CL, both the matrix and the mud share common CL luminescence; C) Thin section scan of a sedimentary breccia cross-cut by a dolomite-cemented vein. The matrix and Breccia A are fully dolomitized by $RD1_{Mano}$. The vein is cemented by a multi-phase dolomitization. In the center of the vein, dolomite crystals ($DC4_{Mano}$) are more limpid than near the edge ($DC2\text{-}3_{Mano}$); D) Example of dolomite cements observed in Breccia B comprising $DC2_{Mano}$, $DC3_{Mano}$, and $DC4_{Mano}$.

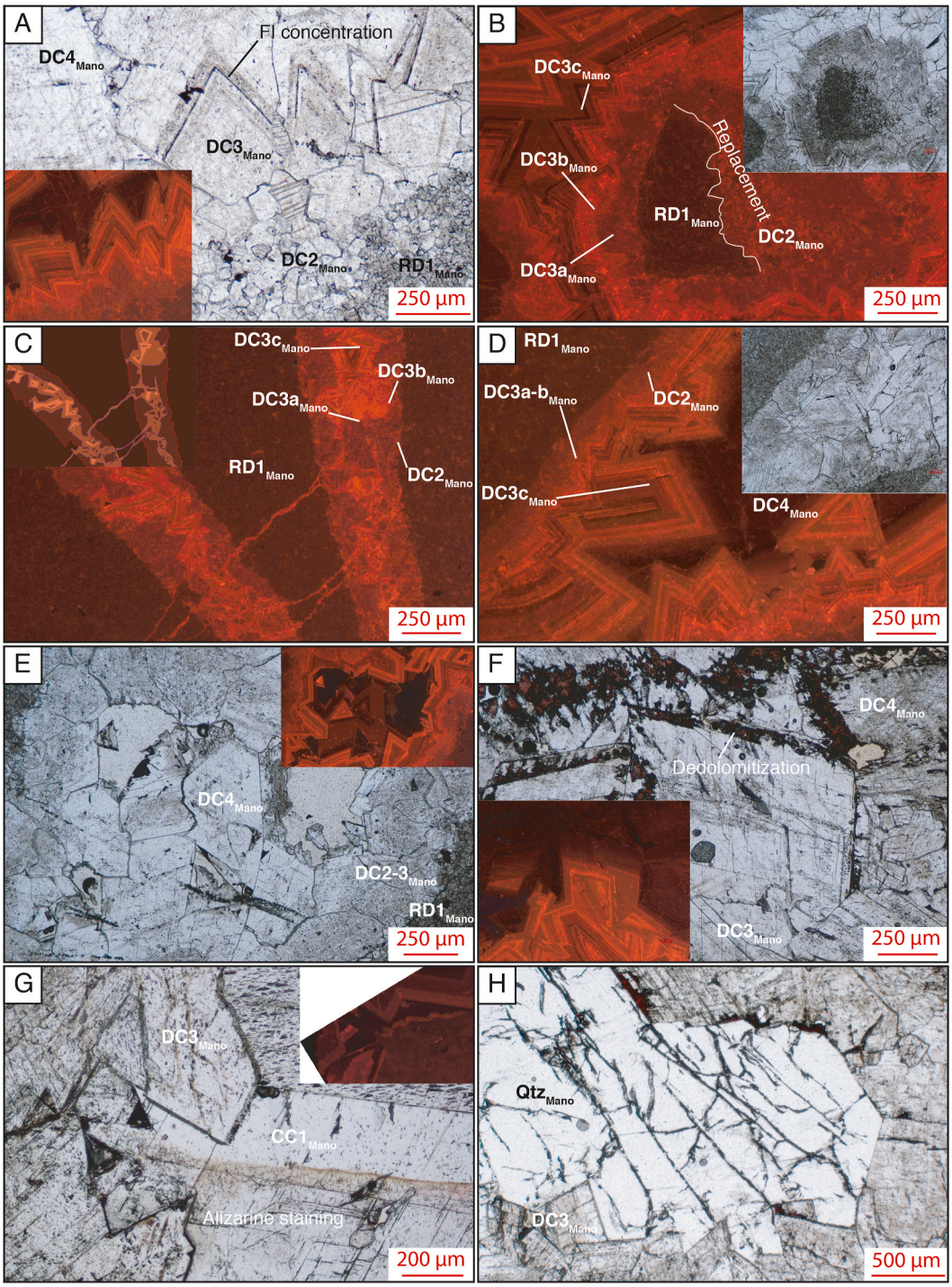


**Fig. 6.** Main characteristics of the cements present in the Mano Formation. A) Example of multi-phase dolomitization. The matrix was replaced by a fine non-planar dolomite $RD1_{Meillon}$. Vein-filling cements are made of fine planar-S to planar-E dolomite $DC2_{Mano}$ with planar-E dolomite $DC3_{Mano}$ overgrowths, followed by limpid saddle dolomite $DC4_{Mano}$; B) $RD1_{Mano}$, $DC2_{Mano}$, and $DC3_{Mano}$ observed under CL. In Breccia B, a clast initially dolomitized by $RD1_{Mano}$ is partially replaced by $DC2_{Mano}$; C) Dolomite-cemented veins in the host rock. The veins are similar to those in Breccia B except for the absence of $DC4_{Mano}$; D) Complete dolomite cementation with $DC3_{Mano}$ in saddle configuration; E) Large $DC4_{Mano}$ saddle crystals within Breccia B; F) Local dedolomitization of dolomite fringes as revealed by staining; G and H) Local cementation of the remaining intercrystalline porosity by dull-brown calcite $CC1_{Mano}$ (G) or quartz $Qtz_{Mano}$ (H). (For interpretation of the references to color in this figure legend, the reader is referred to the Web version of this article.)

zone displays numerous primary fluid inclusions aligned along the crystal boundaries (Fig. 6A).

The third dolomite cement ($DC4_{Mano}$) is observed only locally. It mainly occurs as large (300 µm–2000 µm) saddle blocky crystals in the breccias and the center of veins (Fig. 5C, D and Fig. 6E). This cement is limpid and contains only a few fluid inclusions. Under CL, it is characterized by a dull red luminescence (Fig. 6E, D). Locally, $DC4_{Mano}$ is impacted by dedolomitization, which is more pronounced along the crystal growth planes (Fig. 6F).

*4.2.1.4. Calcite and quartz cements.* Calcite cements are scarce. Locally, the stainings reveal calcite inside the dolomite crystals, which is

interpreted as resulting from dedolomitization (Fig. 6F). These calcite crystals (5–20 μm) are non-luminescent under CL. Given their tiny size, they cannot be related to other calcite cements.

Calcite cements ($CC1_{Mano}$) are also observed in veins and breccias. They are made of limpid, large (>1 mm) blocky crystals with a dull-brown CL luminescence (Fig. 6G).

Quartz ($Qtz_{Mano}$) is more common than calcite, but it is only observed locally. It is made of limpid, large (>500 μm) blocky crystals postdating $DC4_{Mano}$ in the veins and breccias (Fig. 5C, D). Dedolomitization features are often observed in the vicinity of the contacts between quartz and dolomite crystals (Fig. 6H).

### 4.2.2. Meillon Formation

*4.2.2.1. Early diagenetic features.* The wackestone facies located at the top of the Meillon Formation has not been completely dolomitized. The grains are partly micritized (Fig. 7A). Under CL, the micritic envelopes and the unaffected parts of the grains display an orange and dark orange luminescence, respectively (Fig. 7A). The remaining parts of the Meillon Formation, mainly made of oolitic packstone to grainstone, are completely dolomitized. The oolites were micritized before dolomitization and partially dissolved (Fig. 7B, C).

*4.2.2.2. Replacive dolomites.* The Meillon Formation presents two dolomite crystal textures that are non-fabric-preserving to partially fabric-preserving. First, a sucrosic replacive dolomite ($RD1_{Meillon}$) is observed locally (Fig. 7D). $RD1_{Meillon}$ crystals have a planar-E texture and range from 50 to 100 μm in size. The crystals have cloudy cores and clear fringes. Under CL, the cores generally have a dull red luminescence, whereas the outer fringes are bright red. However, some rhombs display irregular patches of red CL luminescence inside the cores, which is indicative of partial replacement (Fig. 7D). In the wackestone facies, the $RD1_{Meillon}$ dolomitization is not always complete, leaving isolated dolomite rhombs in the micrite matrix (Fig. 7A). In the grainstones, the dolomitization is complete, leaving an important intercrystalline porosity. Second, a replacive dolomite ($RD2_{Meillon}$) that commonly replaces and thus postdates $RD1_{Meillon}$ dolomite, affects almost the entire Meillon Formation. $RD2_{Meillon}$ crystals are light gray in PPL, have a planar-S texture, and range from 50 to 200 μm in size (Fig. 7B). In CL, they display a homogeneous dark red luminescence (Fig. 7C). $RD2_{Meillon}$ dolomite replaces all the uncompacted grains, leaving dark gray ghosts (Fig. 7B).

*4.2.2.3. Dolomite cements.* Dolomite cements are present in the intercrystalline porosity or veins of the host rock and Breccia C. These cements have three distinct crystal textures and CL luminescence.

Dolomite cement 2 ($DC2_{Meillon}$) is the first cement observed at the edge of the intercrystalline, moldic porosity, and veins of the host rock (Figs. 7C and 8A, B). $DC2_{Meillon}$ is also present in the brecciated bodies (Fig. 8A). This cement has a light gray color in PPL as well as a planar-S to planar-E dolomite crystal texture, ranging from 50 to 200 μm in size (Fig. 8B). Under CL, it displays a dark red luminescence.

Dolomite cement 3 ($DC3_{Meillon}$) occurs as an overgrowth of $DC2_{Meillon}$, partially or completely filling the remaining intercrystalline and moldic porosity of the host rock (Fig. 7C, D and Fig. 8B, C). This limpid cement is also associated with fractures that postdate $DC2_{Meillon}$ in the host rock and Breccia B (Fig. 8D, E). $DC3_{Meillon}$ crystals have a planar-S to planar-E dolomite texture and range from 50 to 300 μm in size. Under CL, $DC3_{Meillon}$ generally displays bright red luminescence (Fig. 8B). Locally, distinct CL fringes are observed in larger cement (Fig. 8C). $DC3_{Meillon}$ also forms an overgrowth on $RD1_{Meillon}$ crystals (Fig. 7D).

Dolomite cement 4 ($DC4_{Meillon}$) is the last in the Meillon Formation. $DC4_{Meillon}$ has a saddle dolomite crystal texture and ranges from 500 to 3000 μm in size. This light gray to limpid dolomite cement is only present locally in breccias as an overgrowth of $DC3_{Meillon}$ (Fig. 8D, F). Under

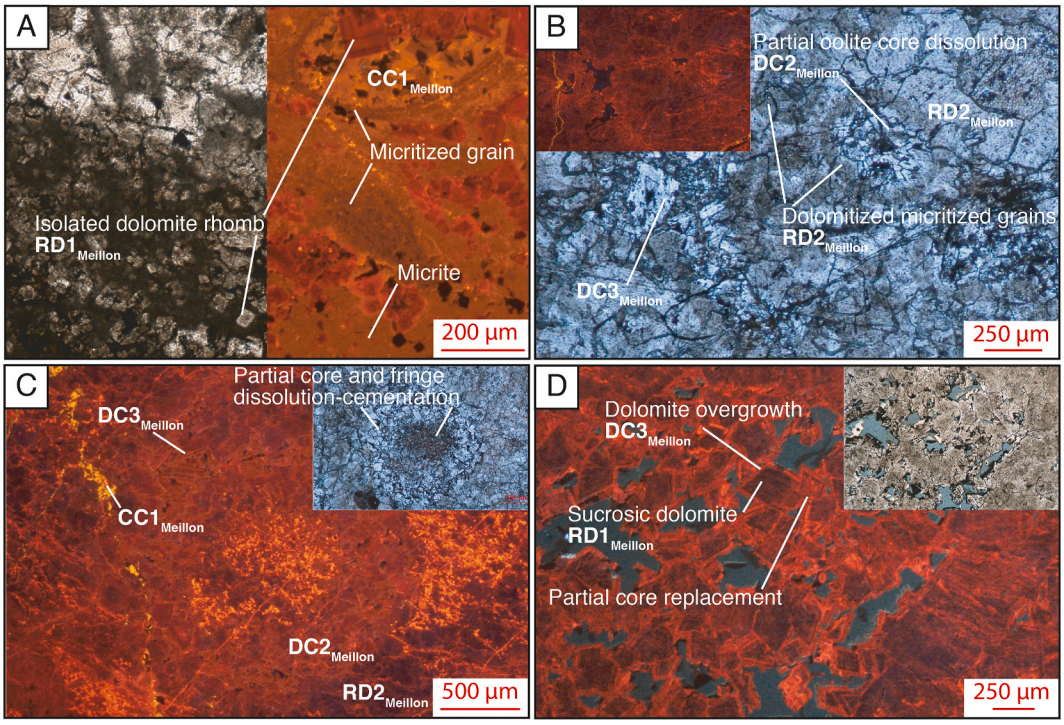


**Fig. 7.** Overview of cements and replacive dolomites present in the Meillon Formation. A) Near the upper boundary of the Meillon Formation, the dolomitization is partial, leaving the initial texture with isolated $RD1_{Meillon}$ rhombs in micrite. Calcite cements are also present ($CC1_{Meillon}$); B) Planar-S $RD2_{Meillon}$ dolomite in the oolitic grainstone facies. Secondary porosity was cemented by planar-S $DC2_{Meillon}$ and planar-E $DC3_{Meillon}$ dolomites; C) Example of oolite dissolution before dolomitization; D) Planar-E sucrosic dolomite $RD1_{Meillon}$. Secondary intercrystalline porosity was partially filled by $DC2_{Meillon}$ overgrowths. $DC2_{Meillon}$ locally replaces the core of $RD1_{Meillon}$ crystals.

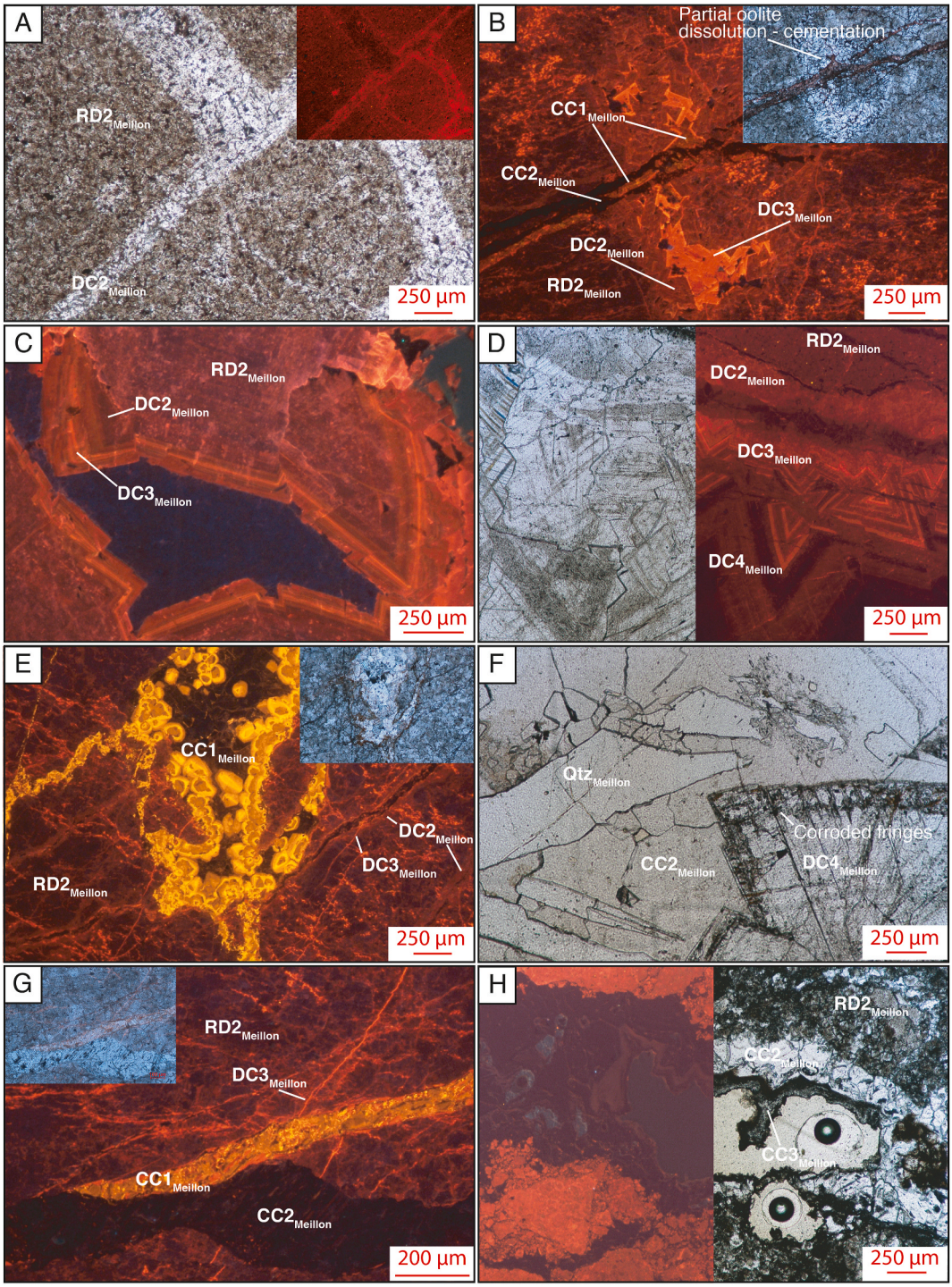


**Fig. 8.** Main characteristics of the cements present in the Meillon Formation (PPL and CL). A) $RD2_{Meillon}$ planar-S dolomite pervasively replacing the initial matrix. A vein affecting the host rock is filled by the planar-S dolomite cement $DC2_{Meillon}$; B) Illustration of the relative timing of dolomite and calcite cements in the grainstone facies. $DC2\text{-}3_{Meillon}$ dolomite cements postdate the replacive dolomite $RD1_{Meillon}$. They are followed by $CC1_{Meillon}$ calcite in veins and remnant porosity. $CC2_{Meillon}$ is the last vein-filling cement; C) Example of the succession of $RD2_{Meillon}$, $DC2_{Meillon}$, and $DC3_{Meillon}$ dolomites filling a vein; D) An additional saddle dolomitization stage $DC4_{Meillon}$ is observed in Breccia C; E) Dedolomitization or solution-cavity fills associated with $CC1_{Meillon}$ can locally affect the $RD2_{Meillon}$ dolomite matrix. Note the three distinct CL luminescences of $CC1_{Meillon}$; F) Additional $CC2_{Meillon}$ cements are observed in Breccia C. $DC4_{Meillon}$ cement presents corroded rims. The remaining intercrystalline porosity was first partially cemented by quartz $Qtz_{Meillon}$. After the $Qtz_{Meillon}$ fracturing, $CC2_{Meillon}$ has blocked the remnant porosity; G) Another illustration of the relative timing of cementation between dolomite and calcite. $DC3_{Meillon}$ is cross-cut by a vein filled by $CC1_{Meillon}$, which is cross-cut by a vein filled by $CC2_{Meillon}$; H) Calcite cement $CC2_{Meillon}$ supports clasts in Breccia C. It is followed by dripstone calcite $CC3_{Meillon}$.

CL, this cement displays a dark red luminescence with large bright fringes.

*4.2.2.4. Calcite and quartz cements.* The first calcite cement ($CC1_{Meillon}$) to precipitate in the Meillon Formation occurs in veins (Fig. 8G) and as pore-filling (Fig. 8B). It displays a drusy fabric with sub-euhedral to euhedral crystals ranging from 30 to 300 µm. Under CL, $CC1_{Meillon}$ exhibits three successive growth bands with distinct luminescence: an

orange luminescence, followed by a bright yellow external fringe, and in the coarsest pores or veins (up to 200 μm wide), a dull-brown color. Locally, $CC1_{Meillon}$ fills pores generated by the previous dolomite dissolution or directly replaces existing dolomite (Fig. 8E).

$CC2_{Meillon}$ is commonly observed as cement filling the residual intercrystalline porosity present in large veins of the host rock or in breccia cements (Fig. 8F, G, H). $CC2_{Meillon}$ fills fractures that postdate $CC1_{Meillon}$ and quartz cements (Fig. 8F, G). Locally, $CC2_{Meillon}$ supports dolomitized clasts in breccia C (Fig. 8H). It has a blocky fabric with limpid crystals ranging from 100 to 1000 μm in size. Under CL, $CC2_{Meillon}$ is non-luminescent (Fig. 8F, G, H). Locally, $CC2_{Meillon}$ replaces $DC4_{Meillon}$, leaving corroded rims (Fig. 8F). A last calcite cement with a dripstone fabric ($CC3_{Meillon}$) is observed only rarely in remnant pores (Fig. 8H).

Quartz cement ($Qtz_{Meillon}$) occurs in Breccia C (Fig. 8F), where it clearly postdates $DC4_{Meillon}$ but predates $CC2_{Meillon}$. The relative chronology between $Qtz_{Meillon}$ and $CC1_{Meillon}$ is not clear. The crystals are limpid with a size up to 500 μm.

### 4.3. Geochemistry

#### 4.3.1. Composition

The Mano dolomites are nearly stoichiometric (Table 1). Their Mg and Ca contents are consistent among the cements (less than 0.7 wt (wt) % variation). $RD1_{Mano}$ exhibits high contents of Fe and Si (around 3300 and 5800 ppm, respectively, in mean values) compared to $DC2\text{-}3_{Mano}$ dolomite cements (around 850 and 250 ppm, respectively, in mean values). The high Fe and Si values are likely a marker of detrital contamination. $DC4_{Mano}$ has the highest Fe content value (up to 3000 ppm) and the lowest Si content value (less than 200 ppm) of all the dolomite cements. Mn and Sr values remain low (<100 and <200 ppm, respectively) in all the dolomites.

The Meillon dolomites are also nearly stoichiometric (Table 1). $RD1_{Meillon}$ exhibits high Fe and Si contents (around 1800 and 2307 ppm, respectively, in mean values) compared to $RD2_{Meillon}$ (around 400 and 650 ppm, respectively, in mean values). $DC2_{Meillon}$ is Si-rich (around 2000 ppm) and presents a low content of Fe and Sr (around 300 and 150 ppm, respectively). $CC1_{Meillon}$ exhibits higher Mn and Sr contents (around 550 and 650 ppm, respectively) and low Si and Fe contents (around 350 and 300 ppm).

#### 4.3.2. Stable isotopes

Selected SIMS transects for the Meillon and Mano Formations are shown in Fig. 9 and Fig S3, while the mean $\delta^{18}O$ and $\delta^{13}C$ SIMS values of each diagenetic phase are presented in Fig. 10 and Table 2. Both SIMS and bulk data were obtained for $RD1_{Mano}$ and $DC4_{Mano}$. For $RD1_{Mano}$, the mean $\delta^{18}O$ and $\delta^{13}C$ values obtained by SIMS are −3.2 and + 3.1‰, respectively, whereas for bulk samples they are −0.80 and + 1.55‰, respectively. For $DC4_{Mano}$, the mean $\delta^{18}O$ and $\delta^{13}C$ values obtained by SIMS are −12.45 and 2.9‰, respectively, whereas for bulk samples they are −9.8 and + 1.2‰, respectively. The differences between the values measured by SIMS and on bulk samples are +2.41‰ for $RD1_{Mano}$ and +2.68‰ for $DC4_{Mano}$. The mean (+2.54‰) was used to correct for the matrix effect on $\delta^{18}O$ SIMS data for the other dolomite cements.

In the Mano Formation (Fig. 9), the $\delta^{18}O$ and $\delta^{13}C$ of $RD1_{Mano}$ (n = 7) range from −3.0 to +0.7‰ (mean = −0.7‰; median = −0.5%) and from +0.6 to +4.6‰ (mean = +3.1‰; median = +3.3‰), respectively. A significant negative shift in the $\delta^{18}O$ is measured between $RD1_{Mano}$ and $DC2_{Mano}$. The $\delta^{18}O$ and $\delta^{13}C$ of $DC2_{Mano}$ (n = 22) range from −14.7 to −11.5‰ (mean = −13.6‰; median = −13.7‰) and from −1.7 to +5.7‰ (mean = +3.2‰; median = +3.5‰), respectively. The $\delta^{18}O$ and $\delta^{13}C$ of $DC3_{Mano}$ (n = 43) range from −14.6 to −9.4‰ (mean = −11.9‰; median = −11.9‰) and from +0.8 to +5.2‰ (mean = +3.4‰; median = +3.5‰), respectively. The last cement $DC4_{Mano}$ is characterized by a positive shift in oxygen isotope values (Fig. 9). The $\delta^{18}O$ and $\delta^{13}C$ of $DC4_{Mano}$ (n = 29) range from −13.1 to −7.9‰ (mean = −9.9‰; median

**Table 1**
Elemental composition (microprobe data) of the investigated cements in both the Mano and Meillon Formations.

| | | Ca (wt%) | Mg (wt%) | Si (ppm) | Mn (ppm) | Fe (ppm) | Sr (ppm) |
|---|---|---|---|---|---|---|---|
| $RD1_{Mano}$ | Max. | 21.1550 | 13.268 | 24,729 | 266 | 83,810 | 512 |
| | Min. | 16.85 | 11.198 | 168 | bdl | 97 | bdl |
| | Mean | **20.3301** | **12.5831** | **5793** | **59** | **3275** | **74** |
| Normalized to six oxygens | | *0.965* | *0.985* | *0.039* | *0* | *0.011* | *0* |
| $DC2_{Mano}$ | Max. | 21.834 | 13.167 | 834 | 322 | 1940 | 323 |
| | Min. | 20.563 | 12.531 | 103 | 51 | 223 | bdl |
| | Mean | **21.0479** | **12.8617** | **269** | **171** | **747** | **96** |
| Normalized to six oxygens | | *0.994* | *1.001* | *0.002* | *0.001* | *0.003* | *0* |
| $DC3_{Mano}$ | Max. | 21.486 | 13.648 | 1279 | 370 | 3588 | 466 |
| | Min. | 14.787 | 11.322 | bdl | 53 | bdl | bdl |
| | Mean | **20.8001** | **12.7671** | **233** | **216** | **996** | **101** |
| Normalized to six oxygens | | *0.990* | *1.004* | *0.002* | *0.001* | *0.004* | |
| $DC4_{Mano}$ | Max. | 21.354 | 13.236 | 455 | 292 | 8245 | 170 |
| | Min. | 18.24 | 11.7180 | 38 | bdl | 354 | bdl |
| | Mean | **20.4447** | **12.6566** | **183** | **106** | **3050** | **6** |
| Normalized to six oxygens | | *0.984* | *1.004* | *0.001* | *0* | *0.011* | |
| $RD1_{Meillon}$ | Max. | 24.4488 | 12.58 | 21,991 | 3265 | 6891 | 512 |
| | Min. | 17.937 | 10.011 | 2 | bdl | 607 | bdl |
| | Mean | **20.7248** | **11.4378** | **2307** | **296** | **1765** | **74** |
| Normalized to six oxygens | | *1.035* | *0.941* | *0.016* | *0.001* | *0.006* | |
| $RD2_{Meillon}$ | Max. | 25.853 | 12.976 | 904 | 398 | 671 | 715 |
| | Min. | 21.9303 | 10.0012 | 327 | bdl | 135 | bdl |
| | Mean | **22.9991** | **12.0602** | **652** | **129** | **368** | **173** |
| Normalized to six oxygens | | *1.070* | *0.925* | *0.004* | *0* | *0.001* | |
| $DC2_{Meillon}$ | Max. | 23.045 | 14.193 | 6980 | 607 | 418 | 371 |
| | Min. | 21.804 | 13.355 | 612 | 210 | 119 | bdl |
| | Mean | **22.5138** | **13.7310** | **2250** | **396** | **247** | **120** |
| Normalized to six oxygens | | *0.989* | *0.995* | *0.014* | *0.001* | *0.001* | |
| $CC1_{Meillon}$ | Max. | 41.252 | 0.3753 | 845 | 3158 | 831 | 1186 |
| | Min. | 38.286 | bdl | 52 | bdl | bdl | 168 |
| | Mean | **40.3069** | **0.0758** | **364** | **567** | **287** | **665** |
| Normalized to six oxygens | | *1.990* | *0.005* | *0.003* | *0.002* | *0.001* | |

bdl: below detection limit.

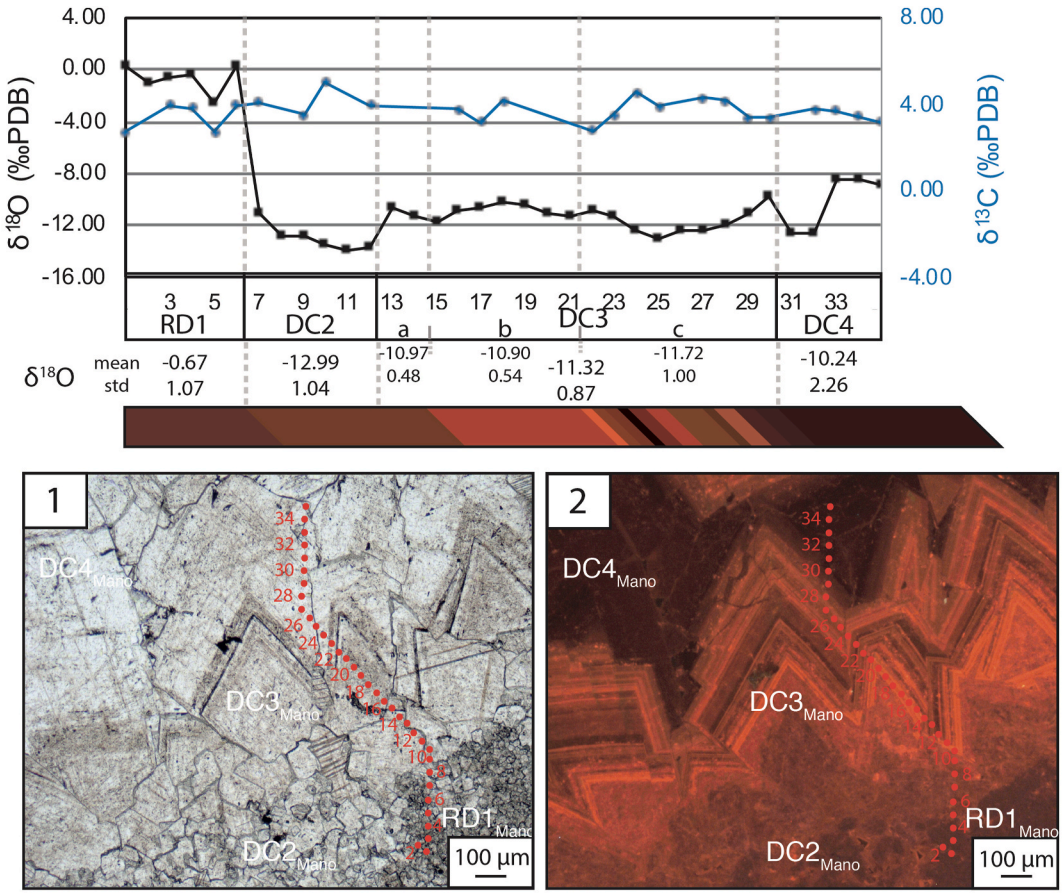


**Fig. 9.** Detailed SIMS $\delta^{18}O$ and $\delta^{13}C$ values obtained from a transect of Mano dolomite cements. The location of the transect is shown in images 1 (PPL) and 2 (CL). $\delta^{18}O$ exhibits a significant negative shift between $RD1_{Mano}$ matrix and $DC2_{Mano}$, whereas the $\delta^{13}C$ has constant values along the entire transect.

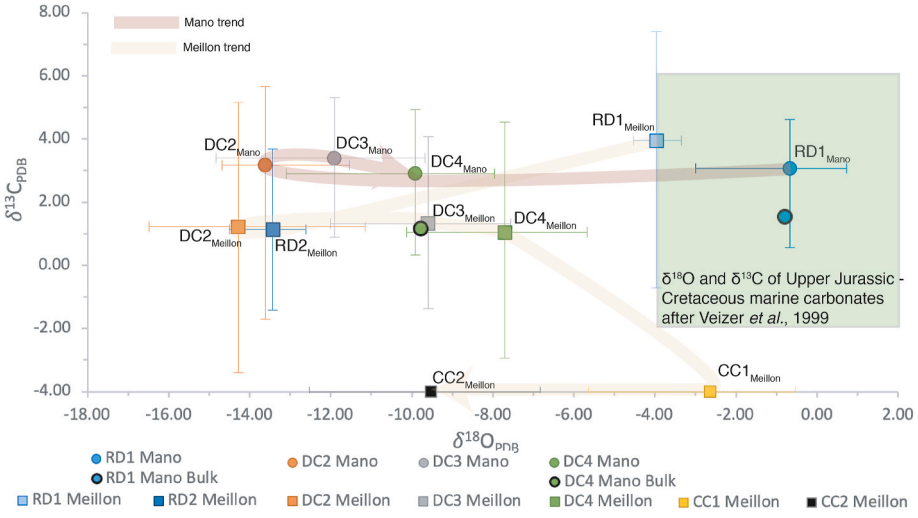


**Fig. 10.** Mean $\delta^{18}O$ and $\delta^{13}C$ values of all the dolomites measured by SIMS, with the minimum and maximum values represented by bars. The Upper Jurassic and Cretaceous marine carbonate values are represented in the green box (Veizer et al., 1999). (For interpretation of the references to color in this figure legend, the reader is referred to the Web version of this article.)

= −10.0‰) and from +0.3 to +4.9‰ (mean = +2.9‰; median = +3.3‰), respectively.

In the Meillon Formation, five SIMS transects were performed, covering all the dolomites, $CC1_{Meillon}$ and $CC2_{Meillon}$. Similar to the Mano Formation, the Meillon dolomites exhibit strong oxygen isotopic variations. The $\delta^{18}O$ and $\delta^{13}C$ of $RD1_{Meillon}$ (n = 4) range from −4.5 to −3.3‰ (mean = −4.0‰; median = −4.0‰) and from −0.7 to +7.4‰ (mean = +3.9‰; median = +4.5‰), respectively, while $RD2_{Meillon}$ (n = 3) has $\delta^{18}O$ values between −14.5 and −12.6‰ (mean = −13.4‰; median = −13.2‰) and $\delta^{13}C$ values between −1.4 and + 3.7‰ (mean = +1.1‰; median = +1.1‰). $DC2_{Meillon}$ (n = 21) exhibits $\delta^{18}O$ values close to $RD2_{Meillon}$, ranging from −16.5 to −11.1‰ (mean = −14.3‰;

**Table 2**
Geochemical characterization of all the diagenetic phases observed in the Mano and Meillon Formations of the Mail Arrouy chaînon, including stable isotopes ($\delta^{18}O$, $\delta^{13}C$, $^{87}Sr/^{86}Sr$ measured, and $\delta^{18}O$ parent water calculated) and FI analysis (microthermometry and chlorinity determination).

| Sample | Stable isotopes | | | | | | | | | | Sr isotopes | | | | Primary fluid inclusions | | | | | | | | |
|---|---|---|---|---|---|---|---|---|---|---|---|---|---|---|---|---|---|---|---|---|---|---|---|
| | Corrected $\delta^{18}O_{PDB}$ | | | | Parent water $\delta^{18}O_{SMOW}$ | | | $\delta^{13}C_{PDB}$ | | | $^{87}Sr/^{86}Sr$ | | | | Microthermometry | | | | Chlorinity | | | | |
| Type | Mean | Min | Max | n | Mean | Min | Max | Mean | Min | Max | n | Mean | Min | Max | n | Mode | Min | Max | n | Mean | Min | Max | n |
| $RD1_{Mano}$ | −0.7 | −3.0 | 0.7 | 7 | | | | 3.1 | 0.6 | 4.6 | 6 | 0.707633 | 0.707461 | 0.707798 | 3 | | | | | | | | |
| $DC2_{Mano}$ | −13.6 | −14.7 | −11.5 | 22 | 5.4 | 2.7 | 8.2 | 3.2 | −1.7 | 5.7 | 18 | 0.708743 | 0.708484 | 0.709001 | 2 | 200 | 169 | 204 | 7 | 1.6 | 0 | 3.6 | 3 |
| $DC3a_{Mano}$ | −13.1 | −14.4 | −10.2 | 7 | 5.6 | 0.9 | 9.6 | 4.1 | 3.4 | 4.9 | 3 | | | | | 160 | 146 | 193 | 21 | 1.5 | 0 | 4.9 | 4 |
| $DC3b_{Mano}$ | −11.0 | −12.6 | −9.7 | 9 | | | | 3.9 | 2.5 | 5.1 | 5 | | | | | | | | | | | | |
| $DC3c_{Mano}$ | −12.0 | −14.6 | −9.4 | 19 | 6.8 | 3.0 | 9.9 | 3.5 | 0.8 | 5.2 | 17 | | | | | 200 | 171 | 196 | 20 | 4.9 | 0 | 12.4 | 11 |
| $DC4_{Mano}$ | −9.9 | −13.1 | −8.0 | 29 | 12.8 | 6.2 | 16.8 | 2.9 | 0.3 | 4.9 | 23 | 0.710087 | 0.710043 | 0.710130 | 2 | 280 | 196 | 320 | 12 | 19.7 | 10.2 | 26.9 | 4 |
| $RD1_{Meillon}$ | −4.0 | −4.5 | −3.3 | 4 | | | | 3.9 | −0.7 | 7.4 | 4 | 0.707555 | 0.707520 | 0.707590 | 2 | | | | | | | | |
| $RD2_{Meillon}$ | −13.4 | −14.5 | −12.6 | 3 | | | | 1.1 | −1.4 | 3.7 | 2 | 0.707705 | 0.707630 | 0.707780 | 2 | | | | | | | | |
| $DC2_{Meillon}$ | −14.3 | −16.5 | −11.1 | 21 | 6.9 | 4.6 | 10.1 | 1.2 | −3.4 | 5.2 | 12 | 0.707875 | 0.707821 | 0.707929 | 2 | 230 | 230 | 232 | 4 | | | | |
| $DC3_{Meillon}$ | −9.6 | −10.8 | −8.6 | 4 | 9.7 | 7.4 | 11.6 | 1.3 | −1.4 | 4.1 | 3 | | | | | 200 | 179 | 210 | 18 | | | | |
| $DC4_{Meillon}$ | −7.7 | −10.1 | −5.7 | 12 | 14.5 | 11.4 | 17.1 | 1.0 | −2.9 | 4.5 | 7 | 0.708010 | 0.707900 | 0.708120 | 2 | 260 | 238 | 260 | 6 | 18.2 | 12.7 | 23.6 | 6 |
| $Qtz_{Meillon}$ | | | | | | | | | | | | | | | | 170 | 136 | 205 | 19 | 5.6 | 2.5 | 7.5 | 12 |
| $CC1_{Meillon}$ | −2.6 | −5.6 | −0.6 | 13 | | | | | | | | | | | | | | | | | | | |
| $CC2_{Meillon}$ | −9.5 | −12.5 | −6.8 | 11 | 8.1 | 4.5 | 9.8 | | | | | 0.707770 | | | 1 | 140 | 142 | 158 | 5 | 18 | 17.7 | 18.2 | 2 |

median = −14.5‰). The associated $\delta^{13}C$ values range from −3.4 to +5.1‰ (mean = +1.2‰; median = +1.2‰). The $\delta^{18}O$ and $\delta^{13}C$ of $DC3_{Meillon}$ (n = 4) range from −10.8 to −8.6‰ (mean = −9.6‰; median = −9.5‰) and from −1.4 to +4.1‰ (mean = +1.3‰; median = +1.2‰), respectively. The last dolomite cement $DC4_{Meillon}$ (n = 29) has fewer negative $\delta^{18}O$ values ranging from −10.1 to −5.7‰ (mean = −7.7‰; median = −8.0‰). The associated $\delta^{13}C$ values range from −2.9 to +4.5‰ (mean = +1.0‰; median = +1.6‰). The $\delta^{18}O$ values of $CC1_{Meillon}$ (n = 13) and $CC2_{Meillon}$ (n = 11) range from −5.6 to −0.5‰ (mean = −2.6‰; median = - 1.9‰) and −12.5 to −6.8‰ (mean = −9.5‰; median = 8.9‰), respectively ($\delta^{13}C$ could not be measured).

### 4.3.3. Strontium isotopes

For the Mano Formation, the Sr isotope ratio of $RD1_{Mano}$ varies from 0.707461 to 0.707798 (Fig. 11 and Table 2). The small size of the $DC2_{Mano}$ and $DC3_{Mano}$ cements prevented their separate analysis. The mixture of these two cements (n = 2) shows $^{87}Sr/^{86}Sr$ ratios of 0.708484 and 0.709001. The two measurements made for the final dolomite cement $DC4_{Mano}$ give values of 0.710043 and 0.710130.

For the Meillon Formation, $RD2_{Meillon}$ dolomite (n = 2) exhibits $^{87}Sr/^{86}Sr$ ratios of 0.707630 and 0.707780. The analysis of the mixture between $RD1_{Meillon}$ and $DC2_{Meillon}$ (n = 2) gives a Sr isotope ratio between 0.707520 and 0.707590. The mixture of $DC2_{Meillon}$ and $DC3_{Meillon}$ (n = 2) gives $^{87}Sr/^{86}Sr$ ratios of 0.707821 and 0.707929. For $DC4_{Meillon}$ (n = 2), the Sr isotope ratios vary from 0.707900 to 0.708120. The Sr isotope ratio of one calcite cement $CC2_{Meillon}$ was 0.707770. The calcite matrix present in the upper part of the Meillon Formation (n = 2) has Sr isotope ratios varying from 0.707715 to 0.707770.

The $^{87}Sr/^{86}Sr$ ratios of anhydride (n = 2) and halite samples (n = 2) of Triassic evaporites from the Belair well vary from 0.707825 to 0.707827 and from 0.708560 to 0.708565, respectively.

The Sr isotope ratios of the volcanic sills sampled in the Lons Formation (n = 2) are 0.705322 and 0.705348. The $^{87}Sr/^{86}Sr$ ratio of the basaltic rocks embedded in the Albian turbidites (n = 1) is 0.705851.

### 4.3.4. U–Pb dating

Accurate total−Pb/U–Th ages could be obtained for six samples corresponding to $RD1_{Mano}$, $DC2_{Mano}$, $RD2_{Meillon}$, and $DC4_{Meillon}$. These results, presented on Tera-Wasserburg plots, are provided in Fig. S1 for the first approach (subdivision of the isotopic image in 150 μm × 125 μm squares), and in Fig. 12 for the second approach inspired by Drost et al. (2018). For $RD1_{Mano}$, two samples could be analyzed. For one sample, 136.4 ± 6.8 Ma (MSWD = 0.3) was obtained with the first approach, while a similar but slightly more precise age of 136.7 ± 4.7 Ma (MSWD = 1.95) was found with the second approach. For the other sample, ages of 127.0 ± 7.3 Ma (MSWD = 0.6) and 132.6 ± 4.5 Ma (MSWD = 1.5) were calculated with the first and second approaches, respectively. For $DC2_{Mano}$, the large dispersion of individual pixel isotopic ratio values should lead us to consider these ages with caution, despite the acceptable statistics. The ages correspond to 101.3 ± 12.6 Ma (MSWD = 1) (first approach) and 106.2 ± 8.1 Ma (MSWD = 1.1) (second approach). For $RD2_{Meillon}$, two samples gave reliable ages. For the first sample, taken directly from Meillon doloGST in the vicinity of major fault and dolomite breccias, two images were analyzed. Ages of 140.8 ± 9.2 Ma (MSWD = 0.4) and 136.6 ± 9.3 (MSWD = 0.5) were calculated with the first approach, whereas ages of 136.9 ± 4.8 Ma (MSWD = 1.1) and 134.0 ± 4.7 Ma (MSWD = 0.8) were obtained with the second. For the second sample, corresponding to a dolomite clast embedded in fault-related calcite cemented breccia, less precise ages of 113.8 ± 16.6 Ma (MSWD = 0.5) and 107.0 ± 5.6 Ma (MSWD = 1.3) were calculated depending on the approach used. Finally, for $DC4_{Meillon}$, ages of 112.7 ± 13.4 Ma (MSWD = 0.5) and 106.1 ± 5.5 Ma (MSWD = 1.6) were obtained for the first and second approaches, respectively.

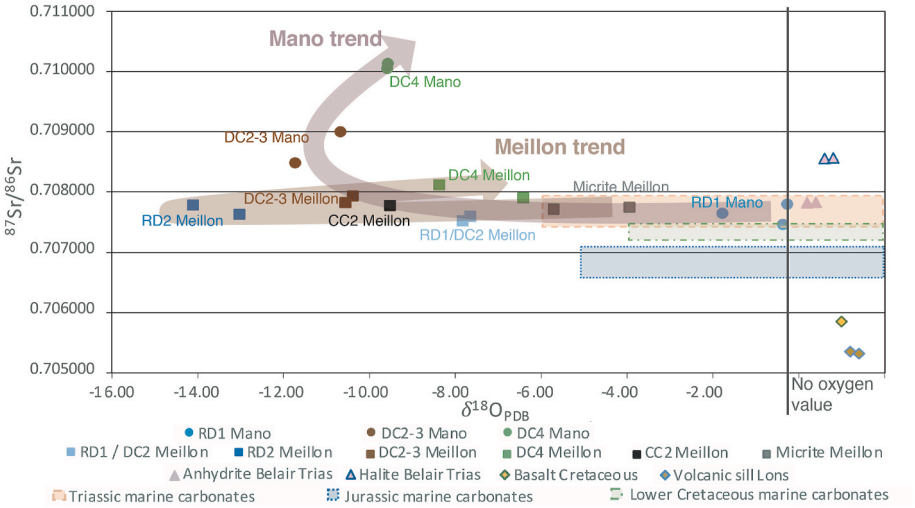


**Fig. 11.** $^{87}Sr/^{86}Sr$ vs $\delta^{18}O$ plot of the different cements and rocks. The arrows represent the chronological trend deduced from petrographical observations. The Jurassic and Triassic marine carbonate values are also indicated (McArthur et al., 2001).

### 4.3.5. Fluid inclusions

*4.3.5.1. Petrography of fluid inclusions.* The investigated dolomite cements in the breccias of the Meillon and Mano Formations have a high content of aqueous fluid inclusions (FIs). For RD1 and RD2 dolomites, the dark cloudy appearance of the crystals in both formations is due to the presence of numerous primary FIs of less than 2 μm in size.

In the DC2 dolomites of both formations, the dolomite crystals have a cloudy appearance due the presence of presumably primary FIs of less than 5 μm in size, which have a rectangular to oval shape (Fig. 13A). Most FIs are too small to distinguish their phase content (one or two phases). Only seven two-phase (water and gas) FIs could be analyzed.

In the DC3 dolomites of both formations, the FIs have a size of around 4–8 μm with an oval to elongated shape. Most are located along the crystal growth planes and are therefore primary (Fig. 13B). All the aqueous FIs have two phases (water and gas). The presence of very clear growth plans allowed us to precisely locate the FI positions in the crystal subdivision in order to link the measured temperatures to the oxygen isotope values specific to this area. Secondary fluid inclusion assemblages (FIAs) located on the planes intersecting the dolomite growth have been observed. Several FIAs stop at $DC4_{Mano}$ (Secondary A), while others intersect all the dolomite generations (Secondary B). These two-phased FIs postdate DC3 and were trapped before or during the DC4 precipitation.

In $DC4_{Mano}$ dolomites, only a few primary FIs are observed on crystal growth zones. These FIs have a rectangular to elongated shape with a size ranging from 2 to 10 μm (Fig. 13C). About half of these FIs are too small to be reliably described. The others have two phases (water and gas). In the Meillon Formation, several $DC4_{Meillon}$ crystals have a very high primary FI content. These have a rectangular shape ranging from 4 to 20 μm in size (Fig. 13D). Around 90% of these FIs have a size of less than 5 μm, and their content cannot be clearly assessed due to their small dimensions. The larger FIs all have two phases (water and gas).

In quartz, isolated FIs are interpreted as primary inclusions, whereas other FIs aligned along the healed fractures are interpreted as secondary. Both FIs have a two-phase aqueous content (water and gas).

In $CC1_{Meillon}$, no inclusions exceeding 2 μm could be observed. Finally, $CC2_{Meillon}$ contains a small amount of FIs. These are isolated, not aligned on the fracture planes, and interpreted as primary with two phases.

*4.3.5.2. Microthermometry.* The $T_h$ values obtained in the Mano cements are shown in Fig. 14A. $DC2_{Mano}$ yields $T_h$ values (n = 7) between 169 and 204 °C. The $T_h$ values of $DC3a\text{-}b_{Mano}$ range from 146 to 192 °C (mode = 157 °C; n = 21), whereas the $T_h$ values of $DC3c_{Mano}$ vary from 171 to 196 °C (mode = 196 °C; n = 20). The highest $T_h$ values observed in the Mano Formation are in $DC4_{Mano}$ FIs, ranging from 196 to 320 °C (n = 12). The large distribution of these values makes it difficult to determine a mode for $T_h$. Secondary FIs in $DC3_{Mano}$ have $T_h$ values around 200 °C (n = 19). Secondary FIs that do not cross $DC4_{Mano}$ have $T_h$ values around 265 °C (n = 4).

The $T_h$ values obtained in the Meillon cements are shown in Fig. 14B. In the Meillon Formation, $DC2_{Meillon}$ yields $T_h$ values between 230 and 232 °C (n = 4). The $T_h$ values of $DC3_{Meillon}$ range from 179 to 210 °C (mode = 207.5 °C; n = 18). Similar to the Mano Formation, the highest $T_h$ values measured in the Meillon Formation are in $DC4_{Meillon}$, the last dolomite cement. These $T_h$ values vary from 237 to 260 °C (mode = 260 °C; n = 6). Primary FIs of $Qtz_{Meillon}$ have $T_h$ values ranging from 135.5 to 205 °C (mode = 205 °C; n = 19), whereas the values of secondary FIs vary from 143.5 to 157.5 °C (mode = 148.5 °C; n = 12). The calcite cement $CC2_{Meillon}$ has $T_h$ values between 141.5 and 157.5 °C (n = 5).

*4.3.5.3. Raman analysis: chlorinity.* The chlorinity values obtained by Raman analysis are detailed in Fig. 14C. $DC2_{Mano}$ yields chlorinity values comprised between 0 and 3.6‰$_{eqNaCl}$ (mean = 1.6‰$_{eqNaCl}$; n = 3). For DC3, the values vary from 0 to 4.9‰$_{eqNaCl}$ (mean = 1.5‰$_{eqNaCl}$) in DC3a-b (n = 4) and from 0 to 12.4‰$_{eqNaCl}$ (mean = 4.9‰$_{eqNaCl}$) in DC3c (n = 11). The saddle dolomite $DC4_{Mano}$ has the highest chlorinity between 10.2 and 26.9% (mean = 19.7‰$_{eqNaCl}$; n = 4).

In the Meillon Formation, chlorinity was only measured in the $DC4_{Meillon}$ dolomite with values between 12.7 and 23.6‰$_{eqNaCl}$ (mean = 18.2‰$_{eqNaCl}$; n = 6). The primary and secondary FIs of quartz have a chlorinity ranging from 2.5 to 7.5‰$_{eqNaCl}$ (mean = 5.6‰$_{eqNaCl}$; n = 12) and 7.7 to 23.9‰$_{eqNaCl}$ (mean = 20‰$_{eqNaCl}$; n = 12), respectively. $CC2_{Meillon}$ (n = 2) has a chlorinity between 17.7 and 18.2‰$_{eqNaCl}$.

### 4.3.6. Rare earth elements

In the Mano Formation, the shale-normalized REE patterns of all the dolomite phases are similar, except for $DC4_{Mano}$ (Fig. 15A). The low REE (LREE) patterns are flat and thus consistent with the WSA, whereas the high REE (HREE) patterns tend to slightly decrease, being closer to the pattern of hydrothermal fluids. $DC4_{Mano}$ has a distinctive REE pattern, with a strong positive Eu anomaly and a greater decrease in HREE. This entire profile is more consistent with that of hydrothermal vents.

Except for $RD1_{Meillon}$, the REE patterns of the Meillon dolomites

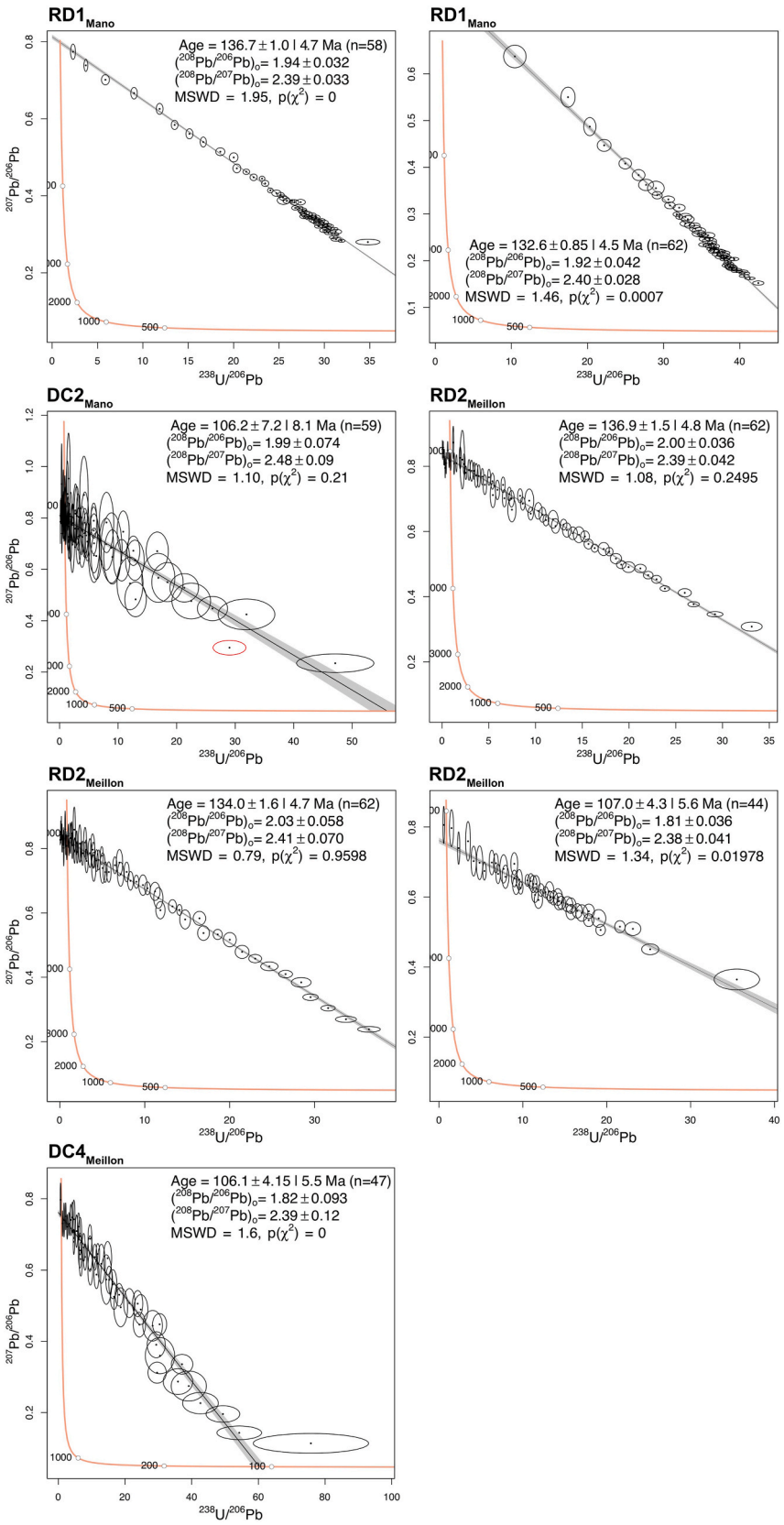


**Fig. 12.** Total-Pb/U–Th plots for the dolomites successfully dated by the U–Pb method of Drost et al. (2018). All ellipses correspond to two sigma uncertainties. For $DC2_{Mano}$, the red ellipse was not considered in the age calculation. (For interpretation of the references to color in this figure legend, the reader is referred to the Web version of this article.)

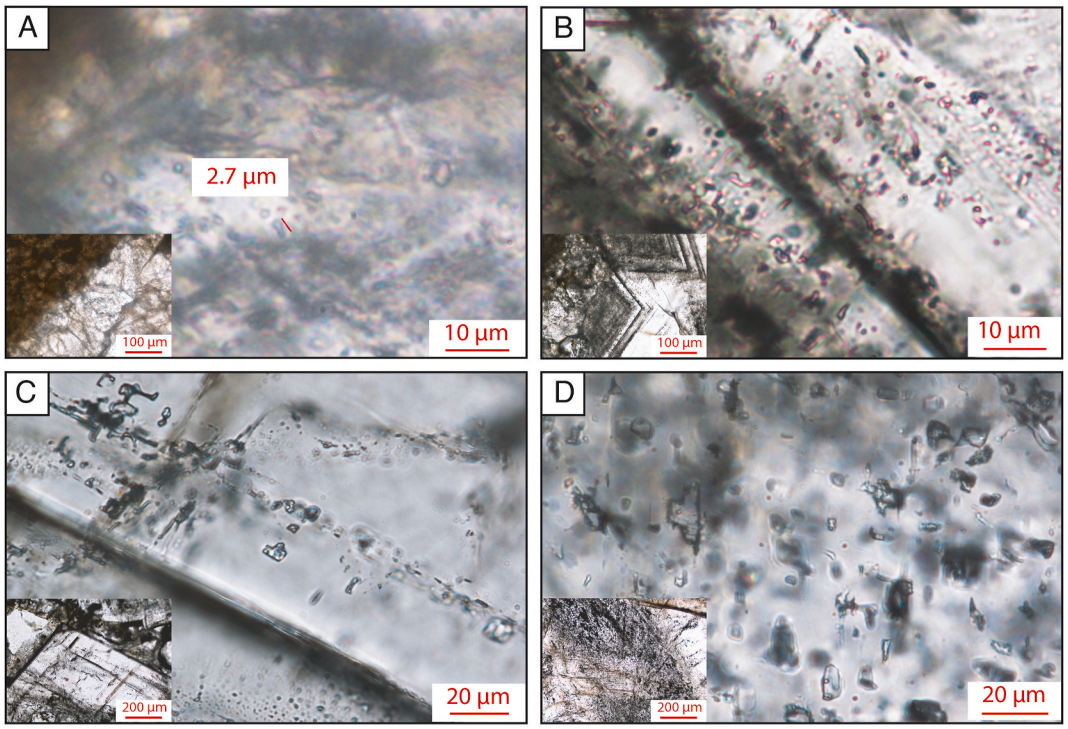


**Fig. 13.** Overview of the FIs present in the Mano and Meillon dolomite cements. A) Small oval FIs give a cloudy appearance to $DC2_{Mano}$; B) Primary FIs are located on the crystal growth plans of $DC3_{Mano}$; C) Rectangular FIs are found along a crystal growth zone in $DC4_{Mano}$; D) A high number of rectangular FIs occur in $DC4_{Meillon}$.

partly differ from those of the Mano dolomites (Fig. 15B). Their LREE patterns present a strong negative Ce anomaly, which is consistent with seawater. By contrast, their HREE patterns are similar to those of the Mano dolomites and thus more consistent with hydrothermal fluids. In addition, the $DC4_{Meillon}$ presents some distinction with a slightly positive Eu anomaly and a greater HREE decrease, closer to the profile of $DC4_{Mano}$.

## 5. Discussion

### 5.1. Paragenetic sequence

Our study on textural relationships, geochemical trends, FI microthermometry, and absolute age of the precipitation of diagenetic phases allows us to propose a complete paragenetic sequence of the Mano and Meillon Formations from the Early Cretaceous to the Cenozoic (Fig. 16).

The Mano and Meillon carbonate deposits were initially affected by early marine micritization as well as partial oolitic and peloidal grain dissolution. Thereafter, both formations were massively dolomitized during the Early Cretaceous, which is consistent with a near-surface to shallow burial context. In the Mano Formation, only one dolomitization event is recorded ($RD1_{Mano}$). In the Meillon Formation, remnants of a first dolomitization stage ($RD1_{Meillon}$) are locally preserved in the wackestone to packstone facies, whereas in the grainstone facies, the initial textures were completely overprinted by a second stage of massive dolomitization ($RD2_{Meillon}$). Widespread dolomitization probably occurred coevally to dolomite cementation (DC2 and DC3) in both the intercrystalline pores of the dolostones (including breccias) and the tectonic veins. A final stage of saddle dolomite cementation (DC4) occurred locally in the fault zones where it supports the breccias clasts. All dolomite cements, including the dolomite matrix ($RD1_{Mano}$ and $RD2_{Meillon}$), were either locally dissolved, thus creating solution-enhanced porosity, or directly replaced by calcite cement (CC1). In the residual porosity, subsequent quartz precipitated in the largest voids of several veins and breccias. The final cementation stage identified was only found in the Meillon Formation, with CC2 calcite blocking the residual porosity in large veins and filling new fractures. Finally, a last calcite cement with a rarely observed dripstone fabric ($CC3_{Meillon}$) filled the residual porosity of the Meillon Formation.

### 5.2. Near-surface to shallow burial: marine- or meteoric-derived water influx

#### 5.2.1. Early micritization and grain dissolution in near-surface conditions

All the dolomite cements of both formations present equivalent $\delta^{13}C$ values (range between +1 and + $4\%_{PDB}$). These values are in line with those of the marine carbonate deposits, pointing to a marine origin for the parent water or to $\delta^{13}C$ values influenced by the sedimentary marine carbonates originally forming the host rock (Longstaffe, 1987).

The oolitic and peloidal grains were micritized and partially dissolved in both formations, forming moldic porosity in the grainstone facies. Micritization occurred at or close to the surface soon after deposition, as commonly observed in marine platform carbonates (e.g., Scholle and Ulmer-Scholle, 2003). The preferential dissolution of aragonite or high-Mg calcite grains is also common, especially in platforms exposed to the ingress of meteoric water during emersion (Bathurst, 1971; James and Choquette, 1984).

#### 5.2.2. Widespread dolomitization in near-surface to shallow burial conditions

In the Mano Formation, an age of ~135 ± 5 Ma obtained for $RD1_{Mano}$ indicates that widespread dolomitization occurred between the Berriasian and the Hauterivian. Present-day sedimentary thickness suggests that the maximum burial of the Mano Formation did not exceed 500 m at that time (Castéras et al., 1970), assuming that compaction was limited due to the essential presence of high energy carbonate deposits in the Jurassic and pre-Albian units (dolostones and GST; Croizé et al., 2013; Goldhammer, 1997). We can use the maximum burial to propose an approximate precipitation temperature between ~20 °C at the surface to ~35 °C at 500 m, assuming a normal geothermal gradient of 30 °C/km (Fig. 17A). The parent water $\delta^{18}O$ ($\delta^{18}O_w$) of $RD1_{Mano}$ dolomite calculated for this temperature range, the measured dolomite $\delta^{18}O$ (−3 to

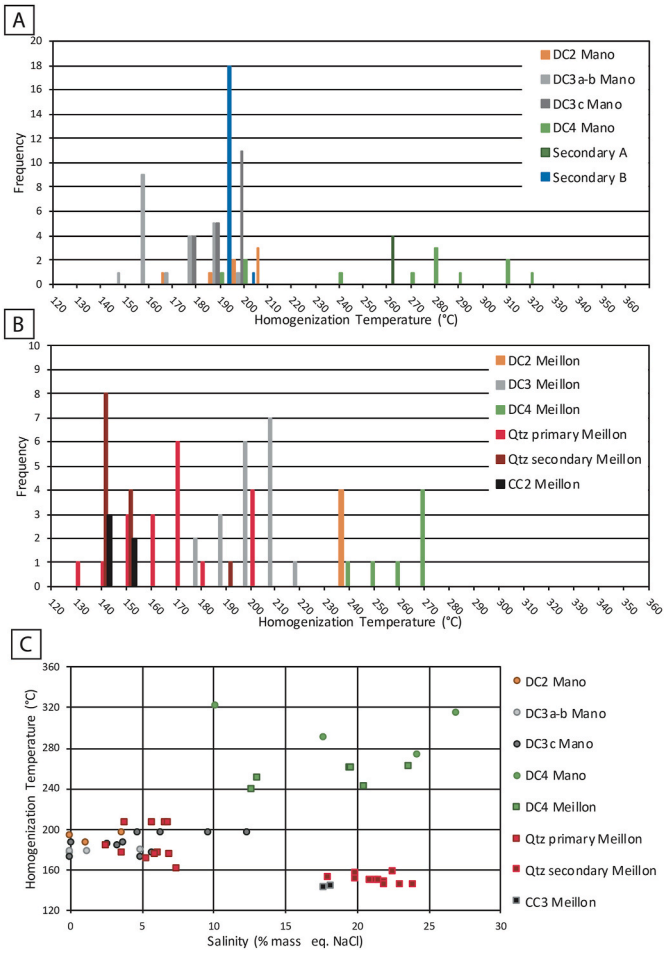


**Fig. 14.** Results of FI analysis. A) Histogram of homogenization temperatures of aqueous FIs measured in dolomite cements present in Breccia B in the Mano Formation; B) Histogram of homogenization temperatures of aqueous FIs measured in cements present in Breccia C in the Meillon Formation; C) Homogenization temperatures versus chlorinity measured by Raman spectroscopy in Mano and Meillon cements.

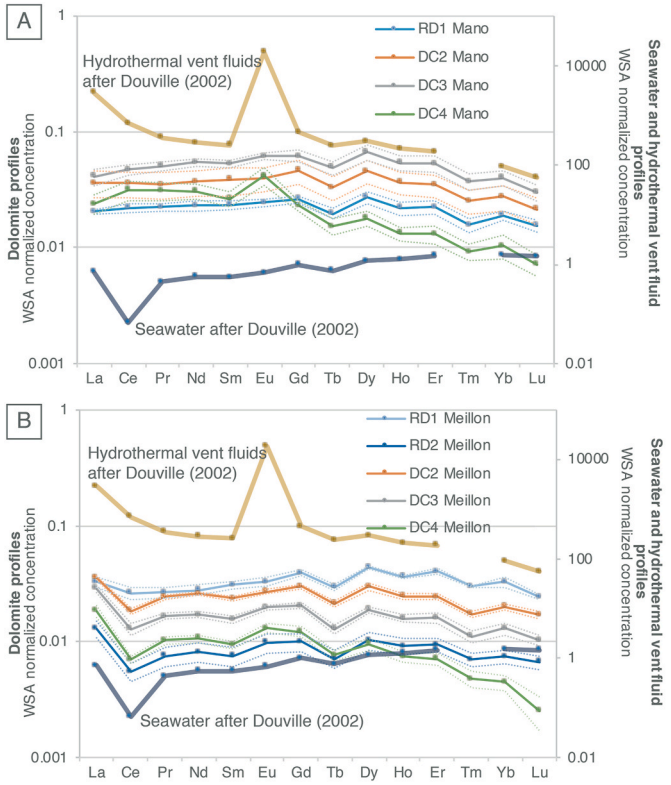


**Fig. 15.** REE profiles normalized to WSA in Mano (A) and Meillon (B) Formations with standard errors (1s) in dashed lines.

0.74‰$_{PDB}$), and the dolomite–water fractionation factor of Horita (2014) range from −5.9 to +1.2‰$_{SMOW}$ (Fig. 18). The lowest values are compatible with meteoric water, whereas slightly negative to positive values are more consistent with Early Cretaceous seawater to slightly evolved basinal waters (Longstaffe, 1987; Veizer and Prokoph, 2015). The Sr isotope values are higher than Early Cretaceous seawater (Fig. 11), suggesting an interaction with radiogenic components such as clays or bauxites deposited above the erosive truncation of the Mano Formation or the mixture of marine-derived water and groundwater (e.g., Adams et al., 2019; Nader et al., 2004; Railsback and Hood, 2001). The shale-like LREE pattern corroborates the interactions between radiogenic components, inducing a high water-rock interaction, whereas the HREE tends to slightly decrease and thus is in line with a hydrothermal fluid pattern. Although not fully diagnostic, dolomite and water $\delta^{18}O$ values, measured $^{87}Sr/^{86}Sr$ values, and LREE patterns are in line with $RD1_{Mano}$ dolomitization enhanced by the near-surface reflux of marine-derived water, which interacted with radiogenic components such as clay or mixed with groundwater (Fig. 17A). This mechanism of dolomitization is common in recently emerged carbonate platforms (Adam and Rhodes, 1960; Adams et al., 2019; Machel, 2004; Warren, 2000). This hypothesis is also consistent with previous studies on the Mano dolostones, which pointed to the presence of an early dolomitization phase linked to emersion and fed by seawater (Grimaldi, 1988). Although this interpretation is preferred, the hypothesis of higher temperature precipitation cannot be ruled out in the absence of more precise thermal constraints. In this case, the fluids causing dolomitization would have had higher $\delta^{18}O_w$ values, tending toward evaporative or basin signatures. Sr values higher than marine seawater could then be explained by the interaction with radiogenic components such as clay or crustal material (Longstaffe, 1987).

In the Meillon Formation, the U–Pb dating of the main replacive dolomite ($RD2_{Meillon}$) gives different ages in two distinct samples (~136 ± 5 Ma and 107 ± 5.6 Ma; Fig. 12). The first U–Pb age (Berriasian to Hauterivian), obtained from a dolomite clast embedded in calcite-cemented breccia, is similar within uncertainties to that of $RD1_{Mano}$ (Fig. 16). It is thus interpreted as reflecting the timing of the first dolomitization stage ($RD1_{Meillon}$), not reset during the subsequent recrystallization to $RD2_{Meillon}$. Taking this age, $RD1_{Meillon}$ would have formed in near-surface to shallow burial conditions (≤ 1000 m). Using its $\delta^{18}O$ values (−4.5 to −3.3‰$_{PDB}$) with a precipitation temperature between 20 °C at the surface and 50 °C at 1000 m ($\delta^{18}O$ ranging from −4.5 to −3.3‰$_{PDB}$), $\delta^{18}O_w$ values of −5 to +0.2‰ are calculated (Fig. 18). These values as well as the REE pattern are very similar to those obtained for $RD1_{Mano}$ dolomite, suggesting similar conditions of formation in near-surface to shallow burial conditions. These simultaneous massive dolomitizations imply a non-compartmentalized hydrologic system (Fig. 17A).

The second U–Pb age of $RD2_{Meillon}$ (Albian) was measured in a dolomite host rock located in the vicinity of a fault-related dolomite breccia. It is comparable within uncertainties to dolomite cement ages obtained in similar breccias in both formations ($DC2\text{-}3_{Mano}$ and $DC4_{Meillon}$; Fig. 16). It is thus interpreted as recording the timing of the recrystallization of $RD1_{Meillon}$ to $RD2_{Meillon}$, which was more pronounced at the vicinity of major faults. As detailed in the next section, such recrystallization occurred at a higher burial.

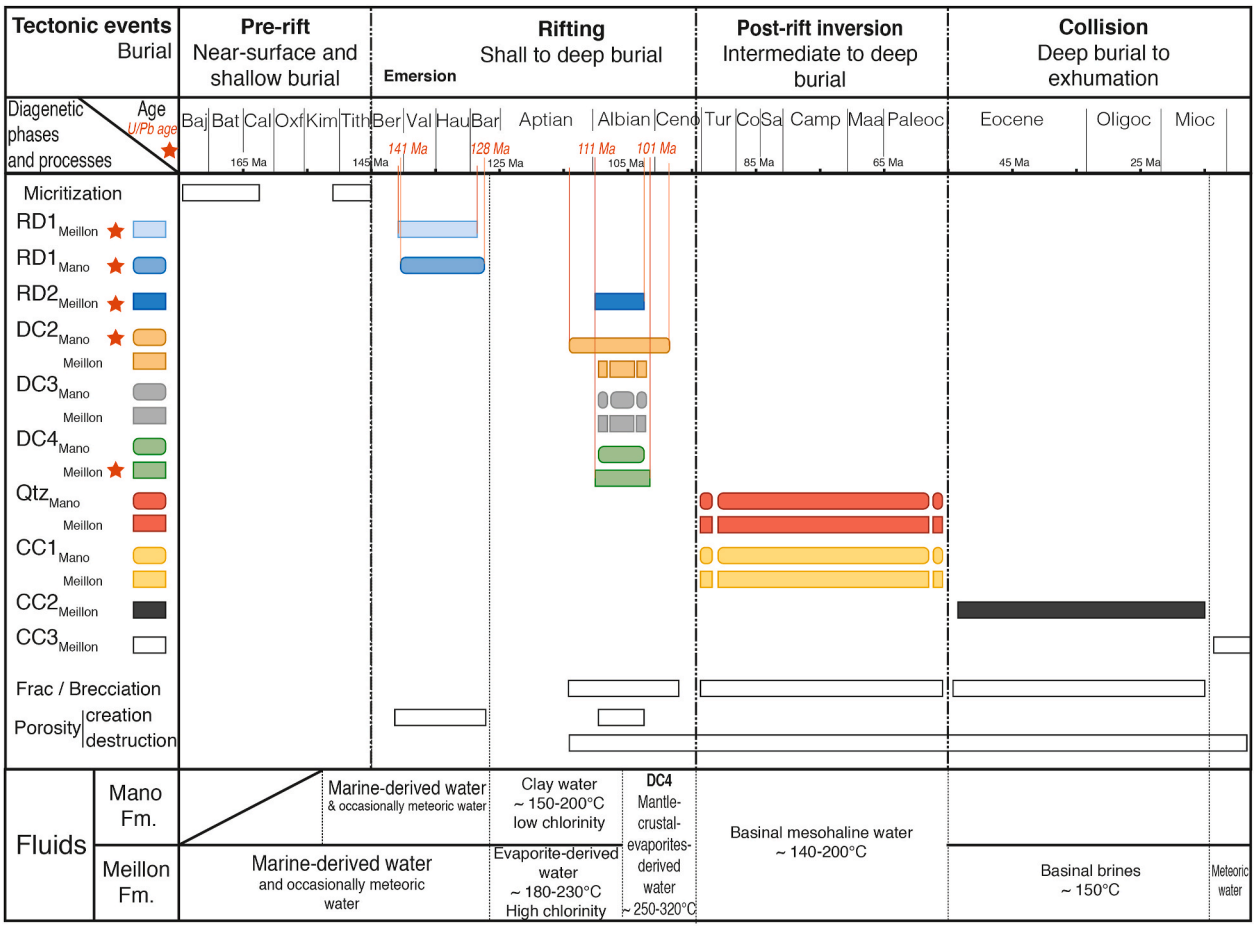


**Fig. 16.** Chronology of the diagenetic phases, including fluid data, observed in both the Mano and Meillon Formations set in time with U–Pb ages in the complex geodynamic evolution of the Mail Arrouy chaînon.

### 5.3. *Shallow to deep burial: toward the widespread influx of crustal fluids*

#### 5.3.1. *Massive recrystallization of dolomites in the Meillon Formation*

In the Meillon Formation, the U–Pb dating of the $RD2_{Meillon}$ points to a recrystallization during the Albian under a burial found at approximatively 1500–2000 m (Castéras et al., 1970, Fig. 16). The strongly negative $\delta^{18}O$ (mean = −13.4‰$_{PDB}$) makes the precipitation conditions clearly distinct from those of $RD1_{Mano}$ and $RD1_{Meillon}$. If the precipitation temperature was only controlled by burial (~1500–2000 m) under the high geothermal gradient expected during the Albian due to the rifting (~ 80 °C/km), $RD2_{Meillon}$ would have formed at a maximum temperature of ~180 °C (Corre, 2017; Hart et al., 2017; Vacherat et al., 2014). The corresponding $\delta^{18}O_w$ values of the $RD2_{Meillon}$ parent water (considering a $\delta^{18}O$ ranging from −14.5 to −12.6‰$_{PDB}$) would then range from +0.6 to +5‰$_{SMOW}$, pointing to the heavy basinal water interacting with the host rock (Longstaffe, 1987, Fig. 18). This would be consistent with the Sr isotope ratio measured in $RD2_{Meillon}$, similar to the Triassic marine carbonate values (Fig. 11). Hot water would have possibly interacted with the Triassic evaporites located only 500 m below and flowed up in the Meillon Formation (Castéras et al., 1970, Fig. 17B). The seawater-like REE pattern measured in $RD2_{Meillon}$ is in line with this interpretation, pointing to an interaction with marine water. In this case, these waters would not have reached the Mano Formation due to the presence of poorly permeable Lons Limestones, which were compacted at that time (Biteau et al., 2006). Thus, $RD2_{Meillon}$ dolomitization occurred as the hydrologic systems of the Mano and Meillon Formations were compartmentalized.

#### 5.3.2. *DC2 and DC3 cementations in compartmentalized reservoirs*

In the Mano Formation, the first two cements ($DC2_{Mano}$ and $DC3_{Mano}$) are ubiquitous. The U–Pb dating of $DC2_{Mano}$ constrains the timing of the precipitation to between ~114 and ~98 Ma, corresponding to the Aptian to Albian time interval (Fig. 16). FIs indicate cementation at temperatures of at least 160 °C, higher than those estimated in the host rock at this age (100–140 °C at 1000–1500 m). The dolomite cementations probably occurred under the hydrothermal regime, which is consistent with previous studies on dolomitization in the northwestern Pyrenees (Corre et al., 2018; Iriarte et al., 2012; Lopez-Horgue et al., 2010; Nader et al., 2012; Renard et al., 2018; Salardon et al., 2017).

These dolomites are characterized by a significant negative shift in the $\delta^{18}O$ values compared with the host rock and previous cements (Table 2). Considering FI temperatures (146–204 °C) and the oxygen isotope ratio measured in $DC2_{Mano}$ and $DC3_{Mano}$ (−14.7 to −9.4‰$_{PDB}$), the calculated $\delta^{18}O_w$ ranges from +1 to +10‰$_{SMOW}$ (mean = +5.9‰$_{SMOW}$; Fig. 19). Such positive values are consistent with heavy basinal water interacted with the host rock (Longstaffe, 1987). The high Sr isotope ratios measured in these cements are in line with this interpretation (Fig. 11). In addition, the low chlorinity measured in the FIs (Fig. 17B) points to an absence of interaction with the underlying Triassic evaporites. Low chlorinities are better explained by a meteoric water source or clay dehydration (Chaudhuri and Clauer, 1992; Longstaffe, 1987 and reference therein; Mountjoy et al., 1992; Wilkinson et al., 1992). The REE profiles of both $DC2_{Mano}$ and $DC3_{Mano}$ dolomite cements are very similar to that of $RD1_{Mano}$, which has a shale-like pattern. These REE patterns, in addition to the high $\delta^{18}O_w$ values, tend to favor clay dehydration as the main source of dolomite-saturated water. In this case, the Lons Formation, located just below the Mano

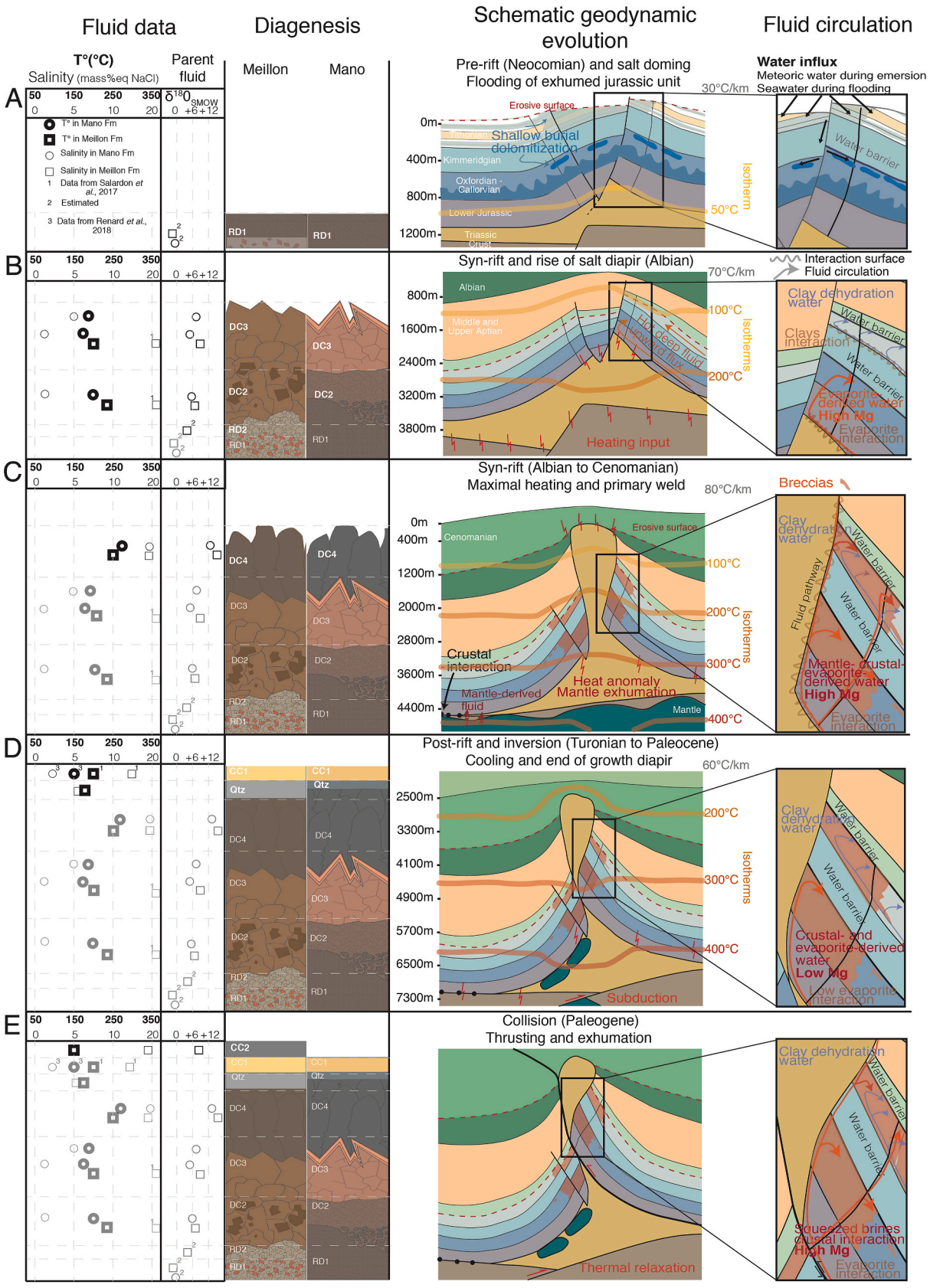


**Fig. 17.** General model of the evolution of fluid chemistry, fluid circulation, and diagenesis phases set in the schematic reconstruction of the Mail Arrouy chaînon and its structural and geochemical evolution. The rightmost sketches detail the inferred fluid circulations in the near-sampled area. The isotherms were developed based on Corre (2017), Hart et al. (2017), and Vacherat et al. (2014). The thermal anomalies around the salt structures were interpreted from Grunnaleite and Mosbron (2019), Jensen (1983), Kaiser et al. (2011), Mello et al. (1995), Peterson and Lerche (1995), and Selig and Wallick (1966).

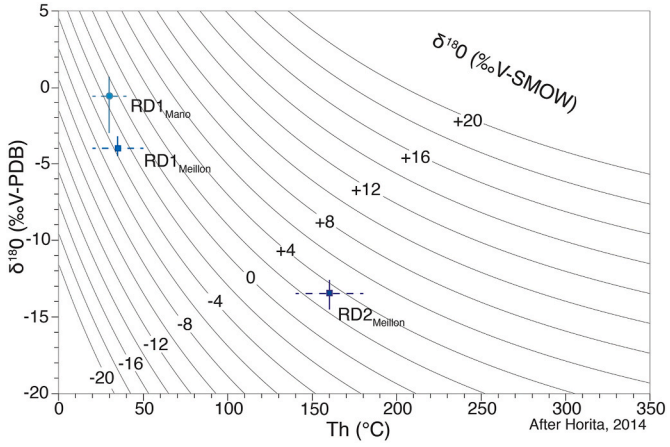


**Fig. 18.** Fractionation diagram for replacive dolomites using the dolomite–water fractionation factor of Horita, 2014). The values of the parent water $\delta^{18}O$ are calculated from an expected temperature range (dashed lines) and the measured dolomite $\delta^{18}O$.

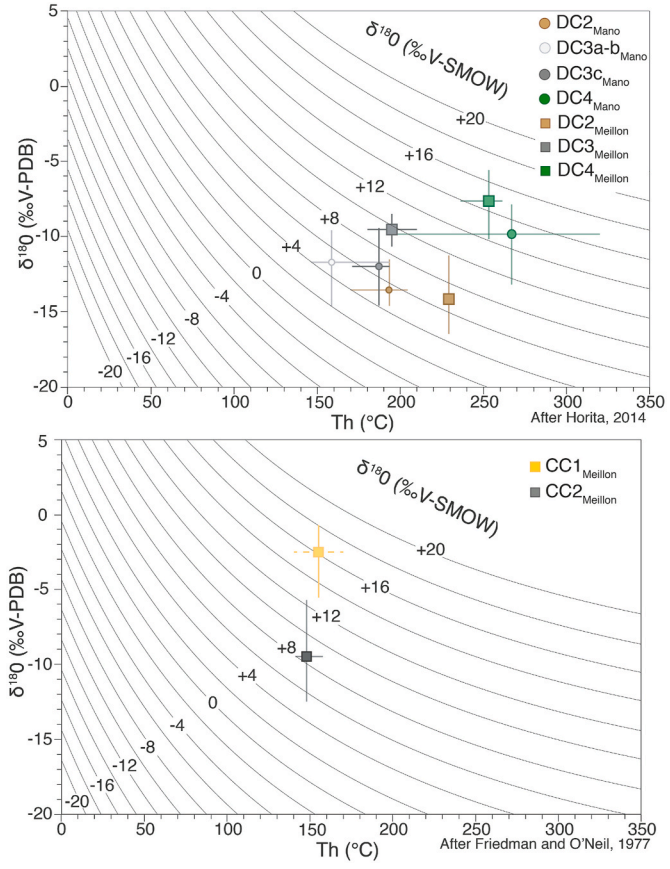


**Fig. 19.** Fractionation diagram for dolomite cements using the dolomite–water fractionation factor of Horita (2014) and calcite cements using the calcite–water fractionation factor of Friedman and O'Neil (1977). The dashed line for $CC1_{Meillon}$ values corresponds to the expected temperatures using the data of Salardon et al. (2017).

unit, could be a source of clay-related water. Clay dehydration could have provided some Mg in addition to the existing $RD1_{Mano}$ (e.g., Elias Bahnan et al., 2020; McHargue and Price, 1982; Mountjoy et al., 1992).

In the Meillon Formation, the U–Pb dating of the previous and later cements suggests a Barremian to Albian age development for $DC2_{Meillon}$ and $DC3_{Meillon}$ (Fig. 16; $RD2_{Meillon}$ and $DC4_{Meillon}$, with ages of ~136 Ma and ~106 Ma, respectively), which explains the high primary FI temperatures (180–230 °C). The similar $\delta^{18}O$ values between $RD2_{Meillon}$ and $DC2_{Meillon}$ suggests precipitation in close conditions. The calculated $\delta^{18}O_w$ of $DC2_{Meillon}$ ranges from +4.6 to +10.1‰$_{SMOW}$ (mean = +6.9‰$_{SMOW}$), whereas in $DC3_{Meillon}$, it ranges from +7.4 to +11.6‰$_{SMOW}$ with a higher mean value of +9.7‰$_{SMOW}$ (Fig. 19). This indicates a change to the heavier parent water $\delta^{18}O$ values over time at a constant temperature. The Sr isotopic ratio of the mixture of both cements lies in the range of the Triassic marine cement values (Fig. 11). Although the chlorinity of the parent fluid could not be measured, it can be expected to be high based on the study of Salardon et al. (2017), who found water with high chlorinity in similar dolomite cements of the Meillon Formation. The REE profiles measured in these cements are similar to that obtained in $RD2_{Meillon}$ with a seawater pattern. However, our data and those of Salardon et al. (2017) strongly suggest that $DC2_{Meillon}$ and $DC3_{Meillon}$ cements precipitated from isotopically heavy evaporite-derived water with high chlorinity. This interpretation differs from that of Salardon et al. (2017), who suggested a magmatic water source. This highlights once again a clear compartmentalization between the Mano and Meillon reservoirs (Fig. 17B). For $RD2_{Meillon}$, $DC2_{Meillon}$, and $DC3_{Meillon}$, it is likely that the Mg was provided in part locally by $RD1_{Meillon}$ (e.g., Gao et al., 1995; Gisquet et al., 2013; Guo et al., 2016; Montanez, 1994; Zhang et al., 2009). However, the external brines with a Triassic signature could have supplied part of the Mg necessary for precipitation, which would not be surprising in a context of salt tectonics (Davies and Smith Jr, 2006; Krupp, 2005; Quesnel et al., 2019; Wendte et al., 1998).

### *5.3.3. Saddle dolomite DC4: last dolomite cementation in the connected reservoirs*

This last dolomite cement could only be dated to the Meillon Formation ($DC4_{Meillon}$), where it also formed during the Albian (Fig. 16). In both formations, saddle dolomites are characterized by higher precipitation temperatures (>250 °C) and oxygen isotope ratios compared to previous cements (Table 2). In the Mano Formation, the corresponding parent water oxygen isotope ratios range from +6.1 to +16.8‰$_{SMOW}$ (mean = +12.8‰$_{SMOW}$), whereas in the Meillon Formation, they range from +11.4 to +17.1‰$_{SMOW}$ (mean = +14.5‰$_{SMOW}$; Fig. 19). In both formations, the chlorinity measured in the FIs reaches 20%$_{eqNaCl}$. Although this corresponds to a very strong increase in the Mano Formation, it is more in line with the values measured in previous cements in the Meillon Formation, as evidenced by Salardon et al. (2017) (Fig. 17C). These high chlorinities as well as the high $\delta^{18}O_w$ suggest the influence of Triassic evaporites, added to the significant increase in the water-to-rock ratio (Land and Prezbindowski, 1981; Longstaffe, 1987). Given the absence of clastic rocks in the Mano Formation and the Triassic evaporites, the very high Sr isotope ratios measured in $DC4_{Mano}$ (>0.71; Fig. 11) necessarily imply contributions from the Paleozoic basement (Banner, 1995; Chaudhuri and Clauer, 1992). The low Sr ratios of the volcanic rocks exclude any interactions with magmatic-related fluids (Fig. 11). Moreover, the REE profiles of both DC4 dolomite cements differ from those measured in other dolomites. They present a positive Eu anomaly (very strong for $DC4_{Mano}$ and less pronounced for $DC4_{Meillon}$) and a decrease in the HREE content compared to LREE (Fig. 15). These characteristics mimic those of the fluids hosted by ultramafic rocks like peridotites (e.g., Douville et al., 2002, 1999; Tostevin et al., 2016). It is thus likely that dolomitizing waters also interacted with the mantle located below the thinned continental crust or even exhumed. Mantle serpentinization reactions are known to release large amounts of Mg, which may have contributed to dolomite precipitation (Breesch et al., 2010; Chen et al., 2016; Debure et al., 2019; Koeshidayatullah et al., 2020; Pinto et al., 2017; Salardon et al., 2017). Finally, DC4 precipitated from water resulting from a mixture of evaporite-, crustal-, and mantle-derived waters, each of which was able to provide part of the Mg necessary for precipitation to occur. A simple scenario would be that mantle-derived fluids migrated

upward through the residual crust and Triassic evaporites. These saddle dolomites are located near faults, indicating that these fluids were channeled by the fault network, which acted as pathways between the Mano and Meillon reservoirs (Fig. 17C). This interpretation is consistent with several studies on dolomitized carbonate platforms, which highlight similar diagenetic evolutions, especially the role of faults on high temperature dolomitization (Barale et al., 2016; Duggan et al., 2001; Haeri-Ardakani et al., 2013a, 2013b; Lopez-Horgue et al., 2010; Mozafari et al., 2019).

### 5.4. Deep burial to exhumation: from dolomite-to quartz- and calcite-saturated waters

#### 5.4.1. Quartz precipitation: influx of diluted waters in the Meillon Formation

Following the dolomite cementation, both the Mano and Meillon Formations were affected by local dedolomitization. This marks a change in the composition of the waters and/or of pression-temperature conditions, leading to dolomite undersaturation (e.g., Brauer and Baker, 1984). According to the U–Pb dating of DC4 cement, the dolomite dissolution or replacement occurred after ~100 Ma, corresponding to the post-rift phase and/or Pyrenean shortening (Puigdefàbregas and Souquet, 1986). This evolution of the water composition is also recorded during the subsequent precipitation of quartz, which partially blocked the residual intercrystalline porosity (Table 2). FIs measured in quartz from the Meillon Formation record a significant decrease in chlorinity and lower temperatures compared with DC4, which is compatible with precipitation during shortening (Vacherat et al, 2014, 2016). These lower values may explain the transition from carbonate to silica-saturated waters due to the retrograde solubility of dolomite. The low chlorinity also shows a decreasing interaction with Triassic evaporites, clearly indicating a change in the water migration pathways. This would be better explained by the influx of meteoric waters or by clay dehydration. The latter is preferred given (1) the still high temperatures recorded by primary FIs (~170 °C), which is compatible with significant burial at the time of quartz precipitation, and (2) the nearby presence of clay-rich formations (Lons Limestones and overlying flysch deposits). Silica necessary for quartz precipitation was provided by these formations (e.g., Hesse, 1987) or interaction with the basement (e.g., Bustillo, 2010), but neither of these hypotheses can be excluded based on the available data.

#### 5.4.2. Calcite cementation: second stage of reservoir compartmentalization

The paragenetic relationships between quartz and calcite cements CC1 to CC3 could not be firmly established. However, based on the presence of calcite-cemented dissolution vugs in quartz, Salardon et al. (2017) proposed that quartz precipitated before calcite in the study area. This would constrain calcite to have likely precipitated during the Pyrenean shortening.

The first calcite cement CC1 is characterized by $\delta^{18}O$ values of around −2.6‰, the highest value of all the calcite cements. The absence of FI data prevents the characterization of the parent water composition. However, considering the $T_h$ of ~170 °C measured in quartz and the $T_h$ of ~140 °C measured in CC2, it is likely that the precipitation temperature of CC1 is in the range of 140–170 °C. Using these temperatures and the calcite-water oxygen isotope fractionation factor of Friedman and O'Neil (1977), this gives an isotopic value in the range of +11.5 to +17.2‰$_{SMOW}$ (Fig. 19), pointing to a very high water-to-rock ratio. In the Mano Formation, the study of Renard et al. (2018) shows that the first calcite cementation after dolomitization took place at ~150 °C with very low chlorinity water (range between 1.2 and 4.4%$_{eqNaCl}$). In the Meillon Formation, according to Salardon et al. (2017), the calcites formed at ~200 °C with high chlorinity water (range between 13 and 16%$_{eqNaCl}$). Such contrasting chlorinities imply that the Mano and Meillon Formations were once again compartmentalized during the calcite precipitation. Whereas the low chlorinities in the Mano Formation may indicate dilution with clay-dehydration water, the high chlorinities and temperatures in the Meillon Formation point again to the influx of water interacting with the Triassic evaporites in contrast with the previous quartz cements (Fig. 17D).

The CC2 calcite cement, which is only observed in the Meillon Formation, is mainly associated with breccias located near the fault zones, suggesting fluid circulation during fault activity (Heydari, 1997; Oliver, 1986, Fig. 17E). The CC2 cement was formed from high chlorinity water, similar to $CC1_{Meillon}$ but at a lower temperature (<150 °C), which is consistent with the decreasing depth during exhumation (Table 2). The calculated $\delta^{18}O$ of the parent water ranges from +4.5 to +9.8‰$_{SMOW}$ (Fig. 19). This parent water has the same characteristics as that described for the cement CC2 of Salardon et al. (2017). These authors suggested that given the negative $\delta^{13}C$ values, the parent water of this cement was of meteoric origin. Assuming that their CC2 cement is the same as our CC2 calcite, this interpretation is not consistent with the calculated $\delta^{18}O_w$ or their very high chlorinity, which is more typical of the heavy basinal water and still points to interactions with evaporites at a depth.

The last CC3 calcite cement was observed in the intercrystalline porosity of the Meillon Formation. This cement has a dripstone fabric (microstalactitic cement), which is consistent with a vadose environment (Moore and Wade, 2013). The CC3 cement probably marks the final exhumation of the area with the influx of meteoric water (e.g., Martín-Martín et al., 2015).

### 5.5. Local controls on dolomitization

#### 5.5.1. Limited role of the carbonate facies

The carbonate matrix of the Mano and Meillon Formations has been largely affected by dolomitization, occurring as replacive dolomite ($RD1_{Mano}$, $RD1_{Meillon}$, and $RD2_{Meillon}$) or porosity-infilling cement (DC2 and DC3). In the Mano Formation made of MST and WST facies, early dolomitization by $RD1_{Mano}$ was ubiquitous. On the contrary, in the Meillon Formation, early dolomitization ($RD1_{Meillon}$) was more pronounced in the oolitic and peloidal grainstones compared to mudstone and packstone facies, with the latter showing isolated rhombs. Thus, despite relatively similar conditions of deposition, the two formations considered here show the contrasting impact of carbonate facies on early dolomitization. The same applies to late dolomites ($RD2_{Meillon}$, DC2, and DC3). Whereas $RD1_{Mano}$ was largely preserved in the Mano Formation, with only small volumes of $DC2_{Mano}$ and $DC3_{Mano}$ cements in veins and residual porosity, $RD1_{Meillon}$ was almost entirely overprinted in the Meillon Formation by $RD2_{Meillon}$ (and locally affected by $DC2_{Mano}$ and $DC3_{Mano}$). This difference can be simply explained by the presence of the Lons Formation above the Meillon Formation, as the former acted as a seal, thus limiting the upward flow of deep hot waters. Therefore, as will be discussed below, the role of the stratigraphic architecture seems to have been primordial compared to that of the carbonate facies.

#### 5.5.2. Late dolomitization: interplays between faults and sedimentary breccias

In contrast to the previous cements, saddle dolomite DC4 only precipitated in association with breccias that presented a fracture geometry in the vicinity of faults (Fig. 3). The similarities of the parent fluids in the DC4 of the Mano and Meillon Formations suggest that these faults acted as a conduit channelizing the fluids in both units. Similar fault-controlled dolomitization has been suggested in several studies conducted in proximity (Iriarte et al., 2012; Lopez-Horgue et al., 2010; Nader et al., 2012; Salardon et al., 2017; Shah et al., 2010) and in other carbonate platforms worldwide (Barbier et al, 2012, 2015; Duggan et al., 2001; Haeri-Ardakani et al., 2013a; Hendry et al., 2015; Koeshidayatullah et al., 2020; Martín-Martín et al., 2015; Mountjoy and Halim-Dihardja, 1991; Mozafari et al., 2019; Rustichelli et al., 2017; Stoakes, 1987; Wendte et al., 2009; Zhang et al., 2009).

However, a peculiarity of the late dolomitization in the Mail Arrouy

relates to the presence of bedding parallel breccias extending from the fault zones over several hundred meters (Fig. 17). These mosaic breccias (Breccia B) pass laterally to karst-related sedimentary-collapse breccias (Breccia A). The dolomite mud that supports the fragments of sedimentary breccias was replaced by saddle dolomites with a rough irregular front, creating a mosaic breccia-like morphology with dolomite white cement (Fig. 3). Here, it is thus clear that the mosaic breccias (Breccia B) result from a process of neomorphism rather than the more commonly proposed process of hydraulic fracturing despite the textural similarities. If neomorphism has been largely studied, for example, in experiments of mineral replacement (Pedrosa et al., 2016; Putnis, 2002, 2009), to our knowledge, this is the first time that "neomorphic dolomite breccia" has been described from field observations. Nevertheless, regardless of the brecciation mechanism, saddle dolomitization is firstly fault-controlled and then locally with a stratabound geometry considering the horizontal distribution of karstification and sedimentary breccias.

### 5.6. Impact of the geodynamic context on the diagenetic record

#### 5.6.1. Pre-rifting and salt tectonics

The first RD1 dolomitizations were associated with shallow burial to emersion, enabled by the inflow of seawater during the Late Jurassic and Early Cretaceous emersion. Massive seawater dolomitization directly resulted from the combined effect of a regional uplift and the initiation of salt doming in the *Chaînons Béarnais* linked to the early stage of rifting (Canérot et al., 2005; Canérot and Lenoble, 1993; Izquierdo-Llavall et al., 2020; James and Canérot, 1999; Labaume and Teixell, 2020). The seawater influx was likely favored by rift-related faulting both in the basement and at the crest of the anticlines formed above the salt domes (e.g., Fischer et al., 2013; Moragas et al., 2020).

#### 5.6.2. Syn-rift and diapirism

In the Meillon Formation, the massive $RD2_{Meillon}$ dolomitization, dated to 107 ± 5.6 Ma as well as the dolomite cements $DC2_{Meillon}$ and $DC3_{Meillon}$, filling pores, fractures, and breccias exhibit post-Neocomian to Albian ages, resulting from the circulation of Triassic evaporite-derived water (Fig. 17B). The inflow of these fluids occurred during the syn-rift period, characterized by a gradual increase in the geothermal gradient due to the crustal thinning, beginning with mantle exhumation, volcanic activity, and in the cover layer, the rise of salt diapirs and ridges in response to the faulting of the sedimentary cover (Brinkmann and Lögters, 1968; Canérot et al., 2005; Clerc et al., 2015; Corre et al., 2016; Golberg and Leyreloup, 1990; Izquierdo-Llavall et al., 2020; Jammes et al., 2010a; Labaume and Teixell, 2020; Lagabrielle et al., 2010). The upflow of hot water could have been favored by the rise of the salt diapir due to the enhanced focused fluid flow along the impervious diapir boundaries and the enclosing rocks as well as the accumulation of heat at the top of the structure that generates thermal convection (Fig. 17B; Grunnaleite and Mosbron, 2019; e.g., Jackson and Hudec, 2017 and references therein; Jensen, 1983; Kaiser et al., 2011; Mello et al., 1995; Selig and Wallick, 1966).

In the Mano Formation, the lack of recrystallization related to the circulation of Triassic evaporite-derived water is due to stratigraphic compartmentalization. Only dolomite cements ($DC2_{Mano}$ and $DC3_{Mano}$) precipitated in the entire Mano Formation during the syn-rift due to the circulation of clay-derived water under the hydrothermal regime. Although the upflow of hot water was probably favored by the rise of salt diapir as in the Meillon Formation, it was limited to the compartmentalized Mano Formation (Fig. 17B).

The last dolomite DC4, also precipitated during the Albian, records the highest temperatures observed in the diagenetic cements, which is consistent with the high temperatures measured in the host rock (Corre, 2017; Izquierdo-Llavall et al., 2020). This period also corresponds to the maximum growth of salt diapirs and associated halokinetic folds (Canérot et al., 2005). Following the rise of the Mail Arrouy salt wall, its progressive welding (Labaume and Teixell, 2020) may have created fluid pathways at the contact between the salt and the enclosing rocks by means of faulting and fracturing, connecting both formations to the hot water initially present only in the lower compartment (Meillon; Fig. 17C). Crustal interaction recorded by the saddle dolomite implies that the seal formed by the Triassic salt was breached by welding, salt flow, or salt dissolution, thus allowing the ascent of basement-derived waters (Jackson and Hudec, 2017; Fig. 17C).

Therefore, tectonics exerted strong control on the fluid circulation and associated dolomitization by creating pathways through faults and fracture networks as well as along the diapir boundaries. This consequently had an important effect on the diagenetic evolution of the carbonate platform in accordance with other studies conducted in similar tectonic settings (Callot et al., 2010; Gonzalez et al., 2012; Roure et al, 2005, 2010; Vilasi et al., 2009).

#### 5.6.3. Post-rift and pyrenean compression

Dolomite cements are followed by the precipitation of quartz, which likely occurred during the post-rift stage (Fig. 16). At that time, the burial temperature gradually decreases but remained high due to a blanketing effect (Vacherat et al., 2014). More locally, FIs demonstrate that the parent water became more diluted, which, combined with the temperature decrease, probably favored the transition from a dolomite-to quartz-saturated composition. The lower contribution of salt to the water composition could be explained by the continued salt evacuation related to the ongoing diapirism during the post-rift phase (Fig. 17D).

The last identified cements are calcites, which filled fractures and breccias. The precipitation temperatures recorded by the FIs are the lowest of all cements ($T < 150$ °C), testifying to the exhumation of the area during the Pyrenean shortening. However, chlorinity increases significantly compared to quartz, suggesting a renewed interaction with evaporites. During the Pyrenean compression, salt tectonic structures resumed through squeezing, while some of them were thrusted (Canérot et al., 2005; Izquierdo-Llavall et al., 2020). The reactivation of these existing structures may have generated the pumping and expulsion of basinal brines at the origin of the calcite cementation (Fig. 17E). The presence of squeegee-type flow is consistent with the observation of Salardon et al. (2017) and several other studies on fold and thrust belts (Al-Aasm et al., 2019; Beaudoin et al., 2014; Machel and Cavell, 1999; Oliver, 1986; Roure et al., 2010).

### 5.7. Implications for exploration

More than 90% of the dolomite identified in the Mano and Meillon Formations concern $RD1_{Mano}$ and $RD2_{Meillon}$, which formed from fluids with distinct geochemical characteristics and at different ages, likely due to the presence of Lons Limestones between both formations. Replacive dolomitization was thus controlled at a large scale by the sedimentary architecture of the carbonate platform, resulting in the development of two largely unconnected dolomite reservoirs. Except for the last episode of dolomite cementation DC4, compartmentalization was effective during all the subsequent records of cement precipitation, from the syn-rift to the inversion stages. Influencing the reservoir diagenesis, compartmentalization effects should also be considered in hydrocarbon migration.

Whereas dolomitization in the Mano Formation can be explained by the seepage of marine-derived water, the influx of deep hot water is required in the Meillon Formation. These fluids most likely originated from the large layer of pre-rift salt located below the carbonate platform. Significant heat caused by the thinning of the passive margin during the syn-rift stage may have triggered an upward fluid flow by thermal convection. The combination of a thick salt layer and an abnormal heat flux resulted in the complete dolomitization of a reservoir unit associated with gas generation and storage in the Aquitaine Basin (Biteau et al., 2006). This also led to the development of drains with dyke-like

brecciated conduits as well as saddle dolomite geobodies. Thus, hyper-extended passive margins might be important targets in the exploration of reservoirs, provided that thick salt layers were deposited. The combined presence of a carbonate platform in this hot context close to the evaporites could have generated large volumes of dolomites, thus releasing essential porosity for the storage of georesources, even if reservoirs in this context can also be affected by dolomite cementation by blocking previously created porosity. This case study clearly demonstrates the usefulness of applying multidisciplinary and integrated workflows to better understand the evolution of complex diagenetic systems such as salt-rich hyper-thinned passive margins.

## 6. Conclusion

The diagenetic evolution of the dolomitized Jurassic carbonate platform of the northwestern Pyrenees, which comprises two major oil and gas reservoir analogues (Mano and Meillon Formations), was studied here in detail from the outcrops of the *Chaînons Béarnais*. The main features of their diagenetic history, especially the conditions of dolomitization, may be summarized as follows:

1. Massive limestone dolomitization, which comprises the main volume of dolomite in the area, was generated in near-surface to shallow burial conditions in both carbonate reservoirs. This was primarily controlled by the carbonate facies, and thus, by the depositional environments and vertical stacking.
2. This dolomitization occurred coevally in the Mano and Meillon Formations at about ~135 Ma, beginning with the seepage of marine-derived water that interacted with clay and/or groundwater in normal thermal conditions, thus allowing for the regional uplift and the early reactive salt diapirism.
3. The influx of hot basinal brines by thermal convection interacted with underlying Triassic evaporites and remobilized early dolomites, resulting in a massive dolomite recrystallization of the Meillon Formation at around ~106 Ma. This dolomitization was triggered by crustal thinning and the associated thermal anomaly generated during the Early Cretaceous rifting. It was probably enhanced by the rise of salt diapir. This dolomitization highlighted the compartmentalization of the two reservoirs.
4. Two additional dolomite cementation stages are recorded in the residual porosity and tectonic veins of the still compartmentalized formations. Precipitation occurred at temperatures above ~150 °C during the Albian. Whereas the cements in the Meillon Formation still record the contribution from dissolved Triassic evaporites, in the Mano Formation, they precipitated from low salinity water, probably resulting from clay dehydration. In this case, Mg was probably supplied mostly by the earlier massive dolomites.
5. At the same time during the Albian, a last saddle dolomite cement precipitated in the vicinity of faults associated with breccias. It formed from the same highly saline, hot ($T > 250$ °C), crustal-derived waters possibly mixed with mantle-derived fluids in both formations. The connection between the reservoirs was then restored as a result of the faulting and active diapirism related to Early Cretaceous rifting. In the Mano Formation, these basinal brines locally seeped into sedimentary breccias, generating the stratabound replacement of the dolomite.
6. Subsequent quartz and calcite cements, formed at a lower temperature ($T < 200$ °C), record the restauration of the reservoir compartmentalization in a post-rift to inversion context.

This case study represents a comprehensive and data-rich example of the multi-phase dolomitization of a carbonate platform in a complex geodynamic setting evolving from pre-rift to hyperextension and then collision. This provides evidence of the major control exerted by rifting, combined with the presence of diapiric salt, on dolomitization. Likewise, ancient carbonate platforms on modern salt-rich passive margins may have been massively dolomitized, thus forming potential targets for exploration.

## Declaration of competing interest

The authors declare that they have no known competing financial interests or personal relationships that could have appeared to influence the work reported in this paper.

## Acknowledgments

Geoffrey Motte benefited from a PhD grant funded by Total EP-R&D as part of the Fluids geological research project. Laurent Guy is kindly thanked for his support and introduction to the field. Laurent Lambert and his colleagues from BGM *Center Scientifique et Technique Jean Féger TOTAL* are thanked for providing access to their facilities. Guillaume Barré and Stephen Centrella are warmly thanked for their fruitful discussions. The authors also acknowledge the suggestions and comments of the associate editor Marco Brandano and the reviewers Juan Diego Martín Martín and Mar Moragas, which greatly improved the quality of the manuscript.

## Appendix A. Supplementary data

Supplementary data to this article can be found online at https://doi.org/10.1016/j.marpetgeo.2021.104932.

## Credit author statement

**Geoffrey Motte**: Field, petrographical and geochemical data acquisition, analysis and design; paper writing. **Guilhem Hoareau**: Supervision; dating, geochemical and diagenesis analysis. **Jean-Paul Callot**: Supervision, structural geology, integration. **Sylvain Calassou and Eric Gaucher**: Regional integration and revisions. **Sidonie Révillon**: Sr isotopes analysis and data extraction. **Francesca Piccoli**: Rare earth element analysis and data extraction.

## References

Adam, J.E., Rhodes, M.L., 1960. Dolomitization by seepage refluxion. Am. Assoc. Petrol. Geol. Bull. 44, 1912–1920. https://doi.org/10.1306/bc74368d-16be-11d7-8645000102c1865d.

Adams, A., Diamond, L.W., Aschwanden, L., 2019. Dolomitization by hypersaline reflux into dense groundwaters as revealed by vertical trends in strontium and oxygen isotopes: upper Muschelkalk, Switzerland. Sedimentology 66, 362–390. https://doi.org/10.1111/sed.12530.

Al-Aasm, I.S., Mrad, C., Packard, J., 2019. Fluid compartmentalization of devonian and mississippian dolostones, western Canada sedimentary basin: petrologic and geochemical evidence from fracture mineralization. Can. J. Earth Sci. 56, 265–305. https://doi.org/10.1139/cjes-2018-0226.

Albarède, F., Michard-Vitrac, A., 1978. Datation du métamorphisme des terrains secondaires des Pyrénées par la méthodes 39Ar-40Ar et 87Rb-87Sr. Ses relations avec les péridotites associées. Bull. Société Géologique Fr. 20, 681–687.

Azambre, B., Rossy, M., 1976. Le magmatisme alcalin d'âge crétacé dans les Pyrénées occidentales et l'Arc Basque ; ses relations avec le métamorphisme et la tectonique. Bull. Société Géologique Fr. 18, 1725–1728.

Azambre, B., Rossy, M., Albarède, F., 1992. Petrology of the alkaline magmatism from the cretaceous north-pyrenean rift-zone (France and Spain). Eur. J. Mineral 4, 813–834.

Banner, J.L., 1995. Application of the trace element and isotope geochemistry of strontium to studies of carbonate diagenesis. Sedimentology 42 (5), 805–824. https://doi.org/10.1111/j.1365-3091.1995.tb00410.x.

Barale, L., Bertok, C., Talabani, N.S., D'Atri, A., Martire, L., Piana, F., Préat, A., 2016. Very hot, very shallow hydrothermal dolomitization: an example from the Maritime Alps (North-West Italy – South-East France). Sedimentology 63, 2037–2065. https://doi.org/10.1111/sed.12294.

Barbier, M., Floquet, M., Hamon, Y., Callot, J.-P., 2015. Nature and distribution of diagenetic phases and petrophysical properties of carbonates: the Mississippian Madison Formation (Bighorn Basin, Wyoming, USA). Mar. Petrol. Geol. 67, 230–248. https://doi.org/10.1016/j.marpetgeo.2015.05.026.

Barbier, M., Hamon, Y., Callot, J.-P., Floquet, M., Daniel, J.-M., 2012. Sedimentary and diagenetic controls on the multiscale fracturing pattern of a carbonate reservoir: the Madison Formation (Sheep Mountain, Wyoming, USA). Mar. Petrol. Geol. 29, 50–67. https://doi.org/10.1016/j.marpetgeo.2011.08.009.

Barbier, M., Hamon, Y., Doligez, B., Callot, J.-P., Floquet, M., Daniel, J.-M., 2011. Simulation stochastique couplée faciès et diagenèse. L'exemple de la diagenèse précoce dans la Formation Madison (Wyoming, USA). Oil Gas Sci. Technol. 67, 123–145. https://doi.org/10.2516/ogst/2011009.
Bathurst, R.G.C., 1971. Carbonate sediments and their diagenesis. In: Developments in Sedimentology, vol. 12.
Beaudoin, N., Bellahsen, N., Lacombe, O., Emmanuel, L., Pironon, J., 2014. Crustal-scale fluid flow during the tectonic evolution of the Bighorn Basin (Wyoming, USA). Basin Res. 26, 403–435. https://doi.org/10.1111/bre.12032.
Beckert, J., Vandeginste, V., John, C.M., 2015. Exploring the geological features and processes that control the shape and internal fabrics of late diagenetic dolomite bodies (Lower Khuff equivalent - Central Oman Mountains). Mar. Petrol. Geol. 68, 325–340. https://doi.org/10.1016/j.marpetgeo.2015.08.038.
Biehl, B.C., Reuning, L., Schoenherr, J., Lüders, V., Kukla, P.A., 2016. Impacts of hydrothermal dolomitization and thermochemical sulfate reduction on secondary porosity creation in deeply buried carbonates: a case study from the Lower Saxony Basin, northwest Germany. Am. Assoc. Petrol. Geol. Bull. 100, 597–621. https://doi.org/10.1306/01141615055.
Biteau, J.-J., Le Marrec, A., Le Vot, M., Masset, J.-M., 2006. The Aquitaine basin. Petrol. Geosci. 12, 247–273. https://doi.org/10.1144/1354-079305-674.
Braithwaite, C.J.R., Rizzi, G., Darke, G., 2004. The geometry and petrogenesis of dolomite hydrocarbon reservoirs: introduction. Geom. Petrog. Dolomite Hydrocarb. Reserv. Geol. Soc. London Spec. Publ. 235, 1–6. https://doi.org/10.1144/GSL.SP.2004.235.01.01.
Brauer, J.S., Baker, P.A., 1984. Experimental hydrothermal dedolomitization. Am. Assoc. Petrol. Geol. Bull. 68, 456–457.
Breesch, L., Swennen, R., Vincent, B., Ellison, R., Dewever, B., 2010. Dolomite cementation and recrystallisation of sedimentary breccias along the Musandam Platform margin (United Arab Emirates). J. Geochem. Explor. 106, 34–43. https://doi.org/10.1016/j.gexplo.2010.02.005.
Brinkmann, R., Lögters, H., 1968. Diapirs in western Pyrenees and foreland, Spain. In: Diapirism and Diapirs: a symposium. American Association of Petroleum Geologists 8, 275–292. https://doi.org/10.1306/M8361.
Burke, E.A.J., 2001. Raman microspectrometry of fluid inclusions. Lithos 55, 139–158. https://doi.org/10.1016/S0024-4937(00)00043-8.
Bustillo, M.A., 2010. Chapter 3 silicification of continental carbonates. Developments in Sedimentology. Elsevier, pp. 153–178. https://doi.org/10.1016/S0070-4571(09)06203-7.
Butler, G.P., Harris, P.M., Kendall CG, St C., 1982. Recent evaporites from the Abu Dhabi coastal flats. Depos. diagenetic spectra evaporites SEPM core Work 3. https://doi.org/10.2110/cor.82.01.0033.
Callot, J.-P., Breesch, L., Guilhaumou, N., Roure, F., Swennen, R., Vilasi, N., 2010. Paleo-fluids characterisation and fluid flow modelling along a regional transect in Northern United Arab Emirates (UAE). Arab. J. Geosci. 3, 413–437. https://doi.org/10.1007/s12517-010-0233-z.
Canérot, J., Hudec, M.R., Rockenbauch, K., 2005. Mesozoic diapirism in the Pyrenean orogen: salt tectonics on a transform plate boundary. Am. Assoc. Petrol. Geol. Bull. 89, 211–229. https://doi.org/10.1306/09170404007.
Canérot, J., Lenoble, J.-L., 1993. Diapirisme crétacé sur la marge ibérique des Pyrénées occidentales : exemple du pic de Lauriolle ; comparaison avec l'Aquitaine, les Pyrénées centrales et orientales. Bull. Société Géologique Fr. 164, 719–726.
Canérot, J., Lenoble, J.-L.J.-L., Marchand, D., Thierry, J., 1990. Nouveau schéma de corrélations stratigraphiques du Dogger-Malm dans les Pyérénées occidentales françaises. Comptes rendus l'Académie des Sci. 311, 1337–1343.
Canérot, J., Majesté-Menjoulas, C., Ternet, Y., 1999. Le cadre stratigraphique et géodynamique des altérites et des bauxites sur la marge ibérique des Pyrénées occidentales (France). C. R. Acad. Sc. Paris 328, 451–456.
Cantrell, D., Swart, P.K., Hagerty, R., 2004. Genesis and characterization of dolomite, arab-D reservoir, ghawar field, Saudi arabia. GeoArabia 9, 11–36.
Carmichael, S.K., Ferry, J.M., McDonough, W.F., 2008. Formation of replacement dolomite in the Latemar carbonate buildup, dolomites, Northern Italy: Part 1. Field relations, mineralogy, and geochemistry. Am. J. Sci. 308, 851–884. https://doi.org/10.2475/07.2008.03.
Castéras, M., Canérot, J., Paris, J., Tisin, D., Azambre, M., Alimen, H., 1970. Carte géologique de la France au 1/50 000: Feuille d'Oloron Sainte Marie. BRGM Orléans, Fr.
Caumon, M.-C., Dubessy, J., Robert, P., Tarantola, A., 2013. Fused-silica capillary capsules (FSCCs) as reference synthetic aqueous fluid inclusions to determine chlorinity by Raman spectroscopy. Eur. J. Mineral 25, 755–763. https://doi.org/10.1127/0935-1221/2013/0025-2280.
Caumon, M.-C., Tarantola, A., Mosser-Ruck, R., 2015. Raman spectra of water in fluid inclusions: I. Effect of host mineral birefringence on salinity measurement. J. Raman Spectrosc. 46, 969–976. https://doi.org/10.1002/jrs.4708.
Chaudhuri, S., Clauer, N., 1992. Signatures of radiogenic isotopes in deep subsurface waters in continents. In: Isotopic Signatures and Sedimentary Records. Lecture Notes in Earth Sciences 43, 497–529. https://doi.org/10.1007/BFb0009875.
Chen, Y.X., Schertl, H.P., Zheng, Y.F., Huang, F., Zhou, K., Gong, Y.Z., 2016. Mg–O isotopes trace the origin of Mg-rich fluids in the deeply subducted continental crust of Western Alps. Earth Planet Sci. Lett. 456, 157–167. https://doi.org/10.1016/j.epsl.2016.09.010.
Choquette, P.W., Hiatt, E.E., 2008. Shallow-burial dolomite cement: a major component of many ancient sucrosic dolomites. Sedimentology 55, 423–460. https://doi.org/10.1111/j.1365-3091.2007.00908.x.
Choukroune, P., 1992. Tectonic evolution of the Pyrenees. Annu. Rev. Earth Planet Sci. 20, 143–158. https://doi.org/10.1146/annurev.ea.20.050192.001043.
Choukroune, P., 1976. Structure et évolution tectonique de la zone nord-Pyrénéenne : analyse de la déformation dans une protion de chaîne à schistosité sub-verticale. Mémoires la société géologique Fr. 127, 1–116.
Choukroune, P., Le Pichon, X., Seguret, M., Sibuet, J., 1973. Bay of biscay and Pyrenees. Earth Planet Sci. Lett. 18 (1), 109–118. https://doi.org/10.1016/0012-821X(73)90041-1.
Choukroune, P., Roure, F., Pinet, B., 1990. Main results of the ECORS Pyrenees profile. Tectonophysics 173 (1–4), 411–423. https://doi.org/10.1016/0040-1951(90)90234-Y.
Clerc, C., Lagabrielle, Y., 2014. Thermal control on the modes of crustal thinning leading to mantle exhumation: insights from the cretaceous pyrenean hot paleomargins. Tectonics 33, 1340–1359. https://doi.org/10.1002/2013TC003471.
Clerc, C., Lagabrielle, Y., Labaume, P., Ringenbach, J.C., Vauchez, A., Nalpas, T., Bousquet, R., Ballard, J.F., Lahfid, A., Fourcade, S., 2016. Basement - cover decoupling and progressive exhumation of metamorphic sediments at hot rifted margin. Insights from the Northeastern Pyrenean analog. Tectonophysics 686, 82–97. https://doi.org/10.1016/j.tecto.2016.07.022.
Clerc, C., Lahfid, A., Monié, P., Lagabrielle, Y., Chopin, C., Poujol, M., Boulvais, P., Ringenbach, J.C., Masini, E., de Saint Blanquat, M., 2015. High-temperature metamorphism during extreme thinning of the continental crust: a reappraisal of the North Pyrenean passive paleomargin. Solid Earth 6, 643–668. https://doi.org/10.5194/se-6-643-2015.
Combes, P.-J., Peybernès, B., Leyreloup, A.F., 1998. Altérites et bauxites, témoins des marges europeenne et ibérique des Pyrénées occidentales au Jurassique supérieur - crétacé inférieur, à l'ouest de la vallée d'Ossau (Pyrénées-Atlantiques, France). C. R. Acad. Sc. Paris 327, 271–278.
Corre, B., 2017. La bordure nord de la plaque ibérique à l'Albo-Cénomanien. Architecture d'une marge passive de type ductile (Chaînons Béarnais, Pyrénées Occidentales).
Corre, B., Boulvais, P., Boiron, M.-C., Lagabrielle, Y., Marasi, L., Clerc, C., 2018. Fluid circulations in response to mantle exhumation at the passive margin setting in the north Pyrenean zone , France. Mineral. Petrol. 112, 647–670. https://doi.org/10.1007/s00710-018-0559-x.
Corre, B., Lagabrielle, Y., Labaume, P., Fourcade, S., Clerc, C., Balle, M., 2016. Deformation associated with mantle exhumation in a distal, hot passive margin environment : new constraints from the Saraillé Massif (Chaînons Béarnais, North-Pyrenean Zone). Compt. Rendus Geosci. 348, 279–289. https://doi.org/10.1016/j.crte.2015.11.007.
Cox, K.G., 1989. The role of mantle plumes in the development of continental drainage patterns. Nature 342, 873–877. https://doi.org/10.1038/342873a0.
Croizé, D., Renard, F., Gratier, J.P., 2013. Compaction and porosity reduction in carbonates: a review of observations, theory, and experiments. Advances in Geophysics, pp. 181–238. https://doi.org/10.1016/B978-0-12-380940-7.00003-2.
Davies, G.R., Smith Jr., L.B., 2006. Structurally controlled hydrothermal dolomite reservoir facies: an overview. Am. Assoc. Petrol. Geol. Bull. 90, 1641–1690. https://doi.org/10.1306/05220605164.
Debure, M., Lassin, A., Marty, N.C., Claret, F., Virgone, A., Calassou, S., Gaucher, E.C., 2019. Thermodynamic evidence of giant salt deposit formation by serpentinization: an alternative mechanism to solar evaporation. Sci. Rep. 9 https://doi.org/10.1038/s41598-019-48138-9.
Deffeyes, K.S., Lucia, J.F., Weyl, P.K., 1965. Dolomitization of recent and plio-pleistocene sediments by marine evaporite waters on bonaire, Netherlands antilles. Soc. Econ. Paleontol. Mineral. Spec. Publ. 13, 71–88. https://doi.org/10.2110/pec.65.07.0071.
Di Cuia, R., Riva, A., Scifoni, A., Moretti, A., Spötl, C., Caline, B., 2011. Dolomite characteristics and diagenetic model of the calcari grigi group (asiago plateau, southern alps - Italy): an example of multiphase dolomitization. Sedimentology 58, 1347–1369. https://doi.org/10.1111/j.1365-3091.2010.01212.x.
Douville, E., Bienvenu, P., Charlou, J.L., Donval, J.P., Fouquet, Y., Appriou, P., Gamo, T., 1999. Yttrium and rare earth elements in fluids from various deep-sea hydrothermal systems. Geochem. Cosmochim. Acta 63 (5), 627–643. https://doi.org/10.1016/S0016-7037(99)00024-1.
Douville, E., Charlou, J.L., Oelkers, E.H., Bienvenu, P., Jove Colon, C.F., Donval, J.P., Fouquet, Y., Prieur, D., Appriou, P., 2002. The rainbow vent fluids (36° 14'N, MAR ): the influence of ultramafic rocks and phase separation on trace metal content in Mid-Atlantic Ridge hydrothermal fluids. Chem. Geol. 184 (1–2), 37–48. https://doi.org/10.1016/S0009-2541(01)00351-5.
Drost, K., Chew, D., Petrus, J.A., Scholze, F., Woodhead, J.D., Schneider, J.W., Harper, D.A.T., 2018. An image mapping approach to U-Pb LA-ICP-MS carbonate dating and applications to direct dating of carbonate sedimentation. G-cubed 19 (12), 4631–4648. https://doi.org/10.1029/2018GC007850.
Dubessy, J., Lhomme, T., Boiron, M.-C., Rull, F., 2002. Determination of chlorinity in aqueous fluids using Raman spectroscopy of the stretching band of water at room temperature: application to fluid inclusions. Appl. Spectrosc. 56, 99–106. https://doi.org/10.1366/0003702021954278.
Ducoux, M., Jolivet, L., Callot, J.-P., Aubourg, C., Masini, E., Lahfid, A., Homonnay, E., Cagnard, F., Gumiaux, C., Baudin, T., 2019. The Nappe des Marbres Unit of the Basque-Cantabrian Basin: the Tectono-thermal Evolution of a Fossil Hyperextended Rift Basin. Tectonics 38, 3881–3915. https://doi.org/10.1029/2018TC005348.
Duggan, J.P., Mountjoy, E.W., Stasiuk, L.D., 2001. Fault-controlled dolomitization at Swan Hills Simonette oil field (Devonian), deep basin west-central Alberta, Canada. Sedimentology 48 (2), 301–323. https://doi.org/10.1046/j.1365-3091.2001.00364.x.
Dunham, R.J., 1962. Classification of carbonate rocks according to depositional textures. Classification of Carbonate Rocks–A Symposium. American Association of Petroleum Geologists, pp. 108–121, 10.1306/M1357.

Elias Bahnan, A., 2019. Circulation des fluides et diagenèse du système pétrolier de Lacq : Impact de l'évolution géodynamique. Université de Lorraine.
Elias Bahnan, A., Carpentier, C., Pironon, J., Ford, M., Ducoux, M., Barré, G., Mangenot, X., Gaucher, E.C., 2020. Impact of geodynamics on fluid circulation and diagenesis of carbonate reservoirs in a foreland basin: example of the Upper Lacq reservoir (Aquitaine basin, SW France). Mar. Petrol. Geol. 111, 676–694. https://doi.org/10.1016/j.marpetgeo.2019.08.047.
Embry, A.F., Klovan, E.J., 1971. Upper Devonian Stratigraphy, Northeastern Bank Island, N.W.T. Bull. Can. Petrol. Geol. 19, 705–729. https://doi.org/10.35767/GSCPGBULL.19.4.705.
Fauré, P., 2002. Le Lias des Pyrénées tome 2 Partie 2.
Fischer, M.P., Kenroy, P.R., Smith, A.P., 2013. Fluid systems around salt diapirs, 50902. AAPG Search and Discovery.
Frezzotti, M.L., Tecce, F., Casagli, A., 2012. Raman spectroscopy for fluid inclusion analysis. J. Geochem. Explor. 112, 1–20. https://doi.org/10.1016/j.gexplo.2011.09.009.
Friedman, I., O'Neil, J.R., 1977. Data of geochemistry sixth edition. Geol. Surv. Prof. Pap. 440-KK, 1–117.
Gao, G., Land, L.S., Elmore, R.D., 1995. Multiple episodes of dolomitization in the Arbuckle Group, Arbuckle Mountains, South-Central Oklahoma: field, petrographic and, geochemical evidence. J. Sediment. Petrol. 65 (2a), 321–331. https://doi.org/10.1306/D42680AE-2B26-11D7-8648000102C1865D.
Garaguly, I., Varga, A., Raucsik, B., Schubert, F., Czuppon, G., Frei, R., 2018. Pervasive early diagenetic dolomitization , subsequent hydrothermal alteration , and late stage hydrocarbon accumulation in a Middle Triassic carbonate sequence ( Szeged Basin , SE Hungary ). Mar. Petrol. Geol. 98, 270–290. https://doi.org/10.1016/j.marpetgeo.2018.07.024.
Gisquet, F., Lamarche, J., Floquet, M., Borgomano, J., Masse, J.-P.P., Caline, B., 2013. Three-dimensional structural model of composite dolomite bodies in folded area (upper jurassic of the Etoile massif, southeastern France). Am. Assoc. Petrol. Geol. Bull. 97, 1477–1501. https://doi.org/10.1306/04021312016.
Golberg, J.M., Leyreloup, A.F., 1990. High temperature-low pressure Cretaceous metamorphism related to crustal thinning (Eastern North Pyrenean Zone, France). Contrib. Mineral. Petrol. 104, 194–207. https://doi.org/10.1007/BF00306443.
Goldhammer, R.K., 1997. Compaction and decompaction algorithms for sedimentary carbonates. J. Sediment. Res. 67 (1), 26–35. https://doi.org/10.1306/D42684E1-2B26-11D7-8648000102C1865D.
Goldstein, R.H., Reynolds, T.J., 1994. Systematics of Fluid Inclusions in Diagenetic Minerals. Society for Sedimentary Geology. https://doi.org/10.2110/scn.94.31.
Gong, Z., Langereis, C.G., Mullender, T.A.T., 2008. The rotation of iberia during the aptian and the opening of the bay of biscay. Earth Planet Sci. Lett. 273, 80–93. https://doi.org/10.1016/j.epsl.2008.06.016.
Gonzalez, E., Ferket, H., Callot, J.-P., Guilhaumou, N., Ortuno, S., Roure, F., 2012. Paleoburial, hydrocarbon generation, and migration in the Córdoba Platform and Veracruz Basin: insights from fluid inclusion studies and two-dimensional (2D) basin modeling. Soc. Econ. Paleontol. Mineral. Spec. Publ. 103, 167–186. https://doi.org/10.2110/sepmsp.103.167.
Gregg, J.M., Sibley, D.F., 1987. Classification of dolomite rock texture. J. Sediment. Petrol. 57 (6), 967–975. https://doi.org/10.1306/212F8CBA-2B24-11D7-8648000102C1865D.
Grimaldi, M.-H., 1988. La dolomie tidale du Jurassique terminal des Pyrénées occidentales Sédimentologie, Diagenèse polyphasée et contexte dynamique.
Grunnaleite, I., Mosbron, A., 2019. On the significance of salt modelling-example from modelling of salt tectonics, temperature and maturity around salt structures in Southern North Sea. Geosci. 9 https://doi.org/10.3390/geosciences9090363.
Guo, C., Chen, D., Qing, H., Dong, S., Li, G., Wang, D., Qian, Y., Liu, C., 2016. Multiple dolomitization and later hydrothermal alteration on the Upper Cambrian-Lower Ordovician carbonates in the northern Tarim Basin, China. Mar. Petrol. Geol. 72, 295–316. https://doi.org/10.1016/j.marpetgeo.2016.01.023.
Haeri-Ardakani, O., Al-Aasm, I.S., Coniglio, M., 2013a. Petrologic and geochemical attributes of fracture-related dolomitization in Ordovician carbonates and their spatial distribution in southwestern Ontario, Canada. Mar. Petrol. Geol. 43, 409–422. https://doi.org/10.1016/j.marpetgeo.2012.12.006.
Haeri-Ardakani, O., Al-Aasm, I.S., Coniglio, M., 2013b. Fracture mineralization and fluid flow evolution: an example from Ordovician-Devonian carbonates, southwestern Ontario, Canada. Geofluids 13, 1–20. https://doi.org/10.1111/gfl.12003.
Hallam, A., 2001. A review of the broad pattern of Jurassic sea-level changes and their possible causes in the light of current knowledge. Palaeogeogr. Palaeoclimatol. Palaeoecol. 167, 23–37. https://doi.org/10.1016/S0031-0182(00)00229-7.
Haq, B.U., Hardenbol, J., Vail, P.R., 1987. Chronology of fluctuating sea levels since the triassic. Science 235, 1156–1167. https://doi.org/10.1126/science.235.4793.1156.
Hardie, L.A., 1987. Perspectives. Dolomitization: a critical view of some current views. J. Sediment. Petrol. 57, 166–183. https://doi.org/10.1306/212f8ad5-2b24-11d7-8648000102c1865d.
Hart, N.R., Stockli, D.F., Lavier, L.L., Hayman, N.W., 2017. Thermal evolution of a hyperextended rift basin, Mauléon Basin, western Pyrenees. Tectonics 36, 1103–1128. https://doi.org/10.1002/2016TC004365.
Hendry, J.P., Gregg, J.M., Shelton, K.L., Somerville, I.D., Crowley, S.F., 2015. Origin, characteristics and distribution of fault-related and fracture-related dolomitization: insights from Mississippian carbonates, Isle of Man. Sedimentology 62, 717–752. https://doi.org/10.1111/sed.12160.
Hesse, R., 1987. Selective and reversible carbonate—silica replacements in Lower Cretaceous carbonate-bearing turbidites of the Eastern Alps. Sedimentology 34, 1055–1077. https://doi.org/10.1111/j.1365-3091.1987.tb00592.x.
Heydari, E., 1997. Hydrotectonic models of burial diagenesis in platforme carbonates based on formation water geochemistry in north american sedimentary basins. In Basin-Wide Diagenetic Patterns: Integrated Petrologic, Geochemical, and Hydrologic Considerations. Soc. Sediment. Geol. 57 https://doi.org/10.2110/pec.97.57.0053.
Hill, C.A., Polyak, V.J., Asmerom, Y., Provencio, P., 2016. Constraints on a Late Cretaceous uplift, denudation, and incision of the Grand Canyon region, southwestern Colorado Plateau, USA, from U-Pb dating of lacustrine limestone. Tectonics 35, 896–906. https://doi.org/10.1002/2016TC004166.
Hoareau, G., Claverie, F., Pecheyran, C., Paroissin, C., Motte, G., Chailan, O., Girard, J., n.d. Direct U-Pb Dating of Carbonates from Micron Scale fsLA-ICPMS Images Using Robust Regression. Geochronology in press. https://doi.org/10.5194/gchron-2020-10.
Horita, J., 2014. Oxygen and carbon isotope fractionation in the system dolomite – water – CO2 to elevated temperatures. Geochem. Cosmochim. Acta 129, 111–124. https://doi.org/10.1016/j.gca.2013.12.027.
Illing, L.V., 1964. Penecontemporary dolomite in the Persian gulf. Am. Assoc. Petrol. Geol. Bull. 48, 532–533.
Illing, L.V., 1959. Deposition and diagenesis of some Upper Palaeozoic carbonate sediments in Western Canada. 5th World Pet. Congr.
Incerpi, N., Manatschal, G., Martire, L., Gerdes, A., Bertok, C., 2020. Characteristics and timing of hydrothermal fluid circulation in the fossil Pyrenean hyperextended rift system: new constraints from the Chaînons Béarnais (W Pyrenees). Int. J. Earth Sci. 109, 1071–1093. https://doi.org/10.1007/s00531-020-01852-6.
Iriarte, E., Lopez-Horgue, M.A., Schroeder, S., Caline, B., 2012. Interplay between fracturing and hydrothermal fluid flow in the Ason Valley hydrothermal dolomites (Basque – cantabrian Basin, Spain). Geol. Soc. London Spec. Publ. 370, 207–227. https://doi.org/10.1144/SP370.10.
Izquierdo-Llavall, E., Menant, A., Aubourg, C., Callot, J.-P., Hoareau, G., Lahfid, A., Camps, P., Pere, E., 2020. Pre-orogenic folds and syn-orogenic basement tilts in an inverted hyperextended margin : the northern Pyrenees case study. Tectonics 39 (7). https://doi.org/10.1029/2019TC005719.
Jackson, M.P.A., Hudec, M.R., 2017. Salt Tectonics. Cambridge University Press, doi: 10.1017/9781139003988.
James, N.P., Choquette, P.W., 1984. Diagenesis 9 -. Limestones - the meteoric diagenetic environment. Geosci. Can. 11 (4), 161–194.
James, V., 1998. La plate-forme carbonatée ouest-pyrénéenne au Jurassique moyen et supérieur : Stratigraphie séquentielle, stades d'évolution, relations avec la subsurface en Aquitaine méridionale.
James, V., Canérot, J., 1999. Diapirisme et structuration post-triasique des Pyrénées occidentales et de l'Aquitaine méridionale (France). Eclogae Geol. Helv. 92, 63–72. https://doi.org/10.5169/seals-168647.
Jammes, S., Lavier, L.L., Manatschal, G., 2010a. Extreme crustal thinning in the bay of biscay and the western Pyrenees: from observations to modeling. G-cubed 11. https://doi.org/10.1029/2010GC003218.
Jammes, S., Manatschal, G., Lavier, L.L., Masini, E., 2009. Tectonosedimentary evolution related to extreme crustal thinning ahead of a propagating ocean: example of the western Pyrenees. Tectonics 28, 1–24. https://doi.org/10.1029/2008TC002406.
Jammes, S., Tiberi, C., Manatschal, G., 2010b. 3D architecture of a complex transcurrent rift system: the example of the Bay of Biscay-Western Pyrenees. Tectonophysics 489, 210–226. https://doi.org/10.1016/j.tecto.2010.04.023.
Jensen, P.K., 1983. Calculations on the thermal conditions around a salt diapir. Geophys. Prospect. 31, 481–489. https://doi.org/10.1111/j.1365-2478.1983.tb01064.x.
Jochum, K.P., Weis, U., Stoll, B., Kuzmin, D., Yang, Q., Raczek, I., Jacob, D.E., Stracke, A., Birbaum, K., Frick, D.A., Günther, D., Enzweiler, J., 2011. Determination of reference values for NIST SRM 610-617 glasses following ISO guidelines. Geostand. Geoanal. Res. 35, 397–429. https://doi.org/10.1111/j.1751-908X.2011.00120.x.
Jochum, K.P., Wilson, S.A., Abouchami, W., Amini, M., Chmeleff, J., Eisenhauer, A., Hegner, E., Iaccheri, L.M., Kieffer, B., Krause, J., Mcdonough, W.F., Mertz-Kraus, R., Raczek, I., Rudnick, R.L., Scholz, D., Steinhoefel, G., Stoll, B., Stracke, A., Tonarini, S., Weis, D., Weis, U., Woodhead, J.D., 2010. GSD-1G and MPI-DING reference glasses for in situ and bulk isotopic determination. Geostand. Geoanal. Res. 35, 193–226. https://doi.org/10.1111/j.1751-908X.2010.00114.x.
Jonas, L., Müller, T., Dohmen, R., Baumgartner, L.P., Putlitz, B., 2015. Transport-controlled hydrothermal replacement of calcite by Mg-carbonates. Geology 43, 779–783. https://doi.org/10.1130/G36934.1.
Jourdon, A., Mouthereau, F., Le Pourhiet, L., Callot, J.-P., 2020. Topographic and tectonic evolution of mountain belts controlled by salt thickness and rift architecture. Tectonics 39. https://doi.org/10.1029/2019TC005903.
Kaczmarek, S.E., Sibley, D.F., 2011. On the evolution of dolomite stoichiometry and cation order during high-temperature synthesis experiments: an alternative model for the geochemical evolution of natural dolomites. Sediment. Geol. 240, 30–40. https://doi.org/10.1016/j.sedgeo.2011.07.003.
Kaiser, B.O., Cacace, M., Scheck-Wenderoth, M., Lewerenz, B., 2011. Characterization of main heat transport processes in the Northeast German Basin: constraints from 3-D numerical models. G-cubed 12, 1–17. https://doi.org/10.1029/2011GC003535.
Kim, S.T., Mucci, A., Taylor, B.E., 2007. Phosphoric acid fractionation factors for calcite and aragonite between 25 and 75 °C: Revisited. Chem. Geol. 246, 135–146. https://doi.org/10.1016/j.chemgeo.2007.08.005.
Koeshidayatullah, A., Corlett, H., Stacey, J., Swart, P.K., Boyce, A., Robertson, H., Whitaker, F., Hollis, C., 2020. Evaluating new fault-controlled hydrothermal dolomitization models: insights from the cambrian dolomite, western Canadian sedimentary basin. Sedimentology 67 (6), 2945–2973. https://doi.org/10.1111/sed.12729.
Krupp, R.E., 2005. Formation and chemical evolution of magnesium chloride brines by evaporite dissolution processes - implications for evaporite geochemistry. Geochem. Cosmochim. Acta 69, 4283–4299. https://doi.org/10.1016/j.gca.2004.11.018.

Labaume, P., Teixell, A., 2020. Evolution of salt structures of the Pyrenean rift (Chaînons Béarnais, France): from hyper-extension to tectonic inversion. Tectonophysics 785. https://doi.org/10.1016/j.tecto.2020.228451.
Lagabrielle, Y., Bodinier, J.-L., 2008. Submarine reworking of exhumed subcontinental mantle rocks: field evidence from the Lherz peridotites, French Pyrenees. Terra. Nova 20, 11–21. https://doi.org/10.1111/j.1365-3121.2007.00781.x.
Lagabrielle, Y., Clerc, C., Vauchez, A., Lahfid, A., Labaume, P., Azambre, B., Fourcade, S., Dautria, J., 2016. Very high geothermal gradient during mantle exhumation recorded in mylonitic marbles and carbonate breccias from a Mesozoic Pyrenean palaeomargin (Lherz area, North Pyrenean, France). Compt. Rendus Geosci. 348, 290–300. https://doi.org/10.1016/j.crte.2015.11.004.
Lagabrielle, Y., Labaume, P., De Saint Blanquat, M., 2010. Mantle exhumation, crustal denudation, and gravity tectonics during Cretaceous rifting in the Pyrenean realm (SW Europe): insights from the geological setting of the lherzolite bodies. Tectonics 29, 1–26. https://doi.org/10.1029/2009TC002588.
Land, L.S., 1998. Failure to precipitate dolomite at 25 °C from dilute solution despite 1000-fold oversaturation after 32 years. Aquat. Geochem. 4, 361–368. https://doi.org/10.1023/A:1009688315854.
Land, L.S., 1985. The origin of massive dolomite. J. Geol. Educ. 33, 112–125. https://doi.org/10.5408/0022-1368-33.2.112.
Land, L.S., 1980. The isotopic and trace element geochemistry of dolomite: the state of the art. Soc. Econ. Paleontol. Mineral. 28, 87–110.
Land, L.S., 1973. Contemporaneous dolomitization of Middle Pleistocene reefs by meteoric water, North Jamaica. Bull. Mar. Sci. 23, 64–92.
Land, L.S., Prezbindowski, D.R., 1981. The origin and evolution of saline formation water, lower cretaceous carbonates, South-Central Texas. U.S.A. Dev. Water Sci. 54, 51–74. https://doi.org/10.1016/S0167-5648(08)70595-1.
Lenoble, J.-L., 1992. Les plates-formes carbonatées ouest-pyrénéennes du Dogger à l'Albien : Stratigraphie séquentielle et évolution géodynamique. Université Paul Sabatier de Toulouse (Sciences).
Lenoble, J.-L., Canérot, J., 1992. La lame extrusive de Pont Suzon (Zone Nord-Pyrénéenne en Vallée d'Aspe) : reprise pyrénéenne d'une ride diapirique transverse d'âge crétacé. C. R. Acad. Sc. Paris 314, 387–391.
Lescoutre, R., Tugend, J., Brune, S., Masini, E., Manatschal, G., 2019. Thermal evolution of asymmetric hyperextended magma-poor rift systems: results from numerical modeling and pyrenean field observations. G-cubed 20 (10), 4567–4587. https://doi.org/10.1029/2019GC008600.
Longstaffe, F.J., 1987. Stable isotope studies of diagenetic processes. In Stable isotope geochemistry of low temperature processes. Mineralogical Association of Canada 13, 187–257.
Lopez-Horgue, M.A., Iriarte, E., Schröder, S., Fernandez-Mendiola, P.A., Caline, B., Corneyllie, H., Frémont, J., Sudrie, M., Zerti, S., 2010. Structurally controlled hydrothermal dolomites in albian carbonates of the ason valley, Basque cantabrian basin, northern Spain. Mar. Petrol. Geol. 27, 1069–1092. https://doi.org/10.1016/j.marpetgeo.2009.10.015.
Lovering, T.S., 1969. The origin of hydrothermal and low temperature dolomite. Econ. Geol. 64, 743–754. https://doi.org/10.2113/gsecongeo.64.7.743.
Lukoczki, G., Haas, J., Gregg, J.M., Machel, H.G., Kele, S., John, C.M., 2018. Multi-phase dolomitization and recrystallization of Middle Triassic shallow marine-peritidal carbonates from the Mecsek Mts. (SW Hungary), as inferred from petrography, carbon, oxygen, strontium and clumped isotope data. Mar. Petrol. Geol. 101, 440–458. https://doi.org/10.1016/j.marpetgeo.2018.12.004.
Machel, H.G., 2004. Concepts and models of dolomitization: a critical reappraisal. Geol. Soc. London Spec. Publ. 235, 7–63. https://doi.org/10.1144/GSL.SP.2004.235.01.02.
Machel, H.G., Cavell, P.A., 1999. Low-flux, tectonically-induced squeegee fluid flow ("hot flash") into the Rocky Mountain Foreland Basin. Bull. Can. Petrol. Geol. 47 (4), 510–533. https://doi.org/10.35767/gscpgbull.47.4.510.
Machel, H.G., Mountjoy, E.W., 1986. Chemistry and environments of dolomitization - a reappraisal. Earth Sci. Rev. 23, 175–222. https://doi.org/10.1016/0012-8252(86)90017-6.
Martín-Martín, J.D., Travé, A., Gomez-Rivas, E., Salas, R., Sizun, J.-P., Vergés, J., Corbella, M., Stafford, S.L., Alfonso, P., 2015. fault-controlled and stratabound dolostones in the late aptian–earliest albian benassal formation (maestrat basin, E Spain): petrology and geochemistry constrains. Mar. Petrol. Geol. 65, 83–102. https://doi.org/10.1016/j.marpetgeo.2015.03.019.
Masini, E., Manatschal, G., Tugend, J., Mohn, G., Flament, J.-M., 2014. The tectono - sedimentary evolution of a hyper - extended rift basin: the example of the Arzacq – mauléon rift system (Western Pyrenees, SW France). Int. J. Earth Sci. 103, 1569–1596. https://doi.org/10.1007/s00531-014-1023-8.
McArthur, J.M., Howarth, R.J., Bailey, T.R., 2001. Strontium isotope Stratigraphy : LOWESS version 3 : best fit to the marine Sr-isotope curve for 0 – 509 Ma and accompanying look-up table for deriving numerical age. J. Geol. 109, 155–170. https://doi.org/10.1086/319243.
McHargue, T.R., Price, R.C., 1982. Dolomite from clay in argillaceous or shale-associated marine carbonates. J. Sediment. Petrol. 52 (3), 873–886. https://doi.org/10.1306/212F807B-2B24-11D7-8648000102C1865D.
Mello, U.T., Karner, G.D., Anderson, R.N., 1995. Role of salt in restraining the maturation of subsalt source rocks. Mar. Petrol. Geol. 12, 697–716. https://doi.org/10.1016/0264-8172(95)93596-V.
Montanez, I.P., 1994. Late diagenetic dolomitization of Lower Ordovician, Upper Knox carbonates: a record of the hydrodynamic evolution of the southern Appalachian Basin. Am. Assoc. Petrol. Geol. Bull. 78, 1210–1239. https://doi.org/10.1306/a25feab3-171b-11d7-8645000102c1865d.
Moore, C., Wade, W.J., 2013. Carbonate diagenesis: introduction and tools. Dev. Sedimentol. 67, 67–89. https://doi.org/10.1016/B978-0-444-53831-4.00005-7.
Moragas, M., Baqués, V., Travé, A., Martín-Martín, J.D., Saura, E., Messager, G., Hunt, D., Vergés, J., 2020. Diagenetic evolution of lower Jurassic platform carbonates flanking the Tazoult salt wall (Central High Atlas, Morocco). Basin Res. 32, 546–566. https://doi.org/10.1111/bre.12382.
Morrow, D.W., 1982. Descriptive field classification of sedimentary and diagenetic breccia fabrics in carbonate rocks. Bull. Can. Petrol. Geol. 30 (3), 227–229. https://doi.org/10.35767/gscpgbull.30.3.227.
Mountjoy, E.W., Halim-Dihardja, M.K., 1991. Multiple phase fracture and fault-controlled burial dolomitization, upper devonian wabamun group, alberta. J. Sediment. Petrol. 61 (4), 590–612. https://doi.org/10.1306/D426776C-2B26-11D7-8648000102C1865D.
Mountjoy, E.W., Qing, H., McNutt, R.H., 1992. Strontium isotopic composition of Devonian dolomites, Western Canada Sedimentary Basin: significance of sources of dolomitizing fluids. Appl. Geochem. 7, 59–75. https://doi.org/10.1016/0883-2927(92)90015-U.
Mouthereau, F., Filleaudeau, P.Y., Vacherat, A., Pik, R., Lacombe, O., Fellin, M.G., Castelltort, S., Christophoul, F., Masini, E., 2014. Placing limits to shortening evolution in the Pyrenees: role of margin architecture and implications for the Iberia/Europe convergence. Tectonics 33, 2283–2314. https://doi.org/10.1002/2014TC003663.
Mozafari, M., Swennen, R., Balsamo, F., El Desouky, H., Storti, F., Taberner, C., Desouky, H. El, Storti, F., Taberner, C., 2019. Fault-controlled dolomitization in the Montagna dei Fiori Anticline (Central Apennines, Italy): record of a dominantly pre-orogenic fluid migration. Solid Earth Discuss 10, 1355–1383. https://doi.org/10.5194/se-2018-136.
Muñoz, J.A., 1992. Evolution of a continental collision belt: ECORS-Pyrenees crustal balanced cross-section. Thrust Tectonics 235–246. https://doi.org/10.1007/978-94-011-3066-0_21.
Nader, F.H., López-Horgue, M.A., Shah, M.M., Dewit, J., Garcia, D., Swennen, R., Iriarte, E., Muchez, P., Caline, B., 2012. Les dolomies hydrothermales de Ranero (Albien, Vallée de la Karrantza, nord-ouest de l'Espagne): conséquences sur les modèles génétiques. Oil Gas Sci. Technol. 67, 9–29. https://doi.org/10.2516/ogst/2011165.
Nader, F.H., Swennen, R., 2004. The hydrocarbon potential of Lebanon: new insights from regional correlations and studies of Jurassic dolomitization. J. Petrol. Geol. 27, 253–275. https://doi.org/10.1111/j.1747-5457.2004.tb00058.x.
Nader, F.H., Swennen, R., Ellam, R.M., 2004. Reflux stratabound dolostone and hydrothermal volcanism-associated dolostone: a two-state dolomitization model (Jurassic, Lebanon). Sedimentology 51, 339–360. https://doi.org/10.1111/j.1365-3091.2004.00629.x.
Oliver, J., 1986. Fluids expelled tectonically from orogenic belts: their role in hydrocarbon migration and other geologic phenomena. Geology 14, 99–102. https://doi.org/10.1130/0091-7613(1986)14<99:FETFOB>2.0.CO;2.
Pedrosa, E.T., Putnis, C.V., Putnis, A., 2016. The pseudomorphic replacement of marble by apatite: the role of fluid composition. Chem. Geol. 425, 1–11. https://doi.org/10.1016/j.chemgeo.2016.01.022.
Péré, P., 1989. La formation dolomitique du Mailh Arrouy Dogger Kimméridgien inférieur (Etude à l'affleurement dans les Chaînons béarnais du réservoir gazéifére de Meillon). Pyrénées occidentales (France). Sédimentation, Structuration, Diagenèses. Université de Pau et des Pays de l'Adour.
Péré, P., 1987. Dolomitisations et diagenèses successives avec passage au métamorphisme: dolomies callovo-oxfordiennes des Pyrénées occidentales. France. C. R. Acad. Sc. Paris 305, 391–395.
Peterson, K., Lerche, I., 1995. Quantification of thermal anomalies in sediments around salt structures. Geothermics 24 (2), 253–268. https://doi.org/10.1016/0375-6505(94)00051-D.
Pinto, V.H., Manatschal, G., Karpoff, A.M., Ulrich, M., Viana, A.R., 2017. Seawater storage and element transfer associated with mantle serpentinization in magma-poor rifted margins: a quantitative approach. Earth Planet Sci. Lett. 459, 227–237. https://doi.org/10.1016/j.epsl.2016.11.023.
Piper, D.Z., 1974. Rare earth elements in the sedimentary cycle: a summary. Chem. Geol. 14, 285–304. https://doi.org/10.1016/0009-2541(74)90066-7.
Puigdefàbregas, C., Souquet, P., 1986. Tecto-sedimentary cycles and depositional sequences of the mesozoic and tertiary from the Pyrenees. Tectonophysics 129, 173–203. https://doi.org/10.1016/0040-1951(86)90251-9.
Putnis, A., 2009. Mineral replacement reactions. Rev. Mineral. Geochem. 70, 87–124. https://doi.org/10.2138/rmg.2009.70.3.
Putnis, A., 2002. Mineral replacement reactions: from macroscopic observations to microscopic mechanisms. Mineral. Mag. 66, 689–708. https://doi.org/10.1180/0026461026650056.
Quesnel, B., Boiron, M.-C., Cathelineau, M., Truche, L., Rigaudier, T., Bardoux, G., Agrinier, P., De Saint Blanquat, M., Masini, E., Gaucher, E.C., 2019. Nature and origin of mineralizing fluids in hyperextensional systems: the case of cretaceous Mg metasomatism in the Pyrenees. Geofluids 2019. https://doi.org/10.1155/2019/7213050.
Railsback, L.B., Hood, E.C., 2001. A survey of multi-stage diagenesis and dolomitization of Jurassic limestones along a regional shelf-to-basin transect in the Ziz Valley, Central High Atlas Mountains, Morocco. Sediment. Geol. 139, 285–317. https://doi.org/10.1016/S0037-0738(00)00164-0.
Renard, S., Pironon, J., Sterpenich, J., Lescanne, M., Gaucher, E.C., 2018. Diagenesis in Mesozoic carbonate rocks in the North Pyrénées (France) from mineralogy and fluid inclusion analysis: example of Rousse reservoir and caprock. Chem. Geol. 508, 30–46. https://doi.org/10.1016/j.chemgeo.2018.06.017.
Révillon, S., Jouet, G., Bayon, G., Rabineau, M., Dennielou, B., Hémond, C., Berné, S., 2011. The provenance of sediments in the gulf of lions, western mediterranean sea. G-cubed 12. https://doi.org/10.1029/2011GC003523.

Roberts, N.M.W., Rasbury, E.T., Parrish, R.R., Smith, C.J., Horstwood, M.S.A., Condon, D.J., 2017. A calcite reference material for LA-ICP-MS U-Pb geochronology. G-cubed 18, 2807–2814. https://doi.org/10.1002/2016GC006784.Received.

Rollion-Bard, C., Blamart, D., Cuif, J.P., Juillet-Leclerc, A., 2003. Microanalysis of C and O isotopes of azooxanthellate and zooxanthellate corals by ion microprobe. Coral Reefs 22, 405–415. https://doi.org/10.1007/s00338-003-0347-9.

Rollion-Bard, C., Marin-Carbonne, J., 2011. Determination of SIMS matrix effects on oxygen isotopic compositions in carbonates. J. Anal. At. Spectrom. 26, 1285–1289. https://doi.org/10.1039/c0ja00213e.

Rosenbaum, G., Lister, G.S., Duboz, C., 2002. Relative motions of africa, iberia and Europe during alpine orogeny. Tectonophysics 359, 117–129. https://doi.org/10.1016/S0040-1951(02)00442-0.

Rosenbaum, J., Sheppard, S.M.F., 1986. An isotopic study of siderites dolomites and ankerites at high temperatures. Geochem. Cosmochim. Acta 50, 1147–1150. https://doi.org/10.1016/0016-7037(86)90396-0.

Roure, F., Andriessen, P., Callot, J.P., Faure, J.L., Ferket, H., Gonzales, E., Guilhaumou, N., Lacombe, O., Malandain, J., Sassi, W., Schneider, F., Swennen, R., Vilasi, N., 2010. The use of palaeo-thermo-barometers and coupled thermal, fluid flow and pore-fluid pressure modelling for hydrocarbon and reservoir prediction in fold and thrust belts. Geol. Soc. Spec. Publ. 348, 87–114. https://doi.org/10.1144/SP348.6.

Roure, F., Swennen, R., Schneider, F., Faure, J.L., Ferket, H., Guilhaumou, N., 2005. Incidence and importance of tectonics and natural fluid migration on reservoir evolution in foreland fold-and-thrust belts. Oil Gas Sci. Technol. - Rev. IFP 60, 67–106. https://doi.org/10.2516/ogst:2005006.

Rustichelli, A., Iannace, A., Tondi, E., Di Celma, C., Cilona, A., Giorgioni, M., Parente, M., Girundo, M., Invernizzi, C., 2017. Fault-controlled dolomite bodies as palaeotectonic indicators and geofluid reservoirs: new insights from Gargano Promontory. Sedimentology 64, 1871–1900. https://doi.org/10.1111/ijlh.12426.

Salardon, R., Carpentier, C., Bellahsen, N., Pironon, J., France-Lanord, C., 2017. Interactions between tectonics and fluid circulations in an inverted hyper-extended basin: example of mesozoic carbonate rocks of the western North Pyrenean Zone (Chaînons Béarnais, France). Mar. Petrol. Geol. 80, 563–586. https://doi.org/10.1016/j.marpetgeo.2016.11.018.

Saspiturry, N., 2019. Evolution sédimentaire, structurale et thermique d'un rift hyper-aminci: de l'héritage post-hercynien à l'inversion alpine Exemple du bassin de Mauléon (Pyrénées). Université Bordeaux Montaigne.

Saspiturry, N., Razin, P., Baudin, T., Serrano, O., Issautier, B., Lasseur, E., Allanic, C., Thinon, I., Leleu, S., 2019. Symmetry vs asymmetry of a hyper-thinned rift: example of the mauleon basin. Mar. Petrol. Geol. 104, 86–105. https://doi.org/10.1016/j.marpetgeo.2019.03.031.

Scholle, P.A., Ulmer-Scholle, D.S., 2003. A Color Guide Petrography of Carbonate Rocks: Grains, Textures, Porosity, Diagenesis. AAPG, Tulsa, Oklahoma, U.S.A.

Selig, F., Wallick, G.C., 1966. Temperature distribution in salt domes and surrounding sediments. Geophysics 31 (2), 346–361. https://doi.org/10.1190/1.1439777.

Shah, M.M., Nader, F.H., Dewit, J., Swennen, R., Garcia, D., 2010. Fault-related hydrothermal dolomites in Cretaceous carbonates (Cantabria, northern Spain): results of petrographic, geochemical and petrophysical studies. Bull. la Soc. Geol. Fr. 181, 391–407. https://doi.org/10.2113/gssgfbull.181.4.391.

Sharp, I., Gillespie, P., Morsalnezhad, D., Taberner, C., Karpuz, R., Vergés, J., Horbury, A., Pickard, N., Garland, J., Hunt, D., 2010. Stratigraphic architecture and fracture-controlled dolomitization the Cretaceous Khami and Bangestan groups: an outcrop case study, Zagros Mountains, Iran. Geol. Soc. Spec. Publ. 329, 343–396. https://doi.org/10.1144/SP329.14.

Sibley, D.F., Nordeng, S.H., Borkowski, M.L., 1994. Dolomitization kinetics in hydrothermal bombs and natural settings. J. Sediment. Res. A Sediment. Petrol. Process. 630–637. https://doi.org/10.1306/d4267e29-2b26-11d7-8648000102c1865d.

Sibuet, J.-C., Srivastava, S.P., Spakman, W., 2004. Pyrenean orogeny and plate kinematics. J. Geophys. Res. 109, 1–18. https://doi.org/10.1029/2003JB002514.

Spencer-Cervato, C., Mullis, J., 1992. Chemical study of tectonically controlled hydrothermal dolomitization: an example from the Lessini mountains. Italy. Geol. Rundschau 81, 347–370. https://doi.org/10.1007/BF01828603.

Stoakes, F., 1987. Fault Controlled Dolomitization of the Wabamum Group, Tangent Field, Peace River Arch, Alberta. Devonian Lithofacies Reserv. Devonian Lithofacies and Reservoir Styles in Alberta: 13th CSPG Core Conference and Display, 1987. Canadian Society of Petroleum Geologists, pp. 73–85.

Teixell, A., Labaume, P., Ayarza, P., Espurt, N., de Saint Blanquat, M., Lagabrielle, Y., 2018. Crustal structure and evolution of the Pyrenean-Cantabrian belt: a review and new interpretations from recent concepts and data. Tectonophysics 724–725, 146–170. https://doi.org/10.1016/j.tecto.2018.01.009.

Teixell, A., Labaume, P., Lagabrielle, Y., 2016. The crustal evolution of the west-central Pyrenees revisited: inferences from a new kinematic scenario. Compt. Rendus Geosci. 348, 257–267. https://doi.org/10.1016/j.crte.2015.10.010.

Tortola, M., Al-Aasm, I.S., Crowe, R., 2020. Diagenetic pore fluid evolution and dolomitization of the Silurian and Devonian carbonates, Huron Domain of southwestern Ontario: petrographic, geochemical and fluid inclusion evidence. Minerals 10. https://doi.org/10.3390/min10020140.

Tostevin, R., Shields, G.A., Tarbuck, G.M., He, T., Clarkson, M.O., Wood, R.A., 2016. Effective use of cerium anomalies as a redox proxy in carbonate-dominated marine settings. Chem. Geol. 438, 146–162. https://doi.org/10.1016/j.chemgeo.2016.06.027.

Tugend, J., Manatschal, G., Kusznir, N.J., 2015. Spatial and temporal evolution of hyperextended rift systems: implication for the nature, kinematics, and timing of the Iberian- European plate boundary. Geology 43, 15–18. https://doi.org/10.1130/G36072.1.

Tugend, J., Manatschal, G., Kusznir, N.J., Masini, E., Mohn, G., Thinon, I., 2014. Formation and deformation of hyperextended rift systems: insights from rift domain mapping in the Bay of Biscay-Pyrenees. Tectonics 33, 1239–1276. https://doi.org/10.1002/2014TC003529.Received.

Vacherat, A., Mouthereau, F., Pik, R., Bellahsen, N., Gautheron, C., Bernet, M., Daudet, M., Balansa, J., Tibari, B., Pinna Jamme, R., Radal, J., 2016. Rift-to-collision transition recorded by tectonothermal evolution of the northern Pyrenees. Tectonics 35, 907–933. https://doi.org/10.1002/2015TC004016.

Vacherat, A., Mouthereau, F., Pik, R., Bernet, M., Gautheron, C., Masini, E., Le Pourhiet, L., Tibari, B., Lahfid, A., 2014. Thermal imprint of rift-related processes in orogens as recorded in the Pyrenees. Earth Planet Sci. Lett. 408, 296–306. https://doi.org/10.1016/j.epsl.2014.10.014.

Veizer, J., Ala, D., Azmy, K., Bruckschen, P., Buhl, D., Bruhn, F., Carden, G.A.F., Diener, A., Ebneth, S., Godderis, Y., Jasper, T., Korte, C., Pawellek, F., Podlaha, O.G., Strauss, H., 1999. $^{87}Sr/^{86}Sr$, $\delta^{13}C$ and $\delta^{18}O$ evolution of Phanerozoic seawater. Chem. Geol. 161, 59–88. https://doi.org/10.1016/S0009-2541(99)00081-9.

Veizer, J., Prokoph, A., 2015. Temperatures and oxygen isotopic composition of Phanerozoic oceans. Earth Sci. Rev. 146, 92–104. https://doi.org/10.1016/j.earscirev.2015.03.008.

Vergés, J., Millán, H., Roca, E., Muñoz, J.A., Marzo, M., Cirés, J., Bezemer, T. Den, Zoetemeijer, R., Cloetingh, S., 1995. Eastern Pyrenees and related foreland basins: pre-, syn- and post-collisional crustal-scale cross-sections. Mar. Petrol. Geol. 12, 903–915. https://doi.org/10.1016/0264-8172(95)98854-X.

Vermeesch, P., 2020. Unifying the U–Pb and Th–Pb methods: joint isochron regression and common Pb correction. Geochronology 2, 119–131. https://doi.org/10.5194/gchron-2-119-2020.

Vermeesch, P., 2018. IsoplotR: a free and open toolbox for geochronology. Geosci. Front. 9, 1479–1493. https://doi.org/10.1016/j.gsf.2018.04.001.

Vilasi, N., Malandain, J., Barrier, L., Callot, J.-P., Amrouch, K., Guilhaumou, N., Lacombe, O., Muska, K., Roure, F., Swennen, R., 2009. From outcrop and petrographic studies to basin-scale fluid flow modelling: the use of the Albanian natural laboratory for carbonate reservoir characterisation. Tectonophysics 474, 367–392. https://doi.org/10.1016/j.tecto.2009.01.033.

Warren, J., 2000. Dolomite: occurrence, evolution and economically important associations. Earth Sci. Rev. 52, 1–81. https://doi.org/10.1016/S0012-8252(00)00022-2.

Wendte, J., Chi, G., Al-Aasm, I.S., Sargent, D., 2009. Fault/fracture controlled hydrothermal dolomitization and associated diagenesis of the upper devonian jean marie member (Redknife formation) in the july lake area of northeastern British columbia. Bull. Can. Petrol. Geol. 57, 275–322. https://doi.org/10.2113/gscpgbull.57.3.275.

Wendte, J., Dravis, J.J., Stasiuk, L.D., Qing, H., Moore, S.L.O., Ward, G., 1998. High-temperature saline (thermoflux) dolomitization of Devonian Swan Hills platform and bank carbonates, Wild River area, west-central Alberta. Bull. Can. Petrol. Geol. 46 (2), 210–265. https://doi.org/10.35767/GSCPGBULL.46.2.210.

White, T., Al-Aasm, I.S., 1997. Hydrothermal dolomitization of the mississippian upper debolt formation, sikanni gas field, northeastern British columbia, Canada. Bull. Can. Petrol. Geol. 45 (3), 297–316. https://doi.org/10.35767/gscpgbull.45.3.297.

Wierzbicki, R., Dravis, J.J., Al-Aasm, I.S., Harland, N., 2006. Burial dolomitization and dissolution of upper jurassic Abenaki platform carbonates, deep panuke reservoir, Nova scotia, Canada. Am. Assoc. Petrol. Geol. Bull. 90, 1843–1861. https://doi.org/10.1306/03200605074.

Wilkinson, M., Crowley, S.F., Marshall, J.D., 1992. Model for the evolution of oxygen isotope ratios in the pore fluids of mudrocks during burial. Mar. Petrol. Geol. 9 (1), 98–105. https://doi.org/10.1016/0264-8172(92)90007-2.

Wright, P.V., 1992. A revised classification of limestones. Sediment. Geol. 76, 177–185. https://doi.org/10.1016/0037-0738(92)90082-3.

Ye, N., Zhang, S., Qing, H., Li, Y., Huang, Q., Liu, D., 2019. Dolomitization and its impact on porosity development and preservation in the deeply burial Lower Ordovician carbonate rocks of Tarim Basin, NW China. J. Petrol. Sci. Eng. 182 https://doi.org/10.1016/j.petrol.2019.106303.

Zenger, D.H., Dunham, J.B., 1980. Concept and models of dolomitization. Spec. Publ. Soc. Eng. Petrol. Mineral. 28, 1–9.

Zhang, J., Hu, W., Qian, Y., Wang, X., Cao, J., Zhu, J., Li, Q., Xie, X., 2009. Formation of saddle dolomites in Upper Cambrian carbonates, western Tarim Basin (northwest China): implications for fault-related fluid flow. Mar. Petrol. Geol. 26, 1428–1440. https://doi.org/10.1016/j.marpetgeo.2009.04.004.

Ziegler, P.A., Cloetingh, S., 2004. Dynamic processes controlling evolution of rifted basins. Earth Sci. Rev. 64, 1–50. https://doi.org/10.1016/S0012-8252(03)00041-2.